

# **OPTICALLY TRANSPARENT ANTENNAS FOR MULTI-MODAL SENSING**

A Thesis  
Presented to  
The Academic Faculty

By

Zachary J. Silva

In Partial Fulfillment  
of the Requirements for the Degree  
Master of Science in the  
School of Electrical and Computer Engineering

Georgia Institute of Technology

May 2019

Copyright © Zachary J. Silva 2019

# OPTICALLY TRANSPARENT ANTENNAS FOR MULTI-MODAL SENSING

Approved by:

Dr. Christopher R. Valenta, Advisor  
Electro-Optical Systems Laboratory  
*Georgia Tech Research Institute*  
School of Electrical and Computer  
Engineering  
*Georgia Institute of Technology*

Dr. Gregory D. Durgin, Co-advisor  
School of Electrical and Computer  
Engineering  
*Georgia Institute of Technology*

Dr. Thomas K. Gaylord  
School of Electrical and Computer  
Engineering  
*Georgia Institute of Technology*

Dr. Andrew F. Peterson  
School of Electrical and Computer  
Engineering  
*Georgia Institute of Technology*

Date Approved: April 23, 2019

*To my parents, for always believing in me.*

## **ACKNOWLEDGEMENTS**

I would like to Dr. Christopher Valenta, who I was introduced by from my undergraduate research advisor, Dr. Edward Wheeler. The connection from Rose-Hulman was key in guiding me into a new field of electromagnetics research that I would not have been able to find, arguably, anywhere else in the world. In addition, the mentorship, guidance, and impeccable knowledge shared by Chris has inspired me to continue my research in pursuit of the PhD in Electrical and Computer Engineering to create a broad impact my research. Also, I would like to thank my co-advisor, Dr. Gregory Durgin, for his insights of the fundamentals of electromagnetics and assistance throughout my MS research. I would like to thank my reading committee for their feedback and time in reviewing this thesis. Lastly, I would like to thank my parents for their unending support throughout my education and future endeavors.

## **DISCLAIMER**

This work was supported by the Critical Skills Masters Program at Sandia National Laboratories. This paper describes objective technical results and analysis. Any subjective views or opinions that might be expressed in the paper do not necessarily represent the views of the U.S. Department of Energy or the United States Government.

## TABLE OF CONTENTS

<b>Acknowledgments</b> . . . . .	iv
<b>Disclaimer</b> . . . . .	v
<b>List of Tables</b> . . . . .	x
<b>List of Figures</b> . . . . .	xi
<b>List of Symbols and Abbreviations</b> . . . . .	xvii
<b>Summary</b> . . . . .	xx
<b>Chapter 1: Introduction</b> . . . . .	1
1.1 History of Optically Transparent Conductors . . . . .	2
1.2 Optically Transparent Antennas . . . . .	4
1.3 Transparent Antennas for Novel Applications in Remote Sensing . . . . .	4
1.4 Research Overview . . . . .	5
<b>Chapter 2: Survey of Optically Transparent Conductors and Antennas</b> . . . . .	7
2.1 Optically Transparent Conductors . . . . .	7
2.2 Types of Optically Transparent Conductors . . . . .	9
2.2.1 Transparent Conducting Oxides . . . . .	9

2.2.2	Mesh Conductor . . . . .	10
2.2.3	More Optically Transparent Conductors . . . . .	12
2.2.4	Comparison of the State-of-the-art . . . . .	13
2.3	Optically Transparent Antennas . . . . .	14
2.3.1	The Early Periods . . . . .	15
2.3.2	Transparent Conductors for Antennas . . . . .	16
2.3.3	Antenna Topologies . . . . .	18
2.3.4	Antenna Applications . . . . .	20
<b>Chapter 3: Properties of Optically Transparent Conductors . . . . .</b>		<b>25</b>
3.1	Classical Electromagnetic Theory . . . . .	27
3.1.1	Maxwell's Curl Equations and the Constitutive Parameters . . . . .	28
3.1.2	Dielectric Response and Polarizability for TCOs . . . . .	33
3.1.3	Optics Relation to Constitutive Parameters . . . . .	38
3.1.4	Transmittance, Reflectance, and Absorbance . . . . .	41
3.2	Comparing Transparent Conductors Based on Electromagnetic Properties . . . . .	48
3.3	Comparison of Transparent Conductors . . . . .	50
3.3.1	Limitations of Transparent Conducting Oxides . . . . .	51
3.3.2	Advantages of Optically Transparent Mesh Conductor . . . . .	53
3.4	Proposed Figure of Merit for RF/EO Transparent Conductors . . . . .	55
3.4.1	Figure of Merit Specific to Transparent Conducting Oxides . . . . .	56
3.4.2	Figure of Merit Specific to Mesh Conductors . . . . .	60
3.4.3	Literature Data Comparison Based on New Figure of Merit . . . . .	61

<b>Chapter 4: Optical Characterization of Transparent Conductors . . . . .</b>	<b>66</b>
4.1 Measured Transmittance Comparison of Transparent Conductors . . . . .	67
4.2 Imaging through Transparent Conductors . . . . .	73
4.2.1 Imaging Background . . . . .	73
4.2.2 Imaging Set-up . . . . .	76
4.2.3 Imaging Measurements and Analysis . . . . .	80
 <b>Chapter 5: Characterization of mesh conductor for Microstrip Transmission             Lines and Antennas . . . . .</b>	 <b>84</b>
5.1 Microstrip Transmission Line . . . . .	85
5.2 S-parameters to RLGC . . . . .	86
5.3 Meshed Transmission Line with Solid Ground Plane . . . . .	88
5.3.1 Proposed Modification to Effective Permittivity . . . . .	88
5.3.2 Simulation vs Measurement . . . . .	89
5.3.3 Meshed vs Solid Comparison . . . . .	91
5.4 Mesh Transmission Line and Mesh Ground Plane . . . . .	93
5.4.1 Compensating for the Propagation Effects Introduced by the Mesh Conductor . . . . .	96
5.5 Meshed Patch Antennas . . . . .	100
5.5.1 Antenna Design . . . . .	100
5.5.2 Results . . . . .	101
5.6 Meshed, Linear, Series Fed Patch Array . . . . .	106
 <b>Chapter 6: Conclusion and Future Work . . . . .</b>	 <b>110</b>
6.1 Future Work . . . . .	111



6.1.1	Exploring Infrared Transparent Antennas . . . . .	111
6.1.2	Signal launch and feeding mechanisms . . . . .	111
6.1.3	Purposely Misaligning the Top and Bottom Layer of Mesh Patch Antenna . . . . .	112
6.1.4	Optically Transparent Array Layout . . . . .	112
6.1.5	Array Front-to-Back Ratio Measurement . . . . .	112
6.1.6	Array Fabrication and Test . . . . .	113
6.1.7	Multi-modal Sensing System Construction . . . . .	113
6.1.8	RF-EO/IR Single Aperture Sensor Fusion . . . . .	113
6.2	Contributions . . . . .	114
6.3	Publications and Presentations . . . . .	115
6.3.1	Peer Reviewed Journal Articles . . . . .	115
6.3.2	Refereed Conference Proceedings and Presentations . . . . .	116
6.3.3	Poster Presentations . . . . .	116
<b>References . . . . .</b>		<b>117</b>

## LIST OF TABLES

2.1	Published data for each class of optically transparent conductors (transparent in the visible light region). [12] . . . . .	24
3.1	Typical metals with comparison to transparent conducting oxides showing the direct relationship between D.C. conductivity and plasma frequency. . .	38
3.2	Material behavior based on the effects on parameters and constants above and below the plasma frequency where the material acts as a good insulator and good conductor, respectively. . . . .	51
3.3	Published data from Table 2.1 that provided thickness, transmittance, and sheet resistance to be used for analysis on the new figure of merit for transparent RF conductors . . . . .	62
3.4	Summarized list of the important equations from the chapter . . . . .	65
4.1	Summary of set-up and Nikon DLSR camera settings for <i>MTF</i> imaging experiment. . . . .	78
5.1	Solid transmission line and meshed transmission line design parameters. . .	91
5.2	Simulated transmission line with solid ground plane parameters versus fill factor. . . . .	92
5.3	Solid transmission line and meshed transmission line design parameters. . .	94
5.4	Simulated meshed transmission line parameters with meshed ground plane versus fill factor. . . . .	96
5.5	Antenna parameters versus fill factor. . . . .	104

## LIST OF FIGURES

2.1	Mesh with defined parameters used for fill factor. . . . .	11
2.2	Reported optically transparent conductors with lines of constant figure of merit $\phi_{TC}$ at 0.01, 0.1, 1, and 10. Note: not all conductors are the same thickness, material, etc. [12] . . . . .	14
2.3	Comparison of antenna gains for the mesh, ITO, and AgHT transparent conductors. (Note: variety of antenna topologies are used including one-layer and two-layer metallizations.) [12] . . . . .	17
2.4	. . . . .	20
2.5	(Left) Transparent antenna for integration on CubeSat solar panels. (Middle) Dimensioned model of 2.5 GHz probe-fed patch antenna. (Right) Simulated and measured antenna gain plots at 2.5 GHz [86]. . . . .	21
2.6	(Left) Transparent 717 MHz/2.11 GHz mesh antenna on a vehicle front windshield. (Right) 3D visualization of observed antenna gain at 2.11 GHz [10]. . . . .	22
2.7	Transparent antenna for smart glasses made out of a multilayer film of IZTO/Ag/IZTO at 2.4 GHz [104]. . . . .	23
3.1	RF and Optical Operational Modes (Top) Optical/Infrared operation at $\lambda_{EO/IR}$ which hold values of transmittance $T$ with absorption $\alpha_\kappa$ where desired operation is an optically transparent conductor where an incident electromagnetic wave passes without reflection or absorption (Bottom) RF/microwave operation at $f_{RF}$ with conductivity $\sigma$ where the desired operation is a guided wave operation as shown with transverse propagation and resonant antenna radiation. . . . .	27

3.2	Relationship between attenuation constant $\alpha$ and phase constant $\beta$ for propagation perpendicularly through a metal versus effective conductivity assuming for simplicity, $\epsilon' = \epsilon_0$ and $\tilde{\mu} = \mu_0$ . For illustration of the behavior of the effective conductivity, $\sigma$ , $\tilde{\mu}$ , $\epsilon'$ , and $\epsilon''$ assumed to remain constant over all frequencies. . . . .	31
3.3	Dispersion of materials with frequency over the entire electromagnetic spectrum which shows a changing real and imaginary part of electric permittivity over the entire EM spectrum [105]. Adapted from [111]. . . . .	35
3.4	Transparent conducting oxide interface displaying incident, reflected, absorbed, and transmitted wave interactions . . . . .	42
3.5	Exponentially decreasing electromagnetic wave in an optically dense material. For TCO's the decrease is strong at RF/mm-Wave frequencies, and much less in visible wavelengths. . . . .	44
3.6	Transmittance, reflectance, and absorbance for an ITO film with plasma frequency $\omega_p = 1500$ nm [8] . . . . .	46
3.7	Log-log comparison of skin depth ( $\mu\text{m}$ ) versus conductivity for various RF frequencies compared to Indium Tin Oxide (ITO) and mesh conductors. . .	50
3.8	Optical penetration depth and conductivity versus plasma frequency given an operating wavelength in the visible region of 550 nm and DC conductivity versus plasma frequency. The graph is fixing the operating frequency and varying the plasma frequency to display the effects of operating above and below the plasma frequency. . . . .	52
3.9	Mesh topology described by an RLC high pass filter [117]. . . . .	53
3.10	Optical transmittance and conductivity versus fill factor. . . . .	55
3.11	Figure of merit for a TCO versus plasma wavelength for optical operating wavelength of 550 nm (visible) for different ISM Band frequencies with a material thickness of 100 nm to achieve transmittance and the RF surface resistance when skin depth is not met. . . . .	59
3.12	Figure of merit for a TCO versus changing thickness at operating wavelength $\lambda = 550\text{nm}$ and Drude model plasma wavelengths of $\lambda = 1000\text{nm}$ and $\lambda = 1500\text{nm}$ with literature data plotted for comparison. . . . .	59
3.13	Modified new figure of merit for a $1\ \mu\text{m}$ thick copper mesh conductor ( $\sigma = 5.8e7\ \text{S/m}$ ) versus fill factor for the ISM band frequencies using the figure of merit in (3.72). . . . .	61

3.14	Modified figure of merit for transparent conductors using skin depth calculated at frequency $f_{RF}=2.45$ GHz. (Left) Figure of merit versus reported visible transmittance (Right) Figure Figure of merit versus reported conductivity. . . . .	63
3.15	Modified figure of merit for transparent conductors using skin depth calculated at frequency $f_{RF}=5.8$ GHz. (Left) Figure of merit versus reported visible transmittance (Right) Figure Figure of merit versus reported conductivity. . . . .	63
3.16	Modified figure of merit for transparent conductors using skin depth calculated at frequency $f_{RF}=24$ GHz. (Left) Figure of merit versus reported visible transmittance (Right) Figure Figure of merit versus reported conductivity. . . . .	64
3.17	Modified figure of merit for transparent conductors using skin depth calculated at frequency $f_{RF}=77$ GHz. (Left) Figure of merit versus reported visible transmittance (Right) Figure Figure of merit versus reported conductivity. . . . .	64
4.1	Transparent mesh antenna (left) K-layout model and (right) fabricated photos from Binghamton University CAMM. Mesh parameters are $1\text{ }\mu\text{m}$ thick copper mesh, pitch $g' = 95\text{ }\mu\text{m}$ , and line width $w' = 5\text{ }\mu\text{m}$ for a calculated fill factor $\Psi = 0.05$ . . . . .	67
4.2	Sample optical transmittance measurement set-up in the Cary 5000 Spectrometer annotated for optical characterization from 200 nm to 3200 nm. . .	68
4.3	Normal transmittance of ITO, mesh and the baselines (PET, Willow glass) .	69
4.4	Normalized transmittance comparison of ITO and mesh conductors. . . . .	69
4.5	Mesh parameters with added angle of incidence . . . . .	70
4.6	two-layer mesh with substrate separating and illustration of the effective fill factor due to the second layer mesh. The simple geometric approximation to the fill factor versus angle of incidence allows the transmittance to be predicted. . . . .	71
4.7	Simulation of transmittance versus angle for a two-layer mesh with substrate separating and illustration of the effective fill factor due to the second layer mesh. Mesh parameters same as fabricated values as $w' = 5\text{ }\mu\text{m}$ , $g' = 95\text{ }\mu\text{m}$ , $t = 1\text{ }\mu\text{m}$ , and $t_{sub} = 100\text{ }\mu\text{m}$ . . . . .	72

4.8	Transmittance vs wavelength of ITO (right), mesh (left) with baseline PET and Willow glass divided out and captured incident angles of 0, 10, 20, 40 degrees. . . . .	72
4.9	USAF 1951 Resolution Target . . . . .	75
4.10	ISO12233:2000 Slant Edge Resolution Target with slant targets and resolution line pairs shown. . . . .	76
4.11	ISO12233 spatial frequency response extraction method [120] . . . . .	77
4.12	Modified set-up of the slant-edge method as described in the slant-edge repeatability study with mesh and ITO samples in front of the lens [119]. . .	78
4.13	Diagram showing how the slant edge is projected, binned, and averaged to create a one-dimensional profile from the two-dimensional dataset [121]. . .	79
4.14	Baseline image of slant target with area of interest in red. . . . .	81
4.15	Image of slant target with mesh conductor over aperture with area of interest in red . . . . .	81
4.16	Image of slant target with ITO conductor over aperture with area of interest in red . . . . .	81
4.17	Sample of slant-edge data for a raw (uncovered) aperture, a metal mesh covered aperture, and an ITO covered aperture. . . . .	82
4.18	Processed <i>MTF</i> of the slant-edge data for a raw (uncovered) aperture, a metal mesh covered aperture, and an ITO covered aperture using sfrmat3.m. . . . .	82
4.19	Extracted <i>MTF</i> displaying individual spatial frequency response of mesh and ITO. . . . .	83
5.1	Lumped element RLGC circuit model for transmission lines . . . . .	85
5.2	(a) Unit cell with cross section of dielectric and air interface. AA' is the portion with solid transmission line. BB' is the portion with an open gap in the transmission line. (b) Cross section showing the effective permittivity covering the full region of the transmission line. . . . .	89
5.3	Fabricated board with the solid transmission line (Trace 1) and the meshed transmission line (Trace 2). . . . .	90

5.4	Parameterized mesh transmission line board parameters . . . . .	90
5.5	Simulated and measured transmission line $ S_{11} $ reference left axis and $ S_{21} $ reference right y-axis. Measured data for the solid and mesh transmission lines shown in Fig. 5.3. . . . .	91
5.6	Simulated electric field at 2.4 GHz of (a) solid transmission line (b) mesh transmission line with a solid ground plane . . . . .	92
5.7	Top and bottom example of microstrip transmission line with meshed trace and ground plane. . . . .	93
5.8	Inductance versus fill factor with simulated values extracted from s-parameters and a theoretical model based on (5.17) . . . . .	96
5.9	Capacitance versus fill factor with simulated values extracted from s-parameters and a theoretical model based on (5.16) . . . . .	97
5.10	Impedance versus fill factor extracted from the s-parameters. . . . .	97
5.11	Power loss at different fill factors over the simulated frequency range. Note loss increase as the frequency increases; this includes dielectric and conductor loss in the simulations. As fill factor decreases, the loss increases as expected. . . . .	98
5.12	Interpolated power loss versus fill factor versus the simulated frequency range. Note loss increase as the frequency increases, this includes dielectric and conductor loss in the simulations. As fill factor decreases, the loss increases as expected. . . . .	98
5.13	Simulated S-parameters to match the meshed transmission line using a lower impedance solid transmission line as the reference. $W = 4.2mm$ $\Psi = 0.16$ for $S_{11}$ -mesh and $S_{21}$ -mesh (simulated without connectors). . .	99
5.14	(Left) Solid patch antenna with solid ground plane (Right) Mesh patch antenna with same dimensions of $W, l, a, C, D$ and meshed ground plane (Ground planes not shown). . . . .	100
5.15	Simulated and measured return loss of the antennas from Fig. 5.14 and 5.16. . . . .	102
5.16	Adjusted patch antenna decreasing the length $l$ by 1.1 mm to be 27.72 mm. $\Psi, W, a, C, D$ all remain constant. (Left) CST model (Right) Fabricated with SMA connector. . . . .	102

5.17	Measured antenna patterns at 2.52 GHz for both the solid and adjusted mesh patch antennas with realized gain shown. (Left) Elevation Pattern (Right) Azimuth Pattern. . . . .	103
5.18	Simulated front to back ratio versus fill factor for 2.52 GHz mesh patch antenna. . . . .	104
5.19	Simulated 3dB beamwidth $\theta_3$ versus fill factor for 2.52 GHz mesh patch antenna. . . . .	105
5.20	Simulated realized gain (dB) versus fill factor for 2.52 GHz mesh patch antenna. . . . .	105
5.21	5.8 GHz meshed linear, series fed patch array. . . . .	108
5.22	S-parameters for 5.8 GHz meshed linear, series fed patch array. . . . .	108
5.23	Simulated Pattern for 5.8 GHz meshed linear, series fed patch array. . . . .	109
6.1	Single aperture multi-modal sensing or communications. . . . .	110



## LIST OF SYMBOLS AND ABBREVIATIONS

$\alpha$	attenuation constant
$\alpha_{\kappa}$	optical attenuation constant (absorption coefficient)
$\delta_s$	skin depth
$\delta_{s(\kappa)}$	optical skin depth (penetration depth)
$\epsilon_0$	free space permittivity ( $8.854 \times 10^{-12} \frac{F}{m}$ )
$\gamma$	propagation constant
$\kappa$	extinction coefficient
$\lambda$	wavelength
$\mu_0$	free space permeability ( $4\pi \times 10^{-7} \frac{H}{m}$ )
$\omega_p$	plasma frequency
$\phi_{TC}$	figure of merit for transparent conductors
$\Psi$	fill factor
$\sigma$	DC conductivity
$\sigma_e$	effective conductivity
$\tau$	electron relaxation time
$\tilde{\epsilon}$	complex permittivity

$\tilde{\epsilon}_D$	complex permittivity using the Drude-free-electron model
$\tilde{\mu}$	complex permeability
$\tilde{n}$	complex refractive index
$\tilde{n}_D$	complex refractive index using the Drude-free-electron model
$A$	absorbance
$C_{pul}$	capacitance per unit length
$FBR$	front-to-back ratio of antenna gain pattern
$G_{pul}$	conductance per unit length
$L_{pul}$	inductance per unit length
$n$	refractive index
$R$	reflectance
$R_s$	DC sheet resistance
$R_s^{RF}$	RF surface resistance
$R_{pul}$	resistance per unit length
$T$	transmittance
<b>EM</b>	electromagnetics
<b>EO</b>	electro-optical
<b>ESF</b>	edge spread function
<b>FOM</b>	figure of merit
<b>IR</b>	infrared

**ITO** Indium Tin Oxide

**LSF** line spread function

**MTF** modulation transfer function

**PSF** point spread function

**RF** radio-frequency

**SWaP** size, weight, and power

**TCF** transparent conducting film

**TCO** transparent conducting oxide

**UV** ultraviolet

## SUMMARY

The advent of multi-modal data fusion, the rise of CubeSats, and the dawn of the drone have all, among others, put pressure on sensor developers to increase payload performance while decreasing their size, weight, and power (SWaP). High performance optically transparent conductors realized as antennas can be used for single aperture RF-EO/IR fusion for autonomous vehicle navigation, as communication and sensing antennas on CubeSat missions, and also for embedded antennas in camera lenses for visible and thermal imaging.

The trade-off between optical transparency and conductivity is evident and well documented within the materials science community. However, the fundamental criteria to achieve optical transparency of a conductor at RF, microwave, and millimeter wave frequencies has not been well established. Typically, transparent conducting oxides have been used to achieve optical transparency, but a metal mesh has also been shown to work effectively.

The novel contribution of this thesis is a discussion and analysis of transparent conductors and antennas for the application of single aperture multi-modal remote sensing. The thesis presents the electromagnetic properties of optically transparent conductors starting with Maxwell's equations to discuss the material properties of transparent conductors from direct current (DC) through ultra-violet (UV) frequencies. Using the results of the material properties, a new and improved figure of merit for optically transparent RF conductors will be presented, allowing comparison of optically transparent conductors at microwave frequencies. The comparison leads to the conclusion that the mesh conductor will outperform natural occurring transparent conducting oxides in all ISM frequency bands. In addition, details on the conductor requirements for RF circuitry, and a characterization of the optical transmission and imaging effects are presented. Finally, the thesis will present the RF design and characterization of meshed transmission lines and meshed patch antennas.

# CHAPTER 1

## INTRODUCTION

---

**Chapter Overview:** This chapter provides the following:

- Brief introduction and historical context of optically transparent conductors and antennas
  - An introductory discussion of the broader impacts of the proposed research for RF-EO/IR multi-modal sensing
  - An overview of the organization of the thesis
- 

This thesis will explore optically transparent conductors for multi-modal sensing, specifically single aperture RF-EO/IR multi-modal sensing. Currently, optically transparent antennas are primarily used as unobtrusive antennas for automotive applications and for antennas embedded onto solar cells for CubeSat and SmallSat communications. This work, however, will be investigating optically transparent antennas for RF-EO/IR single aperture sensing in which the RF and EO/IR data will be fused exploiting the difference in material properties at different regions of the electromagnetic spectrum while reducing size, weight, and power as a bonus. Current sensor fusion in automotive and satellite applications uses distributed sensors which requires highly complex data alignment which includes an inherent angular variation in the return data. Single aperture, co-located sensors will allow for a system in which the separate RF and EO/IR signals will have similar field of view, phase center, and return paths which is not possible with the distributed sensors. This thesis lays the groundwork and RF-EO/IR co-design on optically transparent conductors for the future implementation onto a single aperture RF-EO/IR remote sensing system.

## 1.1 History of Optically Transparent Conductors

Before discussing optically transparent antennas, an introduction of optically transparent conductors is necessary. Optically transparent conductors have a surprisingly long history starting with the first transparent metallic film published in 1877 by Yale Professor Arthur Wright [1]. The first transparent metallic film experiments were carried out by depositing metals from cathode discharge in exhausted tubes to create a simultaneous visibly transparent and conductive electrode. The specific application for the Wright's work was not specified in the initial publication but was noted to be part of university research. Thirty years later, the first published transparent conducting oxide (TCO) was developed in 1907 when German physicist, Karl Baedeker, at the University of Jena introduced cadmium oxide, CdO [2]. Baedeker's work was different than Wright's since it was created as a compound oxide doped with a metal, rather than a pure metallic film. The original publication on CdO described the material to have a yellowish hue from the deposition process of the CdO, but it was still visibly transparent. The studies by Baedeker and Wright opened a new area of engineering that many thought impossible. The optically transparent conductors started further studies and drove innovation to create higher performing optically transparent conductors.

The work from Wright and Baedeker laid the foundation for the largest breakthroughs in optically transparent conductors which occurred after WWII, when transparent electrodes were being investigated for optoelectronic devices (heated windows, selenium rectifier photocells, antistatic windows, etc) [3]. Around this time in the 1950's, tin oxide materials as a material to defrost windshields on an airplane cockpit were patented by Harold McMaster of Libbey-Owens-Ford Glass Company [4]. During the 1970s oil crisis, energy conservation awareness was growing to all-time highs. Government and businesses wanted to control the amount of heat passing through a window to save on heating and cooling costs. There is a known relationship between the conductivity of a mate-

rial and its emissivity. As a result, multi-layer films like Bismuth Oxide/Gold/Bismuth Oxide ( $\text{Bi}_2\text{O}_3/\text{Au}/\text{Bi}_2\text{O}_3$ ), Silicon Monoxide/Gold/Silicon Monoxide ( $\text{SiO}/\text{Au}/\text{SiO}$ ), Titania/Silver/Titania ( $\text{TiO}_2/\text{Ag}/\text{TiO}_2$ ), Zinc Sulfide/Aluminum/Zinc Sulfide ( $\text{ZnS}/\text{Al}/\text{ZnS}$ ), and more similar compounds used in the present day glass windows are used as low emissivity coatings that aim to minimize the amount of long wave ultraviolet A (UVA), short wave ultraviolet B (UVB), and infrared light that can pass through glass without compromising the amount of transmitted visible light [5]. Multi-layer films are still extensively studied as an alternative transparent conductor, using a known metal to boost conductivity to reduce the emissivity while maintaining optical transparency [6],[7].

Since the mid-1900s, transparent conducting oxides dominated the space of optically transparent conductors, specifically indium tin oxide (ITO). As ITO has been so widely used and studied, the manufacturing process has been optimized and has become easy to deposit as a thin film with sheet resistance  $< 10 \Omega/\text{sq}$  and with relatively high visible transparency  $> 80\%$ . The challenges and concerns with ITO is that indium is toxic and can be very harmful if inhaled when depositing in the clean-room. As a result, non-toxic materials have been investigated as an alternative to ITO. An example of an alternative TCO is Aluminum Zinc Oxide (AZO or  $\text{ZnO}:\text{Al}$ ), which uses Zinc Oxide as the base compound doped with aluminum to provide the conductivity [8].

Most recently, advancements in micro-fabrication capabilities as well as in material science have allowed periodic metal grids and non-uniform nanowire networks to be created and implemented as a transparent conductor. The metal grids and nanowire networks use the open space as a means of transparency while providing high levels of conductivity in the wires. Nanowires, at one point, looked to be the unanimous decision to replace ITO due to the continuously exhibited high performance at a low cost [9], but currently the uniform metal mesh has ability for higher optical and electrical performance with a simpler deposition process. As research progresses, materials will continue to evolve based on the application and systems requirements making the decision for *best* transparent conductor

difficult.

As research on optically transparent conductors progresses, it continues to show improvements in optical and electrical performance for new upcoming technologies in consumer electronics. Studies over the past 100 years on optically transparent conductors have discovered the difficulty in creating materials that exhibit high optical transparency and electrical conductivity simultaneously [8].

## **1.2 Optically Transparent Antennas**

With transparent conductors well established, the idea of optically transparent antennas began in 1989 with the first patent suggesting a transparent vehicle antenna to be embedded on the windshield to receive FM and TV broadcast signals. Until this point, vehicle antennas had been large, obtrusive monopole antennas inserted on the hood of the vehicle. Importantly, the initial patent pointed out the radiation efficiency challenges due to the decreased conductivity of transparent conductors.

Unlike transparent antennas, transparent conductors have been widely researched in many fields of physics, materials science, and nanotechnology for over 100 years. The transparent conductors previously discussed are not applicable to RF applications since the thin films do not reach the requirements of skin depth to avoid resistive losses in the circuit, and will be discussed further in Chapter 3. Due to the conductive limitations of previously used transparent conducting films, the metal mesh is used for RF applications which achieves transparency by etching or cutting away the metal to form a periodic grid [10].

## **1.3 Transparent Antennas for Novel Applications in Remote Sensing**

As the presented work is introductory in nature, there are broader impacts worth discussion for applications the technology could be applied to, from automotive, UAV, commercial air, and satellite sensing. A major challenge in classical multi-system sensor fusion



is that complex data alignment that must be performed which requires high computation. This alignment is a result of the dual apertures requires dual computing systems to process separate problems based on the spatial locations of the sensors which in turn does not optimize the SWaP [11]. Single aperture sensing, however, allows the RF sensing to be co-located with the optical/infrared sensing mechanism which reduces the computation to a single system into a low SWaP system. SWaP, however, isn't the only benefit to this technology, using a single aperture combined with two sensors, (i.e. synthetic aperture radar combined with synthetic aperture lidar, laser doppler vibrometer or thermal imaging) will allow new data visualization for enhanced spatial awareness. Remote sensing communities could utilize the single aperture RF-EO/IR sensing for new classification methods like the normalized difference vegetative index (NDVI). NDVI exploits the difference in vegetation's return near infrared (NIR) and visible red return to classify vegetation since the material absorbs or reflects the separate wavelengths differently based on the health of the vegetation. Exploiting the behavior of materials, similar to the NDVI technique, will allow the environment and materials to be easily classified in ways that has not yet been possible with dual system sensor fusion.

#### **1.4 Research Overview**

The research presented is novel in the presentation of the direct comparison of transparent conducting oxides (TCOs) and mesh conductors in terms of material parameters and geometry pointing out the fundamental limitations of TCOs at RF. The analysis leads to a co-optimization for RF-EO/IR performance with a new figure of merit for transparent RF conductors. Introductory analysis of the electromagnetic effects of a fully meshed microstrip circuit will be presented for both transmission lines and patch antennas.

Overall, this research seeks to answer the following question:

*In order to effectively achieve single aperture RF-EO/IR multi-modal sensing, what optically transparent conductor should be used, and how is the RF and optical performance affected when this conductor is introduced?*

The remainder of this thesis is organized as follows:

**Chapter 2** introduces the types of transparent conductors currently used with a literature survey displaying the performance. The chapter also presents the state-of-the-art in transparent antennas.

**Chapter 3** discusses the electromagnetics behind optically transparent conductors, discussing how a material can be both conductive and optically transparent. This chapter also gives comparisons of transparent conductors in terms of optical transmittance, imaging and presents a novel RF figure of merit for transparent conductors compared with literature data.

**Chapter 4** presents the optical characterization of optically transparent conductors for transmittance and imaging performance.

**Chapter 5** presents the characterization of mesh transmission lines and antennas explaining further into how a mesh affects propagation in a microstrip circuit as well as how the mesh affects the radiation properties such as realized gain and front-to-back ratio.

**Chapter 6** will conclude the thesis with a discussion of future work, including challenges for future implementations.

## CHAPTER 2

### SURVEY OF OPTICALLY TRANSPARENT CONDUCTORS AND ANTENNAS

---

**Chapter Overview:** This chapter provides the following:

- Fundamentals of optically transparent conductors
  - Survey of optically transparent conductors and antennas performance and applications
  - Discussion of the state-of-the-art in optically transparent antennas
- 

This chapter will present a survey of the work that has been published around optically transparent conductors, specifically for optically transparent antennas. Much of the content in this chapter is also in review for a magazine article in IEEE Antennas and Propagation Magazine [12].

#### 2.1 Optically Transparent Conductors

Optically transparent conductors take two major forms - transparent conducting films (TCFs) and conductive meshes. The former primarily consists of transparent conducting oxides (TCOs), but other types of materials and nanostructures have also been reported in the literature. The latter consists of a grid of conducting wires which is transmissive primarily due to a removal of conducting material within the outline of the structure, like a window screen. Additionally, it's critical to point out that optically transparent concerns the transmission of optical wavelengths from the ultraviolet to the visible to the short-, mid-, and long-wave infra-red (IR) through the material (but rarely occurring across more than one or

two of these bands due to the bandwidth limitations of many electro-optical applications). Likewise, conductors allow electrons to flow with minimal loss, slowly degrading with increasing frequency. An optically transparent conductor is one designed to transmit a particular part of the optical spectrum while simultaneously allowing the conduction of a part of the radio frequency, microwave region of the spectrum .

Optically, the materials are characterized by transmittance  $T$  through the material, which is measured as a function of wavelength, and index of refraction  $n$ . Electrically, in contrast, the materials are characterized using sheet resistance, typically measured at d.c. using a four point probe. The sheet resistance  $R_s$

$$R_s = \frac{1}{\sigma t}, \quad (2.1)$$

is limited by two factors, the conductivity  $\sigma$  and the film thickness  $t$ . A perfect transparent conductor would have 100% optical transmittance and infinite conductivity (zero sheet resistance). Naturally occurring materials typically compromise between these two quantities over the electromagnetic spectrum, making the relative comparisons between them difficult. To quantify an optically transparent conductor's performance, a figure of merit was introduced which relates a material's optical transmittance with its electrical conductivity [13]. The figure of merit  $\phi_{TC}$  is defined as

$$\phi_{TC} = \frac{T^{10}}{R_s}, \quad (2.2)$$

where  $T$  is transmittance, and  $R_s$  is d.c. sheet resistance as discussed before. The figure of merit, from Haacke, is  $T^{10}$  due to analysis of maximizing  $T/R_s$  when  $T = \exp(-\alpha t)$ , where  $\alpha$  is optical attenuation constant, and  $R_s = \frac{1}{\sigma t}$ . Taking the derivative with respect to  $t$  and setting equal to zero and plugging the maximum thickness back in, gives a  $t_{max} = 1/\alpha$ . Plugging the  $t_{max}$  back into the transmittance, give a max figure of merit when optical transmission  $T = 0.37$ , which is not desirable for an optical system. As a result, the  $T^{10}$

was included to weight the maximum figure of merit for a transmittance of 0.9, a much more efficient optical transmission value [13].

Using the figure of merit for transparent conductors, transparent conductor innovation has been driven further, paving a path for transparent microwave and millimeter wave (mmW) devices like antennas, interconnects, and filters. Optically transparent conductors at microwave/mmW frequencies enable new sensor fusion techniques and electromagnetic structures not previously possible. Without the innovation and history of transparent conductors, the recent transparent RF conductors would not be possible. Transparent conductors have been around for over 100 years, and the field of research is still thriving.

## 2.2 Types of Optically Transparent Conductors

As alluded to before, transparent conductors come in two major types, transparent conducting films (specifically TCOs) and meshed conductors. Both transparent conductors are used for a wide range of applications. For each application, the specifications change so there is no clear cut top transparent conductor for all applications. The following sections discuss the major differences of the top transparent conductors.

### 2.2.1 Transparent Conducting Oxides

Of the transparent conductors in literature, transparent conducting oxides (TCOs) are the most studied. TCOs are wide band gap semi-conductors resulting from an oxide compound doped with a metal. These compounds are usually deposited on a substrate (rigid or flexible, glass or plastic) that is transparent in the same spectrum as the TCO is designed to be transmissive at. The total transmittance  $T_{total}$  can be expressed as

$$T_{total} = T_{TCO}T_{substrate}, \quad (2.3)$$

where  $T_{TCO}$  is the transparent conducting oxide transmittance and  $T_{substrate}$  is the transmittance of the substrate that the TCO is deposited.

Indium Tin Oxide (ITO) is the most commonly used TCO due to its electrical conductivity between 6 and 12  $\Omega/sq$ , visible optical transparency between 75 and 92% (at 550 nm), and ease of manufacturing from a large industrial base. Since ITO has been studied in-depth by industry and academia, processes to deposit ITO as a thin film have matured and continue to improve. However, indium is very toxic when manufacturing and can be very dangerous if inhaled. In addition, supply, cost, and pollution is an issue since indium is a rare earth element.

Aluminum zinc oxide (AZO) is another transparent conducting oxide, similar to ITO as it is a doped oxide compound. As a non-toxic alternative to ITO, AZO thin films utilize inexpensive, readily available source materials but lack large area, high yield deposition techniques, and more importantly, a large industrial base. Moreover, AZO displays higher conductivity and transparency than ITO with sheet resistances published from 3.8 to 7.1  $\Omega/sq$  and transparencies ranging from 76-96.5% at 550 nm [8].

Lesser known materials such as fluorine tin oxide (FTO), antimony tin oxide (ATO), gallium zinc oxide (GZO), and other multilayer TCO films have also been reported in the literature with comparable performance to ITO and AZO. Currently the materials don't present any major benefits over these two dominant films [8].

### 2.2.2 Mesh Conductor

The mesh is the other class of optically transparent conductors. It is not a TCO since there is no oxide layer. Like a TCO, it is typically layered on top of a glass or plastic substrate. Physically, it is a patterned solid conductor that has metal removed in a periodic pattern to form a mesh. The mesh is fabricated by depositing a metal (Ag, Au, Cu, etc.) and etching the mesh on the substrate. The mesh transmittance is limited by the fill factor  $\Psi$  described in (2.4), which is defined by line width  $w'$ , pitch or gap  $g'$ , and conductor thickness  $t$  illustrated

in Fig. 2.1, [14]. Line widths and pitches are limited by the fabrication process used to create the mesh.

$$\Psi = \frac{w'}{g' + w'} \quad (2.4)$$

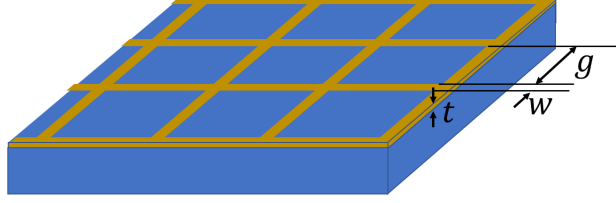


Figure 2.1: Mesh with defined parameters used for fill factor.

A 95% transparent conductor  $T_{tot}$  is possible, for example, with a fill factor of 0.025 using (2.5) and (2.6) assuming a lossless substrate. Here,  $T_{substrate}$  is the transmission of the substrate, and  $T_{mesh}$  is the transmission of the mesh. The total transmission  $T_{tot}$  is simply the product of the transmissions of each layer of the stackup. Note that (2.6) assumes the mesh itself is complete opaque (not transmissive). It can be modified if the conductor is partially transparent.

$$T_{tot} = T_{substrate} T_{mesh} \quad (2.5)$$

$$T_{mesh} = (1 - \Psi)^2 \quad (2.6)$$

The sheet resistance  $R_s$  for the mesh in (2.7) incorporates fill factor  $\Psi$  as the conductance per square is reduced along with the fill of the metal.

$$R_s = \frac{1}{\sigma t (2\Psi - \Psi^2)} \quad (2.7)$$

As a result of the larger conductivity of the metals typically used to create meshes (even reduced by the fill factor), the mesh has substantially lower sheet resistance than any of

the TCOs. Published mesh sheet resistances vary between 0.018-0.36  $\Omega/sq$ , making the mesh a more suitable candidate for use as a conductor in high frequency RF application. However, the total transmittance for the mesh structures is lower than the TCOs with values ranging between 54 and 90%, but higher mesh optical performance is possible by simply changing the geometry. Unlike TCOs, the transmittance of a mesh is more stable over a wide range of optical wavelengths since it is not dependent on the material properties of the mesh, only the geometry. Mesh transparency and sheet resistance can be directly controlled by varying the width and pitch of the individual lines as clearly illustrated by (2.6) and (2.7). The relationship shows as fill factor increases, both the sheet resistance and transmittance decrease. When  $\Psi$  is equal to one, the conductor is opaque, but has the lowest possible sheet resistance. Transparent conducting materials can have very similar optical properties, but the values of sheet resistance will vary greatly depending on the conductance of the material selected and the arrangement of the mesh. Published data shows that meshes have sheet resistance at least 22 times less than that of AZO and ITO with the same transmittance. This fact makes the mesh far more suitable for micro- and millimeter-wave applications.

### 2.2.3 More Optically Transparent Conductors

Academics and industry gravitate around a few transparent conductors due to availability and manufacturing limitations. Silver coated polyester (AgHT) film was considered as an alternative film which has sheet resistance of 4 or 8  $\Omega/sq$  (hence standard names AgHT-4 and AgHT-8, respectively). AgHT displays transmittance around 80% transparency and has been used on plastic substrates, showing an improvement in electrical performance from many of the ITO films [15]. Silver nanoparticles (AgNP) are less commonly used since the sheet resistance is higher than both ITO and AZO at 23  $\Omega/sq$  [16]. Furthermore, a similar option to the mesh, a silver nanoparticle grid (AgNP) resulted in a 95% transparency but a sheet resistance of 26.5  $\Omega/sq$  [17]. Moving from AgNP, graphene electrodes are also



documented as optically transparent conductors but have higher sheet resistance around  $125 \Omega/sq$  and used for applications that require much less electrical conductivity [18]. Each year more transparent conductors are released in literature and the list of exotic materials continues to grow.

#### 2.2.4 Comparison of the State-of-the-art

A survey of optically transparent conductors is presented in Table 2.1 and visualized in Fig. 2.2 comparing both optical and electrical performance characteristics with lines of figure of merit for reference. Specifically, maximum transmittance  $T_{max}$  (current literature displays values primarily in the visible spectrum), sheet resistance, figure of merit  $\Phi_{TC}$ , and fill factor  $\Psi$  (if applicable) are all included in the table. Figure 2.2 illustrates the large advantage a mesh conductor has over the other options in terms of the electrical performance, where every data point is below  $R_s = 1 \Omega/sq$ , entirely due to geometry, and the bulk conductivity of copper and silver. In addition, the reference lines in Fig. 2.2 show what combinations of sheet resistance and transmittance are required to achieve higher performance by the definition of the figure of merit, showing the mesh outperforms the TCO in every realistic case.

The trade off between transparency and sheet resistance that has been mentioned several times throughout this manuscript can be verified in Fig. 2.2 as there are no points in the bottom right corner. Sheet resistance under  $0.5 \Omega/sq$  with transmittance greater than 90% is not a physical limitation of transparent conductor since the mesh allows the transmittance to be tuned by adjusting the fill factor. Instead, the limit is most likely due to fabrication and the requirements for the individual applications.

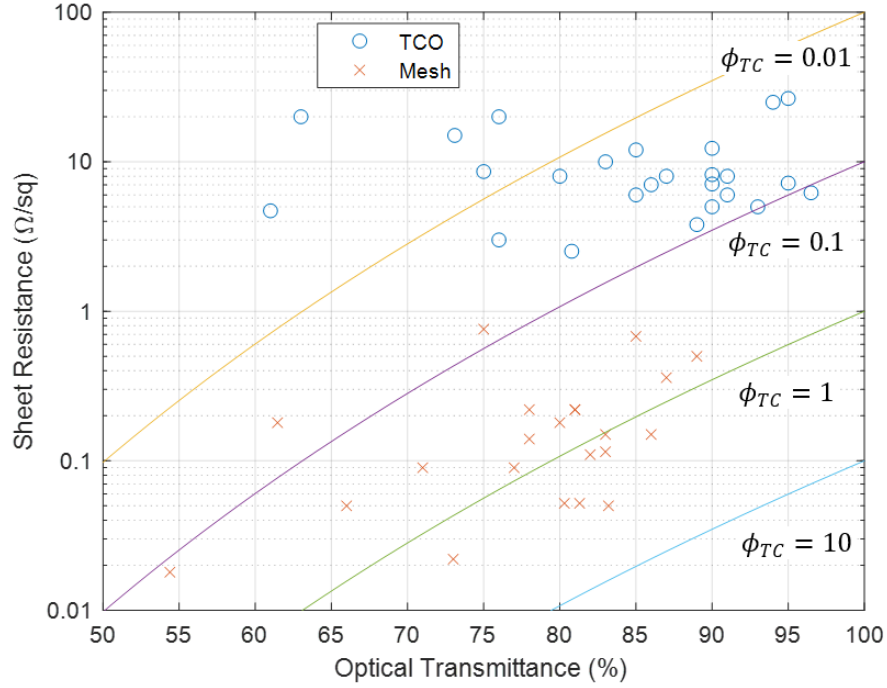


Figure 2.2: Reported optically transparent conductors with lines of constant figure of merit  $\phi_{TC}$  at 0.01, 0.1, 1, and 10. Note: not all conductors are the same thickness, material, etc. [12]

### 2.3 Optically Transparent Antennas

Following the discussion of transparent conductors, the remainder of the manuscript will be dedicated to their application of transparent antennas, and the effects the conductors have on antenna performance. Many groups within the antennas community have studied the radiation of antennas using the transparent conductor. The fundamental goal of these studies is similar to the work in the material science community optimizing the performance of transmittance and conductivity. In RF applications, the challenge has been to identify a conductor to display high conductivity such that the conductor thickness is greater than the skin depth, while simultaneously being transparent to incident light.

### 2.3.1 The Early Periods

Optically transparent antennas started in 1987 with the idea of a transparent, unobtrusive antenna on vehicles to receive radio station signals and to replace the typical monopole antennas. The first transparent antenna was described in a patent which proposed a broadband antenna to receive FM, and even TV broadcast signals from 76-222 MHz to be implemented on vehicle windows using a transparent film. The patent was filed by *Central Glass Company, Limited* in Ube, Japan. The patent discussed methods to increase conductivity of transparent conducting films to support the antenna radiation requirements for both radio and television broadcast waves [43]. The 1990s marked the beginning of the field of optically transparent antennas with applications ranging from transparent antennas on windows to antennas on satellites [44, 45, 46, 47, 48, 49, 50]. Specifically, in 1991 and 1992, the first published papers proposed an antenna utilizing parallel wires at 1 GHz with applications geared toward mobile wireless communications on glass [44, 51]. Also, in 1992, General Motors (GM) filed a patent for a transparent conducting film antenna implemented on a vehicle window glass. The patent discussed that increasing the thickness will increase the conductivity, but in turn diminish the transparency [45]. The challenges discussed in the first three transparent antenna publications demonstrated trade-offs between simultaneous high gain and transparency which has been driving innovations in research thus far.

NASA has also shown interest in transparent antennas. In 1993, a reference manual for the NASA Charging Analyzer Program (NASCAP) included a section mentioning the necessity for antennas that can be largely transparent to allow light and particles to move freely in space [46]. Later, NASA also presented a feasibility study of optically transparent patch antennas at 2.3 GHz (microstrip fed) and 19.5 GHz (probe fed) using AgHT (silver coated polyester film) for satellite communications, the first of its kind [48].

Moving into the 2000s, the first ITO antenna papers began to be published. The first ITO antenna was fabricated on Corning 7059 glass, operated at 5.8 GHz for wireless communications, and exhibited gains 10 dB less than an aluminum design of the same geometry

due to the ohmic losses inherent in ITO [52]. Later in 2002, a patent by Harris Corporation introduced an optically transparent phased array antenna for satellite communications made of indium tin oxide [53].

### 2.3.2 Transparent Conductors for Antennas

Of all the materials discussed above, many of these have been exploited by researchers for optically transparent antennas. Antennas have been presented on glass and plastic substrates using AZO [54], AgHT [55, 56, 57, 15, 58, 59, 60, 61, 62, 63], ITO [35, 64, 65, 66, 67], silver nano-wires [68, 69], Fluorine Tin Oxide (FTO) [70, 71], graphene [72, 73, 74], Indium Gallium Zinc Oxide [75], Silver inkjet printing [76, 77, 78, 31, 79], and lastly, Copper/Silver mesh [80, 81, 82, 83, 84, 85, 41, 86, 87, 88, 89, 90, 91, 92, 93, 94]. Of the conductors listed, the mesh, ITO, and AgHT are the most commonly used for optically transparent antennas. Figure 2.3 presents a literature survey of antenna gain versus the operating frequency for the top three cited conductors. The trend seen in the gain is consistent with the fact that the mesh antenna conductivities are larger than ITO, AgHT, and other comparable materials.

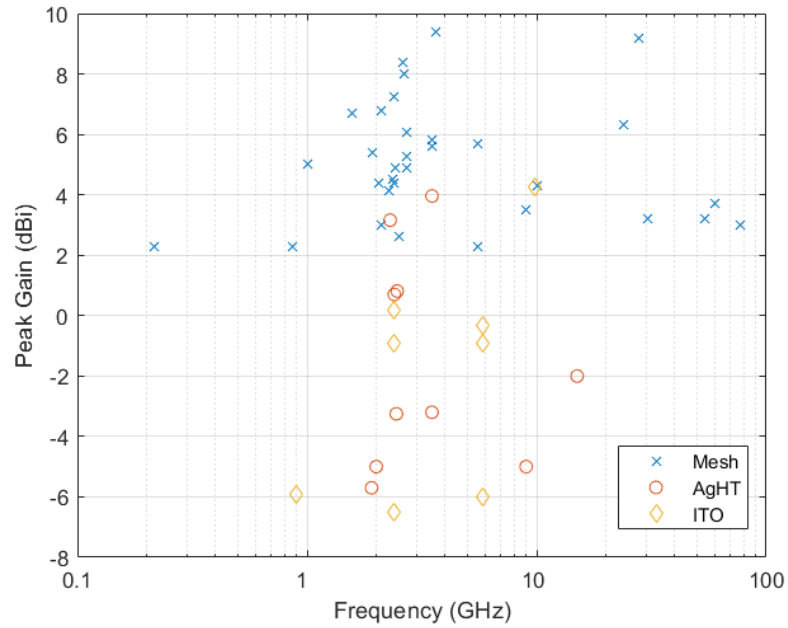


Figure 2.3: Comparison of antenna gains for the mesh, ITO, and AgHT transparent conductors. (Note: variety of antenna topologies are used including one-layer and two-layer metallizations.) [12]

Of the transparent antennas, almost 50% of the use the meshed conductor as the radiating element and ground plane (if applicable). TCO antennas are not typically used in the mmW regime because the skin depth requirement is not met (see Fig. 3.57) resulting in the poor antenna performance shown in Fig. 2.3.

Many papers compare transparent antennas directly to solid antenna of the same dimensions to look at the degradation of performance as a result of introducing a less conductive radiating element. In an experiment comparing an AgHT transparent circular monopole to an aluminum monopole from 1-8.5 GHz, the gain was consistently 5 dB less over the entire band. This observation was suggested as reasonable since aluminum is much more conductive than AgHT-4, and thus has a higher gain potential with less ohmic losses [56]. Also, TCO antennas have been shown to radiate with a lower radiation efficiency due to the high sheet resistance using ITO films at 9.85 GHz [66]. Comparisons of mesh, ITO, and polyester coated film antennas have been explored at 2.5 GHz, discussing trade-offs of the transparency and the radiation properties of the patch antennas on ITO and meshed [95].

TCF antennas lack the performance suitable for low-loss applications. To increase the efficiency, researchers are attempting to increase the conductivity of the radiating element while maintaining high optical transmittance. Using a gold nanolayer deposition technique has been shown to improve the efficiency of a single layer circular monopole at 3 GHz and 8 GHz compared to the same antenna made with ITO [96]. Also, adding a conductive layer where the current density is highest, i.e. a highly conductive strip on the edge of a AgHT coplanar patch antenna, increased antenna efficiency by 30% and increased the antenna gain from 0 dBi to 5 dBi [97]. Like the study discussed above, research to increase efficiency on AgHT-4 film antennas used highly conductive edges to increase the efficiency. The methodology is to reduce the sheet resistance on the edges where the current builds up most to increase the radiating efficiency of the antenna. [98]. This research could potentially be applied to the mesh antennas, aligning the mesh lines where the current density is highest. As a result, this method will allow for higher radiation efficiency, as well as potentially higher overall transmittance since the low current density locations will have a less dense mesh.

For many transparent antenna designers, the main drawback is finding a method to fabricate an antenna on glass. As a result, industry and academic partners have developed manufacturing techniques of transparent conductors on glass. Further developments in the field will require for rapid prototyping and readily available materials. Roll-to-roll manufacturing at Binghamton University's Center for Advanced Microelectronics Manufacturing (CMM) is advancing the field of transparent conductors for high throughput, low-cost manufacturing [35, 10].

### 2.3.3 Antenna Topologies

Using the materials previously discussed, antennas have been implemented as optically transparent vary between the standard directional [7, 42] and omnidirectional antenna topologies. The antennas range from transparent microstrip patch, monopole, and even

a few examples of patch antenna arrays utilizing the materials listed in the previous section. Many of the TCO monopole antennas have been made with alternate geometries to maximize the performance, for example a complementary split ring resonator [61]. The varying geometries look to alternate the current distribution, but without a conductor with required skin depth, the performance will continue to suffer. In addition, circular and triangular patches have been studied to exploit circular polarization. Impedance matching to such antennas can be challenging. As a result, feeding mechanisms have also been explored. Using passive coupling between the feed and circular/triangular antenna element has shown to provide acceptable matching [87].

For two-layer antennas, however, different challenges have been presented. When using a mesh as the conductor for antennas with ground planes, challenges arise in alignment for two-layer mesh designs. Since typically the mesh must be fabricated using photolithography and etching, alignment is important in this process. As a result, the effects of misalignment have been presented which show  $< 1\%$  change in resonant frequency and minimal changes in antenna gain [41]. A copper honeycomb mesh, is presented, displaying the transmission and the antenna performance of a patch at 77 GHz, Fig. 2.4a. The antenna used the honeycomb mesh since the typical rectangular mesh limits the currents to flow in orthogonal directions [42]. The honeycomb mesh has not been as widely studied but the results presented show great potential providing the natural current paths, like the solid structure. These studies show large potential to make transparent antennas as a staple in the engineering design for future applications. At 60 GHz, a patch antenna array in Fig. 2.4b was fabricated and measured using a silver mesh showing 75% optical transparency with gain of 12 dBi [41, 99]. The feed lines of the antenna array were denser than the patches themselves since the current density is higher in the feed lines. Using a higher density mesh in the feeds showed a decrease in loss in the transmission lines, but also decreased the transparency of the structure.

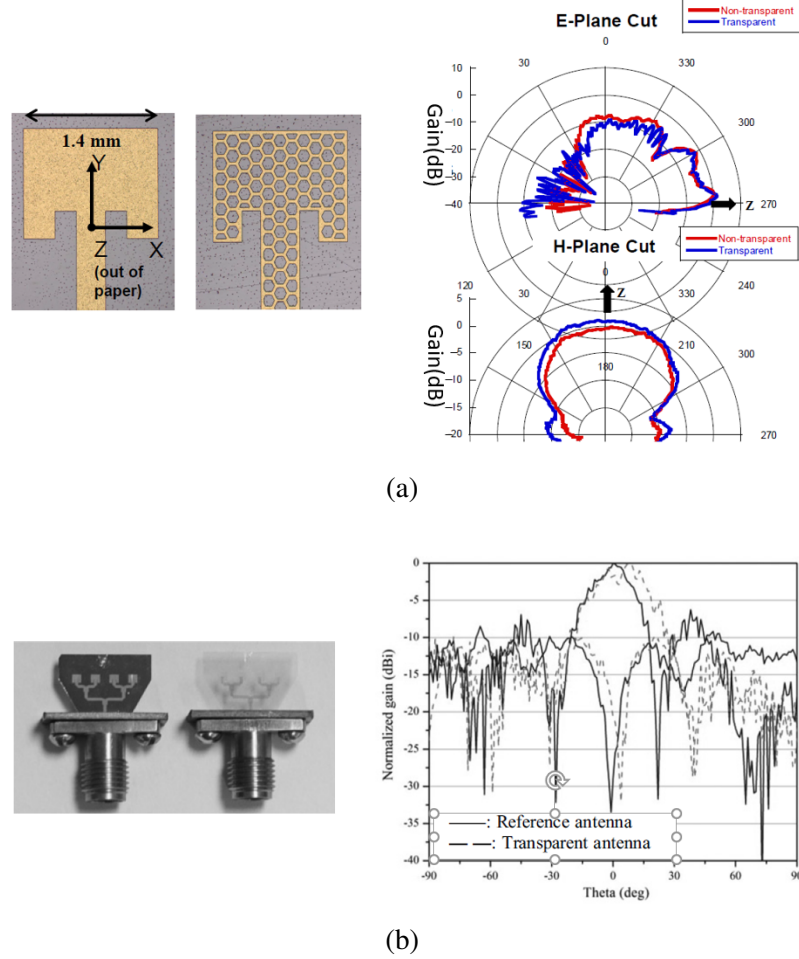


Figure 2.4: State-of-the-art mmW mesh transparent antennas. (a) 80 GHz Honey-comb mesh inset-fed patch antenna [42] (b) 60 GHz Mesh patch array with meshed feed network [41]

### 2.3.4 Antenna Applications

One of the most common applications for optically transparent antennas has been towards applying the antennas on top of solar panels for CubeSats or SmallSats. On systems that are limited to size, weight, and power (SWaP) like satellites, optically transparent antennas prove to be very useful. Typically, antennas require large physical areas on a CubeSat - large dipole antennas are required for UHF and S-band downlink and crosslink communications. Optically transparent, low-profile antennas with minimal blockage of the solar panels can greatly reduce the SWaP and complexity of deployable antennas in orbit. The antennas



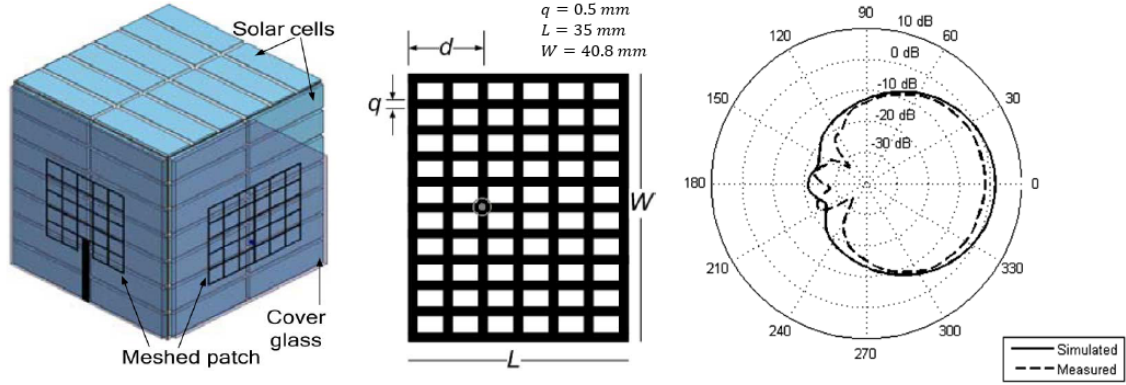


Figure 2.5: (Left) Transparent antenna for integration on CubeSat solar panels. (Middle) Dimensioned model of 2.5 GHz probe-fed patch antenna. (Right) Simulated and measured antenna gain plots at 2.5 GHz [86].

presented in [81] utilized a mesh conductor and provided good electrical performance while maintaining the required level of optical transparency. Research has investigated meshed antennas on satellite solar cells at 2.5 GHz shown in Fig. 2.5 [86]. Though ITO films show very poor performance overall, one study discussing the challenges for ITO patch antennas on Cubesats shows the radiation efficiency versus surface resistance for ITO films. The study displayed a frequency range for optimal performance with 40% efficiency around 5 GHz for an ITO patch antenna with conductor thickness of  $1.2 \mu m$  [100].

Additionally, optically transparent antennas have shown to be useful in the area of radio-frequency identification (RFID) as an unobtrusive tag [15]. The tags can be fabricated as applique antennas that can be stuck onto window, walls, or any surface that would need identification. For an RFID tag, using a TCO can be feasible since short range RFID applications have very relaxed return requirements. As a result, RFID tags have much less strict antenna gain requirements so a lower performing TCO conductor could be used.

Innovations in antenna engineering have steadily progressed in the automotive industry, where many of the early patents discussed optically transparent antennas integrated into automotive windows instead of the large metal-rod monopole antennas. With advancements by GM and other automakers, the next generation FM/AM broadcast antenna looks to be a transparent antenna embedded on the windshield with an isotropic radiation pattern seen

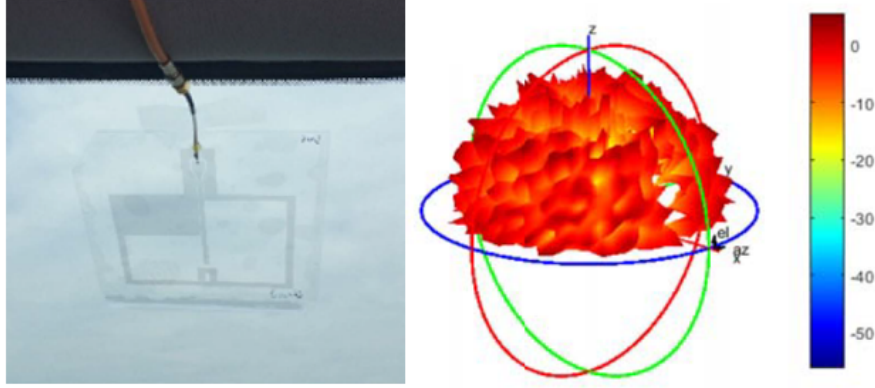


Figure 2.6: (Left) Transparent 717 MHz/2.11 GHz mesh antenna on a vehicle front windshield. (Right) 3D visualization of observed antenna gain at 2.11 GHz [10].

in Fig. 2.6. Consumers have also demanded additional connectivity in their vehicles which has driven designers to integrate GNSS/GPS, 4G and 5G cellular networks, and WiFi bands into cars as well. Automotive antennas have shown the best suited conductor is the mesh as it meets the skin depth requirement over each of the frequency bands, aforementioned [10].

Optically transparent antennas also show great potential in next generation smart phones, watches, televisions, eye-glasses, etc. With the growing interest in wireless connected devices, low profile antennas are essential. As a result, optically transparent antennas have been discussed and presented in many different patents for antennas embedded on the display glass to increase wireless signals [101, 102, 103] Another application, for smart glasses shown in Fig. 2.7, presented effective radiation using a multilayer film of Indium Zinc Tin Oxide/Silver/Indium Zinc Tin Oxide which displayed a bulk conductivity of  $2 \times 10^6$  S/m and a transmittance of 80% [104]. In this example, the antenna is embedded into the glasses lens, which an application that would require a very high level of optical transmittance ( $> 85\%$ ) to be unobtrusive to the user.

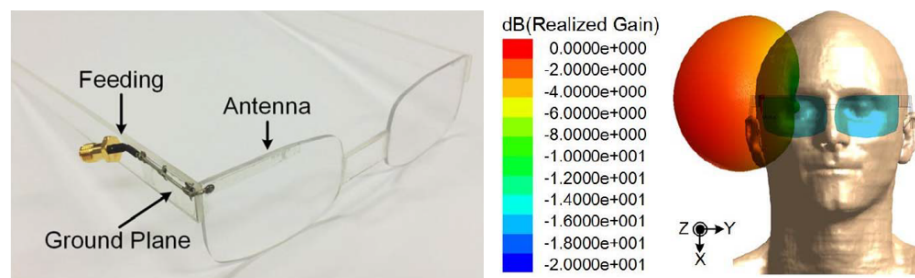


Figure 2.7: Transparent antenna for smart glasses made out of a multilayer film of IZTO/Ag/IZTO at 2.4 GHz [104].

Table 2.1: Published data for each class of optically transparent conductors (transparent in the visible light region). [12]

<i>Conductor</i>	Thickness	$T_{max}$	$R_s$ ( $\Omega/sq$ )	$\phi_{TC} = T^{10}/R_s$	$\Psi$ (mesh only)	<i>Source</i>
AgHT-8	—	0.8	8	0.01342	-NA-	[15]
Antimony TO	—	0.76	20	0.00321	-NA-	[19]
AZO	500 nm	0.9	7.1	0.04911	-NA-	[20]
AZO	—	0.89	3.8	0.06490	-NA-	[19]
AZO	1000 nm	0.9	5	0.06974	-NA-	[21]
AZO	220 nm	0.965	6.2	0.11295	-NA-	[22]
AZO	—	0.96	25	0.02154	-NA-	[23]
BZO	—	0.87	8	0.03105	-NA-	[19]
Cd <sub>2</sub> SnO <sub>4</sub>	—	0.95	7.2	0.08316	-NA-	[19]
CNT	—	0.71	59	0.00055	-NA-	[24]
CNT	—	0.85	500	0.00039	-NA-	[25]
CNT	—	0.85	1000	0.00020	-NA-	[26]
CNT	—	0.85	200	0.00098	-NA-	[27]
CNT	—	0.81	180	0.00020	-NA-	[28]
CNT	—	0.81	310	0.00039	-NA-	[27]
FTO	—	0.9	12.3	0.02835	-NA-	[20]
FTO	—	0.91	8	0.04868	-NA-	[19]
FTO	—	0.83	10	0.01552	-NA-	[29]
FZO	—	0.93	5	0.09680	-NA-	[19]
GaZO	—	0.76	3	0.02143	-NA-	[19]
Graphene	—	0.974	125	0.00615	-NA-	[30]
Graphene	—	0.965	219	0.00320	-NA-	[31]
Graphene	—	0.7	1.35e5	2.1e-7	-NA-	[32]
ITO	250 nm	0.85	12	0.01641	-NA-	[33]
ITO	350 nm	0.731	15	0.00290	-NA-	[33]
ITO	—	0.75	8.6	0.00152	-NA-	[34]
ITO	—	0.9	8.2	0.04252	-NA-	[20]
ITO	—	0.91	6	0.06490	-NA-	[19]
ITO	—	0.84	8	0.02186	-NA-	[22]
ITO/AlSiO <sub>2</sub>	650 nm	0.85	6	0.03281	-NA-	[35]
ITO	—	0.92	11.2	0.03878	-NA-	[22]
ITO/Cu/ITO	183 nm	0.61	4.7	0.00152	-NA-	[34]
IZTO/Ag/IZTO	—	0.8078	2.52	0.04695	-NA-	[7]
IZTO/Ag/IZTO	—	0.86	7.0189	0.03513	-NA-	[6]
IZO	—	0.63	20	0.00049	-NA-	[19]
Copper Mesh	2500 nm	0.87	0.36	0.69007	0.0625	[10]
Copper Mesh	2500 nm	0.81	0.22	0.37890	0.091	[10]
Copper Mesh	2500 nm	0.78	0.22	0.38790	0.090	[10]
Copper Mesh	2500 nm	0.8	0.18	0.59652	0.048	[10]
Copper Mesh	2500 nm	0.86	0.15	1.47534	0.048	[10]
Copper Mesh	2500 nm	0.83	0.115	1.34922	0.0625	[10]
Copper Mesh	2500 nm	0.82	0.11	1.24953	0.063	[10]
Copper Mesh	2500 nm	0.78	0.14	0.59541	0.595	[10]
Copper Mesh	2500 nm	0.77	0.09	0.81408	0.091	[10]
Copper Mesh	2500 nm	0.71	0.09	0.36169	0.091	[10]
Copper Mesh	2500 nm	0.83	Not Given	-NA-	0.091	[36]
Non-Uniform Copper Mesh	—	0.61	0.18	0.04272	-NA-	[7]
Silver Mesh	—	0.544	0.018	0.12610	0.167	[37]
Silver Mesh	—	0.73	0.022	1.95347	0.091	[37]
Silver Mesh	—	0.803	0.052	2.14364	0.063	[37]
Silver Mesh	—	0.813	0.052	2.42606	0.063	[38]
Silver Mesh	—	0.66	0.05	0.3167	0.130	[39]
Silver Mesh	—	0.83	0.15	1.0344	0.049	[39]
Silver Mesh	—	0.89	0.5	0.62363	0.016	[39]
Gold Titanium Mesh	—	0.75	0.76	0.0741	0.048	[40]
Gold Grid	—	0.81	0.2 11	0.55262	-NA-	[41]
Gold Grid	—	0.7	0.015	1.88	-NA-	[42]
Ag Nanowires	—	0.91	23	0.01693	-NA-	[16]

## CHAPTER 3

### PROPERTIES OF OPTICALLY TRANSPARENT CONDUCTORS

---

**Chapter Overview:** This chapter provides the following:

- Derivation of the electromagnetic properties of transparent conducting oxides
  - Relationships between optics, microwave, and classical electromagnetics constants and parameters
  - Comparison of transparent conducting oxides and transparent metal mesh
  - New figure of merit for transparent RF conductors, with analysis transparent conducting oxides and mesh conductor figure of merit graphically represented using parameters from the literature data
- 

As shown in the previous chapter, the conductive performance of transparent conducting oxides are lower than that of a conductive mesh. This chapter will discuss electromagnetic material parameters to explore the frequency relationship of materials over the electromagnetic spectrum. This chapter will also look to find the limitations of transparent conducting oxides and identify the source of the limitation.

Optically transparent conductors must be defined clearly to understand the performance metrics under the electromagnetic environment the materials will be operating. Figure 3.1 shows a simple introductory description of the two operational modes at separate regions of the electromagnetic spectrum. The desired operation of the materials is to be transparent to optical wavelengths  $\lambda_{EO/IR}$  and conductive to RF and millimeter-waves  $f_{RF}$ . Analyzing transparent conductors require transmittance, conductivity, and other parameters to be

clearly defined. The definition of transmittance is typically defined as the ratio of the transmitted and incident wave power/intensity,  $I_t$  and  $I_o$ , respectively. In contrast the definition of conductivity is given by the ratio of the current density to the electric field that allows the flow of current, given by Maxwell's equations. The value of transmittance and conductivity that determines if a material is transparent or conductive is somewhat ambiguous in the literature, the values are obviously desired to be as high as possible for most applications. The problem arises when discussing the transmittance of separate transparent conducting oxides, since the transmittance is based on thickness. In contrast, a conductive with very low sheet resistance  $R_s$ , as described in the previous chapter, is inversely dependent on thickness. This chapter will show the trade-off between transmittance and sheet resistance is clear since the material thickness must be fixed. The conductivity  $\sigma$  at RF and attenuation constant  $\alpha$  at EO/IR must be made in a way to create a high performing transparent conductor, which is a challenge in material science [8].

Transparent conductors can be viewed as an optimization problem, where the parameters being optimized are attenuation  $\alpha$ , conductivity  $\sigma$ , and thickness  $t$ , soon it will be shown that operating frequency also plays a large role. The rest of the chapter will provide relationships between these parameters to find the optimal transparent conductor which maximizes the transmittance at optical wavelengths and minimizes the sheet resistance at RF and millimeter-wave frequencies. The problem this chapter is aiming to solve is to find a maximum value of simultaneous RF conductivity and optical transparency given as  $\phi_{TC}$ , presented is

$$\max(\phi_{TC}(\lambda_{EO}, f_{RF})) \quad (3.1)$$

where  $\phi_{TC}$  is a function of optical absorption, D.C. conductivity, material thickness, as well as both RF and EO-IR operating wavelengths.

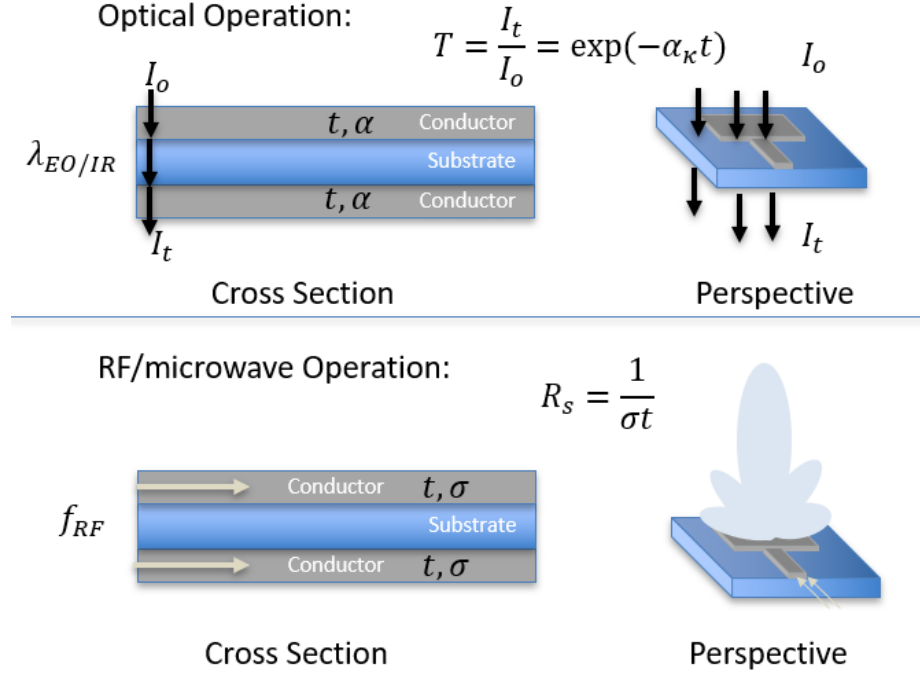


Figure 3.1: RF and Optical Operational Modes (Top) Optical/Infrared operation at  $\lambda_{EO/IR}$  which hold values of transmittance  $T$  with absorption  $\alpha_\kappa$  where desired operation is an optically transparent conductor where an incident electromagnetic wave passes without reflection or absorption (Bottom) RF/microwave operation at  $f_{RF}$  with conductivity  $\sigma$  where the desired operation is a guided wave operation as shown with transverse propagation and resonant antenna radiation.

### 3.1 Classical Electromagnetic Theory

The derivations provide key contextual background for the material properties that allow conductors to be transparent. Though many authors in physics electromagnetics, radio-frequency electromagnetics, and optics use widely different notations, this chapter will utilize a single notation and tie the constants from the separate technical communities back with the most general case to provide the necessary information to understand optically transparent conductors. The following formulation is a combination of work gathered from several electromagnetics, optics, and materials textbooks to draw out the material parameters and characterization over EM spectrum [105, 106, 107, 108, 109]. The following derivation discusses the properties of an electromagnetic wave propagating perpendicu-

larly *through* materials, specifically transparent conductors. Later discussion will extend to propagation between two conductors or inside a transmission line structure.

### 3.1.1 Maxwell's Curl Equations and the Constitutive Parameters

In classical electromagnetics, the constitutive relations are given as

$$\bar{\mathbf{J}} = \sigma \bar{\mathbf{E}}, \quad (3.2)$$

$$\bar{\mathbf{D}} = \tilde{\epsilon} \bar{\mathbf{E}}, \quad (3.3)$$

and

$$\bar{\mathbf{B}} = \tilde{\mu} \bar{\mathbf{H}}. \quad (3.4)$$

The vector quantities are electric current density  $\bar{\mathbf{J}}$ , electric flux density  $\bar{\mathbf{D}}$ , magnetic flux density  $\bar{\mathbf{B}}$ , and known electric and magnetic field vectors  $\bar{\mathbf{E}}$  and  $\bar{\mathbf{H}}$ , respectively. Each of the constitutive relations relate a field quantity to a frequency dependent material property, permittivity  $\tilde{\epsilon}$  or permeability  $\tilde{\mu}$ , and conductivity  $\sigma$ . Complex permittivity and permeability are the material parameters which can describe a material parameter over the entire electromagnetic spectrum. The constitutive material parameters are typically given in real and imaginary parts and both the real part and imaginary part are a function of frequency (or wavelength). Typically, in many micro-/millimeter-wave circuits and optics applications, the materials are assumed to be non-magnetic, and  $\tilde{\mu} \approx \mu_0 = 4\pi \times 10^{-7} \text{ H/m}$ , which tends to simplify analysis and make for clearer representations of field quantities. The non-magnetic approximation will be assumed for the remainder of this thesis.

The following derivations will use  $j = \sqrt{-1}$  to represent complex values, differential curl operator ( $\nabla \times \bar{\mathbf{A}}$ ) and divergence of a vector ( $\nabla \cdot \bar{\mathbf{A}}$ ) where  $\bar{\mathbf{A}}$  is a complex spatial vector quantity. Using the vector notation, the Maxwell's time harmonic, complex, spatial,



equations in a source-less region gives

$$\nabla \times \bar{\mathbf{H}} = \sigma \bar{\mathbf{E}} + j\omega (\epsilon' - j\epsilon'') \bar{\mathbf{E}}, \quad (3.5)$$

$$\nabla \times \bar{\mathbf{E}} = -j\omega \tilde{\mu} \bar{\mathbf{H}}, \quad (3.6)$$

$$\nabla \cdot \bar{\mathbf{D}} = 0, \quad (3.7)$$

and

$$\nabla \cdot \bar{\mathbf{B}} = 0, \quad (3.8)$$

with radial frequency  $\omega = 2\pi f$ , where  $f$  is the frequency and wavelength  $\lambda = \frac{c}{f}$ , and  $c$  is the speed of light in vacuum. Maxwell's equations allow the representation of a complex permittivity as a function of  $\epsilon'$ ,  $\epsilon''$ , and  $\sigma$ . Rearranging terms in (3.5) leads to

$$\nabla \times \bar{\mathbf{H}} = j\omega \left( \epsilon' - j\epsilon'' - j\frac{\sigma}{\omega} \right) \bar{\mathbf{E}}. \quad (3.9)$$

Since the dielectric loss ( $\omega\epsilon''$ ) and the conductive loss ( $\sigma$ ) are indistinguishable, the effective conductivity

$$\sigma_e = \omega\epsilon'' + \sigma, \quad (3.10)$$

can be used to simplify the curl equation to

$$\nabla \times \bar{\mathbf{H}} = j\omega \left( \epsilon' - j\frac{\sigma_e}{\omega} \right) \bar{\mathbf{E}}, \quad (3.11)$$

where the complex permittivity is now given as in terms of a relative permittivity  $\epsilon'$  and an effective conductivity as

$$\tilde{\epsilon} = \epsilon' - j\frac{\sigma_e}{\omega}. \quad (3.12)$$

Separating real and imaginary parts lead to the imaginary part of complex permittivity,

$$\text{Im}(\tilde{\epsilon}) = \frac{\omega\epsilon'' + \sigma}{\omega} = \frac{\sigma_e}{\omega} \quad (3.13)$$

The complex permittivity can typically be given in terms of a loss tangent  $\tan \delta_e$  by rearranging (3.12) as,

$$\tan \delta_e = \frac{\omega\epsilon'' + \sigma}{\omega\epsilon'} = \frac{\sigma_e}{\omega\epsilon'} \quad (3.14)$$

but to keep generality, the form will remain in terms of the constitutive parameters. The loss tangent is typically given in RF material data sheets to characterize the loss of the dielectric at given frequencies, typically when  $\sigma = 0$ , but in general the loss tangent does include  $\sigma$  as shown in (3.14) [105]. For completeness, similar analysis can be performed on Maxwell's curl equation of  $\bar{\mathbf{E}}$  in (3.6) to achieve the magnetic loss tangent of

$$\tan \delta_m = \frac{\mu''}{\mu'}. \quad (3.15)$$

The magnetic loss tangent, and complex permeability is usually neglected in microstrip circuits since many of the materials are non-magnetic. For ferromagnetic and ferrimagnetic materials, the permeability is not assumed to be  $\mu_0$  but instead is a complex quantity where, similar to complex permittivity, both  $\mu'$  and  $\mu''$  change with frequency. For these materials there is a fundamental limit to how in frequency a material can respond where the higher DC permeability the lower the cut-off frequency when the material reverts back to a nonmagnetic material with  $\mu_0$  [110].

Materials in electromagnetics can be described using a propagation constant  $\gamma$  which describes the attenuation  $\alpha$  and phase  $\beta$  of the propagating wave. The propagation constant which can be written in the most general form as

$$\gamma = \alpha + j\beta = \sqrt{j\omega\tilde{\mu}\tilde{\epsilon}} = \sqrt{j\omega\tilde{\mu}(\epsilon' - j\frac{\sigma_e}{\omega})}, \quad (3.16)$$

where  $\alpha$  and  $\beta$  can be given as

$$\alpha = \text{Re}\{\gamma\} = \omega \sqrt{\tilde{\mu}\epsilon'} \left[ \frac{1}{2} \left( \sqrt{1 + \left( \frac{\sigma_e}{\omega\epsilon'} \right)^2} - 1 \right) \right]^{1/2}, \quad (3.17)$$

and

$$\beta = \text{Im}\{\gamma\} = \omega \sqrt{\tilde{\mu}\epsilon'} \left[ \frac{1}{2} \left( \sqrt{1 + \left( \frac{\sigma_e}{\omega\epsilon'} \right)^2} + 1 \right) \right]^{1/2}. \quad (3.18)$$

Since the attenuation and phase constant directly depend on  $\sigma_e$ , as the effective conductivity term decreases, so does the attenuation as shown in Fig. 3.2 which shows the attenuation constant versus effective conductivity. For an EM wave normally incident to an interface, decreasing the effective conductivity, decreases the attenuation constant and thus decreases the transmittance through the material (holds for frequencies at all ranges). In addition, the attenuation increases, as frequency (wavelength) increases.

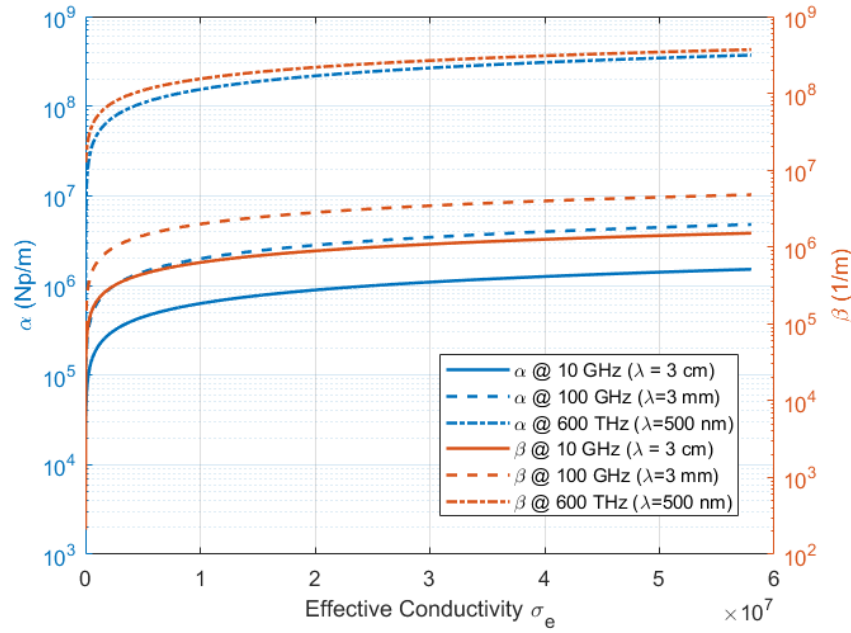


Figure 3.2: Relationship between attenuation constant  $\alpha$  and phase constant  $\beta$  for propagation perpendicularly through a metal versus effective conductivity assuming for simplicity,  $\epsilon' = \epsilon_0$  and  $\tilde{\mu} = \mu_0$ . For illustration of the behavior of the effective conductivity,  $\sigma$ ,  $\tilde{\mu}$ ,  $\epsilon'$ , and  $\epsilon''$  assumed to remain constant over all frequencies.

The propagation constant for a wave travelling in the positive  $z$  direction is expressed

in the form

$$\exp(\gamma z) = \exp(-\alpha z) \exp(-j\beta z),$$

where  $z$  is the distance travelled. This means that for forward propagation, the attenuation must be small as the phase constant is used to provide the phase velocity  $v_p = \omega/\beta$  and the wavelength  $\lambda = 2\pi/\beta$ . Figure 3.2 shows the relationship between  $\alpha$  and  $\beta$  at different frequencies, varying the effective conductivity. Given the RF/mm-Wave frequency of 10 GHz and 100 GHz respectively, the transparent conductor is desired to have high conductivity, high conductivity means high  $\alpha$  from (3.17). It is important to note again the results presented are for a field propagating perpendicularly through a material, not a guided wave structure like a transmission line. At the optical wavelengths of 500 nm, to be transparent the attenuation constant and/or thickness of the material must be very small to avoid absorption; thus, the effective conductivity must also be very small. The relationship, given a fixed thickness, presents a conclusion that a transparent conducting oxide must have decreased effective conductivity to allow the transmission of optical wavelengths through the metal. The decreased effective conductivity at optical wavelengths, and conductive properties at microwave frequencies present in transparent conducting oxides like ITO confirms the frequency variation of the constitutive parameters over the electromagnetic spectrum. The variation of permittivity is explained in electromagnetics as the dielectric response, polarizability, or dispersion, which explains the interaction between the applied electric field and polarization of the atoms to create the bound charge, or dipole moments change in response to the applied field, which also changes with frequency. Going back to Fig. 3.1, the results suggest the parameters given at both regions of the spectrum are related based on the frequency response of the material. The relationships are due to the dielectric response and polarizability, which determines how materials behave in different regions of the spectrum.

### 3.1.2 Dielectric Response and Polarizability for TCOs

In order to explain how a material can behave as a conductor and reflect incident microwave frequencies, while transmitting optical wavelengths, the dielectric response and electron polarizability must be introduced. Figure 3.2 displays that for a conductor to be transparent to an incident electromagnetic field, the effective conductivity must be "small" in the optical region of the spectrum to avoid attenuation of the waves incident on the material, which increase with increasing  $\sigma_e$ .

Analysis for the frequency dependence of materials leads back to the permittivity function  $\tilde{\epsilon}$  and its physical definition as a relationship between the electric field and the electric flux density in (3.3). The frequency response of these conductors with changing material properties at different frequencies is due to electric polarizability, or the behavior of bound charge at different frequencies, which is how the permittivity as a function of frequency is derived. The polarizability of materials is extremely important in understanding how transparent conducting oxides can have high conductivity in one region (i.e RF, microwave, millimeter-wave) of the spectrum, but not in other regions of the spectrum (i.e infrared, optical, etc.).

The electric susceptibility  $\chi_e$ , a dimensionless quantity that influences the electric permittivity and accounts for bound charge, is defined by the following derivation as the relationship between the electric polarization vector  $\bar{\mathbf{P}}$  and the electric flux density  $\bar{\mathbf{D}}$  as

$$\bar{\mathbf{D}} = \epsilon' \mathbf{E} + \bar{\mathbf{P}}, \quad (3.19)$$

and the electric polarization vector  $\bar{\mathbf{P}}$  is given as

$$\bar{\mathbf{P}} = \epsilon_0 \tilde{\chi}_e \bar{\mathbf{E}}, \quad (3.20)$$

where  $\tilde{\chi}_e$  is the complex valued proportionality constant that changes with frequency shown

as

$$\tilde{\chi}_e = \chi'_e - j\chi''_e, \quad (3.21)$$

where  $\chi'_e$  and  $\chi''_e$  are the real and imaginary parts of electric susceptibility, respectively. Physically, the electric polarization vector is a term accounts for the creation of the dipole moments that occur as a result of an applied electric field, which in turn supplements the electric flux density with the relationship in terms of electric susceptibility. Substituting in  $\bar{\mathbf{P}}$  into (3.19) gives

$$\bar{\mathbf{D}} = \epsilon_0 \bar{\mathbf{E}} + \epsilon_0 \tilde{\chi}_e \bar{\mathbf{E}} = \epsilon_0 (1 + \tilde{\chi}_e) \bar{\mathbf{E}}. \quad (3.22)$$

and combining (3.3) and (3.22) results in permittivity as function of electric susceptibility

$$\tilde{\epsilon}_\chi = \epsilon_0 (1 + \tilde{\chi}_e) = \tilde{\epsilon}. \quad (3.23)$$

The dispersion relations give an approximation to the dielectric response due to the electric susceptibility interactions given in Fig. 3.3, where dipole  $\chi_{ed}$ , ionic  $\chi_{ei}$ , and electronic  $\chi_{ee}$  interactions of electrical susceptibility. The solutions to the interactions are outside the scope of this thesis, but the overall concept is very important. The electric susceptibility describes the frequency dependence of both the real and imaginary parts of the dielectric function  $\tilde{\epsilon}$ . The DC through UV material properties are difficult to come across over the entire range of frequencies, which require different operational methods to measure and characterize the materials, but the frequency dependent dispersive nature of materials is similar to the sample behavior shown in Fig. 3.3, where the location and number of inflection points will vary greatly between materials.

Using the dispersion relations, and electron mass transfer theory, effective conductivity can be given in terms of electron charge  $q$ , electron density  $N$ , and electron mass  $m$  as

$$\sigma = \frac{q^2 N}{m}, \quad (3.24)$$

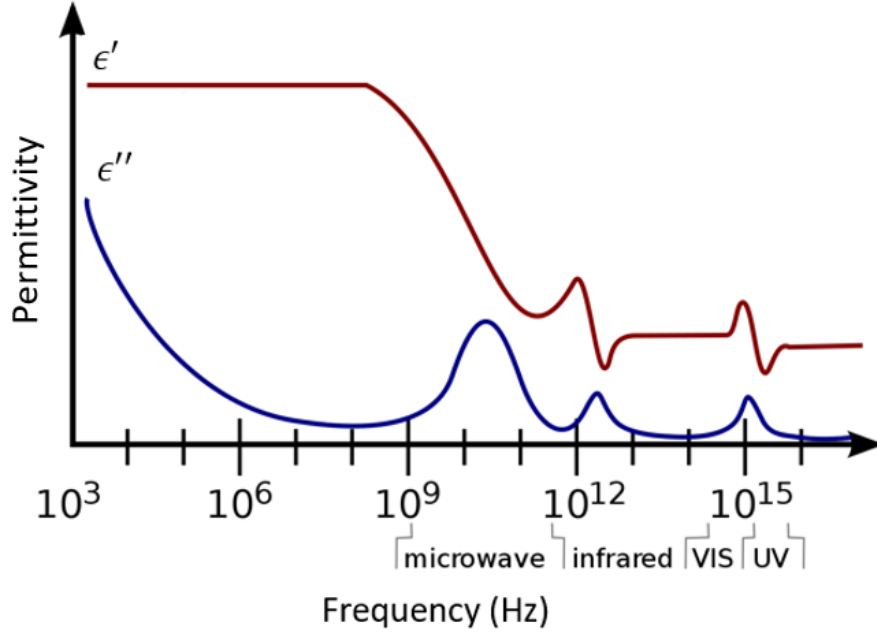


Figure 3.3: Dispersion of materials with frequency over the entire electromagnetic spectrum which shows a changing real and imaginary part of electric permittivity over the entire EM spectrum [105]. Adapted from [111].

and continuing the formulation of electron mass transfer, modelling the material's polarization as mass-spring damper system also known as the Lorentz model. Using the Lorentz model, the inflection points of the materials permittivity function, using the mechanical spring-mass damper model, is called the plasma frequency  $\omega_p$ , defined as

$$\omega_p = \sqrt{\frac{q^2 N}{\epsilon' m \tau}} = \sqrt{\frac{\sigma}{\epsilon' \tau}}, \quad (3.25)$$

where  $\tau$  is the electron relaxation time. Sometimes the plasma frequency is referred to as a plasma wavelength  $\lambda_p$  in optics literature by the relationship by the speed of light  $c$  and plasma frequency  $\omega_p$  as

$$\lambda_p = \frac{2\pi c}{\omega_p}. \quad (3.26)$$

The plasma frequency is the highest possible frequency that a density of electrons can respond to as a conductor. When a wave is incident with a higher frequency than the material's plasma frequency, the electrons response is minimal, and their presence will

only modify the phase velocity, or the rate at which the phase of the wave propagates in space given as  $v_p = \frac{\omega}{\beta}$ . The effects of plasma brings attention to the individual ion and electron interactions in the presence of an electromagnetic wave. Following the derivations shown in [105] by the differential equation

$$m \frac{\partial^2 \vec{r}}{\partial t^2} + \frac{m}{\tau} \frac{\partial \vec{r}}{\partial t} + m\omega_0^2 \vec{r} = -q\vec{E}, \quad (3.27)$$

where  $\tau$  is the relaxation time and  $m\omega_0^2$  is the restoring force. Solving the differential equation (derivation shown in [105]) allows one to arrive at

$$\frac{\vec{P}}{\vec{E}} = \frac{\sigma_e}{(\omega_0^2 - \omega^2) + j\omega\tau^{-1}} \quad (3.28)$$

where  $\tau$  is electron relaxation time. Using (3.23) and (3.22) gives the Lorentz model [105] of the permittivity  $\tilde{\epsilon}_L$  as

$$\tilde{\epsilon}_L = \epsilon' \left( 1 + \frac{\omega_p^2}{(\omega_0^2 - \omega^2) + j\omega\tau^{-1}} \right) \quad (3.29)$$

For metals, electrons are free because they are not bound to a nucleus. For this reason, the restoring force  $m\omega_0^2$  is negligible, hence, there is no natural frequency  $\omega_0$ . Using the fact that there is no natural frequency brings the Drude-free-electron model. Using the Drude model [112], the natural frequency  $\omega_0 = 0$  in (3.29) allows the Drude approximation for complex permittivity  $\tilde{\epsilon}_D$  to become

$$\tilde{\epsilon}_D = \epsilon' \left( 1 - \frac{\omega_p^2}{\omega^2 - j\omega\tau^{-1}} \right), \quad (3.30)$$

which is valid when free electrons dominate the conductive behavior, rather than dielectric resonances.

Since this representation is only a model, the result does not describe all conductors or materials, since many materials, as shown in Fig. 3.3, have multiple resonances causing



the model to break. In this case, the general Lorentz model can be used using the sum of resonances and requires more characterization outside the scope of the work presented.

Rearranging the analysis to vary the conductivity versus the plasma frequency can also been shown. Using the equation for complex permittivity (3.12) combined with permittivity with plasma effects (3.30) using the Drude model for metals, one can arrive at

$$\sigma_e \approx \frac{\omega_p^2 \tau}{\omega^2 \tau^2 + 1} \epsilon', \quad (3.31)$$

and

$$\sigma \approx \omega_p^2 \tau \epsilon', \quad (3.32)$$

which allows the conclusion, the only way to drive down the plasma frequency for a TCO, allowing the material to be simultaneously transparent at optical frequencies and conductive at micro-/millimeter-wave frequencies, is to reduce the conductivity since the  $\omega_p$  and  $\sigma$  are directly related. The phenomena is evident in many of the modern day transparent conducting oxides such as indium tin oxide, aluminum zinc oxide, and many others. As much as materials scientist work to drive down the plasma frequency, (3.31) shows that doing so will also simultaneously drive down conductivity. The reduction in conductivity poses a large problem in micro-/millimeter wave circuits due to skin depth losses.

The following work lends a belief to some of the conductive limits to transparent conducting oxides, which must have a lower plasma frequency (higher plasma wavelength) than that of the light that is desired to be transmitted. Table 3.1 shows typical metals conductive and plasma frequency, where the conductivity decreases at plasma frequency decreases. This result is the core phenomena that governs how transparent metals, like transparent conducting oxides, behave. *No matter what community is researching the materials, the material parameters discussed, as in resistivity, conductivity, electron mobility, band-gap, etc., the transparent conducting oxides all fall back to the direct relationship in the decreased conductivity and the decrease in plasma frequency which allows the materi-*

Table 3.1: Typical metals with comparison to transparent conducting oxides showing the direct relationship between D.C. conductivity and plasma frequency.

Metal	D.C. Conductivity (S/m)	Plasma Wavelength (nm)	Plasma Frequency (THz)
Copper	$5.813 \times 10^7$	114.5	2620
Gold	$4.098 \times 10^7$	137.32	2185
AZO	$\approx 1.562 \times 10^5$	$\approx 900$	$\approx 333$
ITO	$\approx 1.000 \times 10^4$	$\approx 1500$	$\approx 200$

*als to be conductive at RF and transparent at optical frequencies.*

### 3.1.3 Optics Relation to Constitutive Parameters

Since transparent conductors occupy both RF and optical regions, a relation of standard optics parameters such as index of refraction, transmittance, reflectance and absorbance in terms of the constitutive parameters in the following formulation to avoid confusion in notation will be useful.

Beginning the formulation, the most common material parameter in optics is the index of refraction  $n$ . The relationship between  $n$  and  $\epsilon$  and  $\mu$  as

$$n = \sqrt{\frac{\epsilon' \mu'}{\epsilon_0 \mu_0}} = \sqrt{\frac{\epsilon'}{\epsilon_0}}, \quad (3.33)$$

when using  $\tilde{\mu} = \mu_0$ . The index of refraction is effectively a quantity of how the speed of propagation slows in dense materials. In addition, the refractive index gives the angle of refraction of incident light going from one medium to the next. Snell's law is given as

$$n_1 \sin \theta_1 = n_2 \sin \theta_2, \quad (3.34)$$

where  $n_1$  and  $n_2$  are the respective index of refraction of the two materials while  $\theta_1$  is the incident angle of the incoming wave to the interface, while  $\theta_2$  is the refracted, outgoing angle.

Like the constitutive parameters, complex index of refraction is given as

$$\tilde{n} = n - j\kappa \quad (3.35)$$

where the real part  $n$  is the standard index of refraction above, and  $\kappa$  is the extinction coefficient or the loss term. In general, the index of refraction in the most general form can be expanded in terms of the constitutive parameters as

$$\tilde{n} = n - j\kappa = \sqrt{\frac{\tilde{\epsilon}\tilde{\mu}}{\epsilon_0\mu_0}} \quad (3.36)$$

and inserting  $\tilde{\epsilon}$  and  $\tilde{\mu}$

$$\tilde{n} = \sqrt{\left(\frac{\epsilon' - j\epsilon'' - j\sigma/\omega}{\epsilon_0}\right) \left(\frac{\mu' - j\mu''}{\mu_0}\right)}. \quad (3.37)$$

Squaring both sides of (3.37) and again assuming non-magnetic material  $\tilde{\mu} = \mu_0$  yields,

$$\tilde{n}^2 = n^2 - \kappa^2 - j2n\kappa = \left(\frac{\epsilon' - j\epsilon'' - j\sigma/\omega}{\epsilon_0}\right), \quad (3.38)$$

and equating real and imaginary parts gives

$$\epsilon'/\epsilon_0 = n^2 - \kappa^2 \quad (3.39)$$

$$(\omega\epsilon'' + \sigma)/\epsilon_0 = 2\omega n\kappa \quad (3.40)$$

and using the relationship where  $\sigma_e = \omega\epsilon'' + \sigma$  (thus the imaginary part of complex permittivity),

$$\sigma_e = 2\omega n\kappa\epsilon_0. \quad (3.41)$$

Solving the system of equations from (3.40) and (3.41) allows one to arrive at the following

conclusions for  $n$  and  $\kappa$ ,

$$n = \left[ \frac{1}{2} \left( \sqrt{\left( \frac{\epsilon'}{\epsilon_0} \right)^2 + \left( \frac{\sigma_e}{\omega \epsilon_0} \right)^2} + \frac{\epsilon'}{\epsilon_0} \right) \right]^{1/2}, \quad (3.42)$$

$$\kappa = \left[ \frac{1}{2} \left( \sqrt{\left( \frac{\epsilon'}{\epsilon_0} \right)^2 + \left( \frac{\sigma_e}{\omega \epsilon_0} \right)^2} - \frac{\epsilon'}{\epsilon_0} \right) \right]^{1/2} \quad (3.43)$$

which agrees with a similar derivation with notation changes in [113]. For metals, these relationship will follow the Drude model the versus frequency since  $n$  and  $\kappa$  are dependent on  $\tilde{\epsilon}_D$ . Both forms have a plasma frequency that approximates where the material will reflect or transmit incident fields, all that is needed is to substitute (3.30) into (3.37). Since  $\tilde{n}$  is derived from permittivity, the frequency dependence of the complex refractive index is obvious. Furthermore, the material parameters in terms of the constitutive parameters are useful to gain insights on how  $n$  and  $\kappa$  are directly related to the widely used material parameters in classical electromagnetic theory and how the dispersion relationships carry over to these parameters as well.

Since refractive index is derived from complex permittivity, the Drude model can be substituted for further analysis. The complex refractive index (3.37) can now be represented as the Drude refractive index  $\tilde{n}_D$  shown as

$$\tilde{n}_D = \sqrt{\frac{\epsilon'}{\epsilon_0} \left( 1 - \frac{\omega_p^2}{\omega^2 + j\omega\tau^{-1}} \right)}. \quad (3.44)$$

The result if the properties are known, will give a basic understanding of the expected transmittance, reflectance, and absorbance as a function of wavelength.

Using the extinction coefficient  $\kappa$ , the optical attenuation constant can be derived. The optical attenuation constant is commonly confused with the attenuation constant in electric field propagation. Since optics typically expresses fields as power quantities, their attenuation constant is similarly a power quantity. The optical attenuation quantity,  $\alpha_\kappa$  is exactly

twice that of the attenuation constant  $\alpha$  for field quantities in (3.17). The discontinuity comes from how  $\alpha_\kappa$  is initially derived as the attenuation of the field incident and transmitted intensities,  $I_o$  and  $I_t$ , respectively. The field intensity  $I = |E|^2$  and the ratio is given in terms of power, instead of the fields. The expression used for attenuation is given as

$$\alpha_\kappa = \frac{4\pi\kappa}{\lambda} = \frac{4\pi}{\lambda} \left[ \frac{1}{2} \left( \sqrt{\left(\frac{\epsilon'}{\epsilon_0}\right)^2 + \left(\frac{\sigma_e}{\omega\epsilon_0}\right)^2} - \frac{\epsilon'}{\epsilon_0} \right) \right]^{1/2} \equiv 2\alpha, \quad (3.45)$$

where

$$I_t/I_o = \exp(-2\alpha z) = \exp(\alpha_\kappa z). \quad (3.46)$$

### 3.1.4 Transmittance, Reflectance, and Absorbance

With a solid understanding of the complex refractive index, the physical quantities the transmittance  $T$ , reflectance  $R$ , and absorbance  $A$  are discussed. Following conservation of energy shown in Fig. 3.4 and expressed as

$$1 = T + R + A. \quad (3.47)$$

Starting with the expression of reflectance (power or magnitude squared of reflection coefficient  $\Gamma = \frac{\tilde{n}-1}{\tilde{n}+1}$ ) of a complex material  $\tilde{n}$  from an incident wave in free space ( $\tilde{n} = n = 1$ ). Since electromagnetic waves have inherent polarization (transverse-electric TE and transverse-magnetic TM), the reflectance on each boundary will vary based on the polarization of the incident light in addition to the material parameters. For normal incidence, the individual interface reflectances are given as

$$\Gamma_{12,23}^2 = \left| \frac{\tilde{n} - 1}{\tilde{n} + 1} \right|^2 = \frac{(n - 1)^2 + \kappa^2}{(n + 1)^2 + \kappa^2}. \quad (3.48)$$

where  $\Gamma_{12,23}^2$  is the reflectance coefficient at both interfaces air-TCO (1-2) and TCO-air (2-

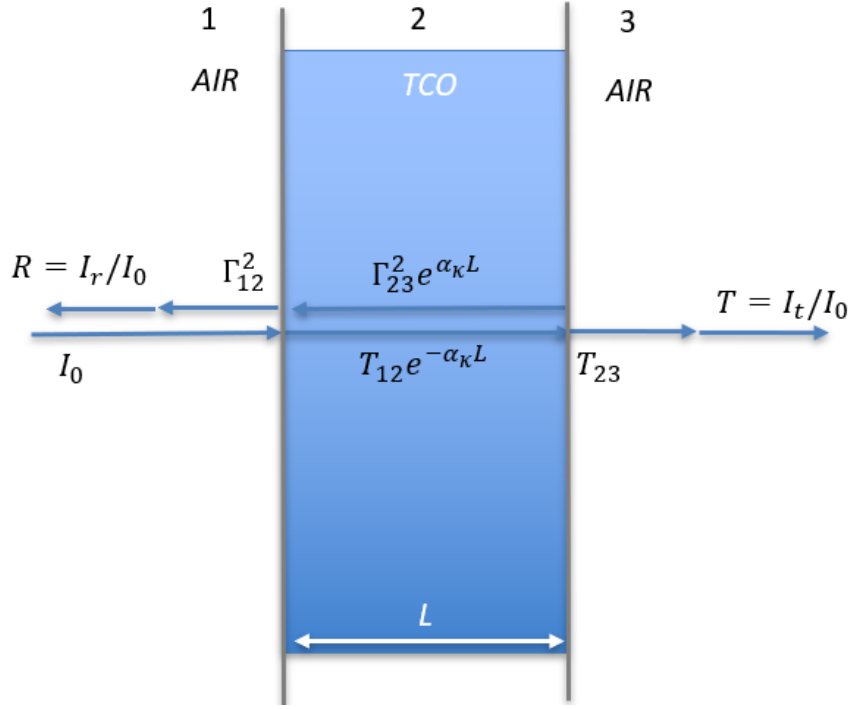


Figure 3.4: Transparent conducting oxide interface displaying incident, reflected, absorbed, and transmitted wave interactions

3) shown in Fig. 3.4. For simplicity and clarity, normal incidence is shown but it is possible to represent the quantities for at an angle of incidence where wave polarization becomes a factor, specifically the when the electric field vector is perpendicular (transverse electric, TE,  $\perp$ ) or parallel (transverse magnetic, TM,  $\parallel$ ) to the plane of incidence.

Since the interfaces are effectively the same due to the material properties and reciprocity,  $\Gamma_{12}^2 = \Gamma_{23}^2$ . Relating this back in terms of the general constitutive parameters substituting (3.42) and (3.43) into (3.48) provides

$$\Gamma_{12,23}^2 = \frac{\sqrt{\left(\frac{\epsilon'}{\epsilon_0}\right)^2 + \left(\frac{\sigma_e}{\omega\epsilon_0}\right)^2 + 1} - \sqrt{2 \left( \sqrt{\left(\frac{\epsilon'}{\epsilon_0}\right)^2 + \left(\frac{\sigma_e}{\omega\epsilon_0}\right)^2} + \left(\frac{\epsilon'}{\epsilon_0}\right) \right)}{\sqrt{\left(\frac{\epsilon'}{\epsilon_0}\right)^2 + \left(\frac{\sigma_e}{\omega\epsilon_0}\right)^2 + 1} + \sqrt{2 \left( \sqrt{\left(\frac{\epsilon'}{\epsilon_0}\right)^2 + \left(\frac{\sigma_e}{\omega\epsilon_0}\right)^2} + \left(\frac{\epsilon'}{\epsilon_0}\right) \right)}}, \quad (3.49)$$

which looks very complex but brings out important results in the relationship between  $R$

and  $\sigma_e$ . Equation (3.49) shows in order to achieve small reflections real part of permittivity ( $\frac{\epsilon'}{\epsilon_0}$ ) must be close to one and the imaginary part ( $\frac{\sigma_e}{\omega\epsilon_0}$ ) must be very small which is what is expected for many materials that are transparent. To add another level of complexity, specular reflectance (angle of incidence same as angle of reflection) also depends on the surface roughness with respect to the applied wavelength. For rough surfaces, however, the reflectance is diffuse and scattered in many directions. Since TCOs are expected to be transparent in the optical region, the surface roughness phenomena is ignored since at RF, surface roughness is negligible. Similarly, the individual transmittances for normal incidence  $T_{12,23}$  can be given as

$$T_{12,23} = 1 - \Gamma_{12,23}^2 = \frac{4}{(n+1)^2 + \kappa^2}, \quad (3.50)$$

which only holds at each interface. For a more complete expression of the full slab including multiple reflections, total reflectance  $R$  is given as

$$R = \frac{\Gamma_{12}^2 + \Gamma_{23}^2 \exp(-2\alpha_\kappa L) + 2\Gamma_{12}\Gamma_{23} \exp(-\alpha_\kappa L) \cos\left(n\frac{2\pi}{\lambda}L\right)}{1 + \Gamma_{12}^2\Gamma_{23}^2 \exp(-2\alpha_\kappa L) + 2\Gamma_{12}\Gamma_{23} \exp(-\alpha_\kappa L) \cos\left(n\frac{2\pi}{\lambda}L\right)}, \quad (3.51)$$

which accounts for the reflection on the first interface, absorption up the second interface and another reflection at the second interface. This slab model for multiple reflections brings an interference terms that is commonly neglected in literature [114]. The phase interference term is given by the  $\cos\left(n\frac{2\pi}{\lambda}L\right)$  in the total reflectance formulation in (3.51). Substituting in the respective values for conductive ( $\omega > \omega_p$ ), transparent ( $\omega < \omega_p$ ), and general lossy materials show the reflectance is dependent on many different parameters, including thickness which causes thin film interference which causes constructive or destructive interference depending on the wavelength of the incident light, material properties ( $\sigma, \mu, \epsilon$ ), and material thickness.

For total transmittance, conservation of energy will hold, so the energy that is not reflected and/or absorbed, will be transmitted through the material. Similarly, transmittance

will include attenuation to account for absorption losses. The total transmittance  $T$  can be shown as

$$T = 1 - R = \frac{T_{12}T_{23} \exp(-\alpha_\kappa L)}{1 + \Gamma_{12}^2 \Gamma_{23}^2 \exp(-2\alpha_\kappa L) + 2\Gamma_{12}\Gamma_{23} \exp(-\alpha_\kappa L) \cos\left(n\frac{2\pi}{\lambda}L\right)}. \quad (3.52)$$

Since  $\Gamma_{12}^2 = \Gamma_{23}^2$ , to clean up the expression, these will be renamed as  $R' = \Gamma_{12}^2 = \Gamma_{23}^2$ , which also allows  $R' = \Gamma_{12}\Gamma_{23}$ . In addition, since  $T_{12,23} = (1 - R')$ , the substitution will be made to simplify the expression further as

$$T = \frac{(1 - R')^2 \exp(-\alpha_\kappa L)}{1 + R'^2 \exp(-2\alpha_\kappa L) + 2R' \exp(-\alpha_\kappa L) \cos\left(n\frac{2\pi}{\lambda}L\right)}. \quad (3.53)$$

For a better picture of the wave behavior inside of the material, Fig. 3.5 shows a transmitted wave exponentially decreasing as the distance  $L$  increases at the rate of its absorption coefficient,  $\kappa$ , described later. As a result, as thickness increases so does absorption in the material.

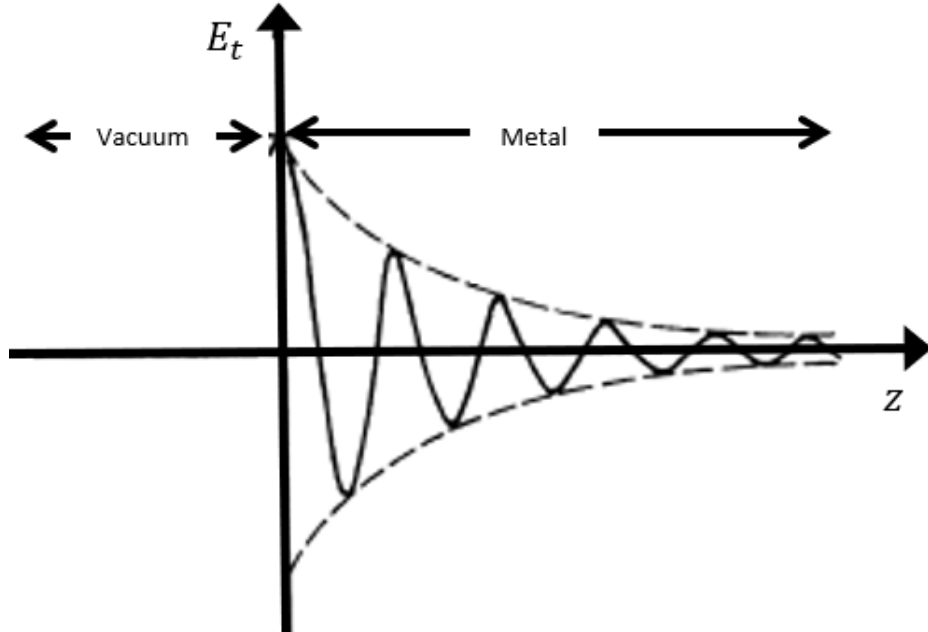


Figure 3.5: Exponentially decreasing electromagnetic wave in an optically dense material. For TCO's the decrease is strong at RF/mm-Wave frequencies, and much less in visible wavelengths.



To simplify the analysis moving forward, the analysis will assume the interference is negligible, as an approximation under non-coherent light sources where the average values of  $T$  and  $R$  are appropriate allow the transmittance to be simplified to (3.54) [114], (which in practice does not hold for monochromatic light source due to multiple reflections, unless the substrate is thick compared to a wavelength) shown as

$$T \approx \frac{(1 - R')^2 \exp(-\alpha_\kappa L)}{1 + R'^2 \exp(-2\alpha_\kappa L)}. \quad (3.54)$$

Equation (3.54) is derived by assuming the  $\frac{2\pi nL}{\lambda}$  in the cosine term from (3.53) is neglected. In general, the approximation does not hold, but for illustrative purposes and to find the maximum, best possible performance of TCOs, the approximation will be used, neglecting the interference. It must also be noted, the phase interference could be exploited to maximize the transmittance (minimizing the reflections) over a narrow optical bandwidth, using quarter-wave transformer theory in electromagnetics.

Substituting the Drude permittivity function in into the optical quantities, the behavior will following the Drude model will hold for the optics specific constants as well. When operating above a materials plasma frequency, absorption is low and approximated to zero which allows the transmittance in (3.54) be a function of  $R$  as

$$T \approx \frac{(1 - R')^2}{1 + R'^2}, \quad (3.55)$$

where it is very easy to see as absorption and reflections are minimized, the transmission is maximized which is what is expected in any case.

The behavior of ITO shown in Fig. 3.6 displays the transmittance above the plasma frequency and the reflection, absorption below the plasma frequency which follows the analysis presented in the chapter. The plasma frequency shown as the point where the material transitions for transmitting more power than it reflects. As the operating wavelength moves beyond the plasma frequency, it begins to reflect more of the incident power.

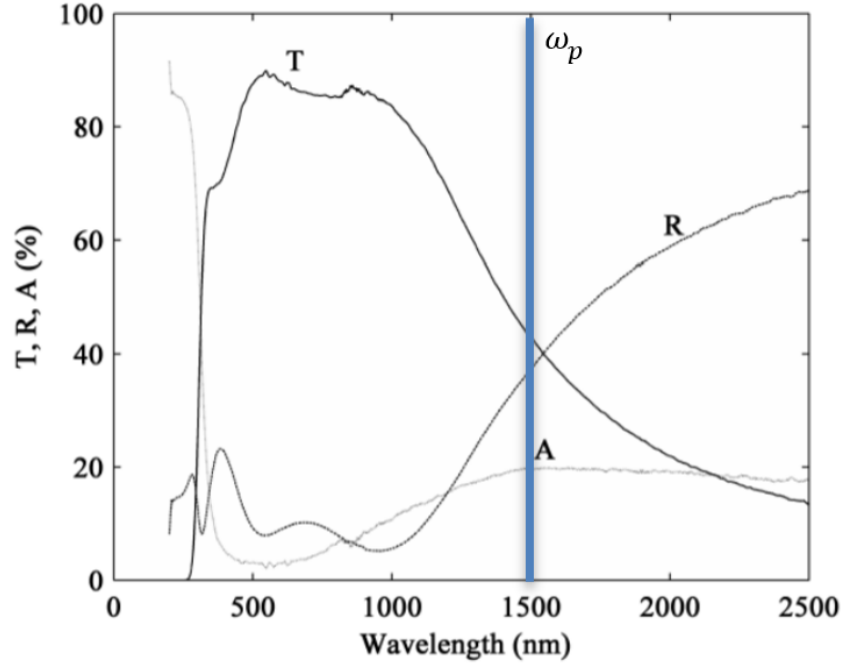


Figure 3.6: Transmittance, reflectance, and absorbance for an ITO film with plasma frequency  $\omega_p = 1500$  nm [8]

The main take away from the analysis shows a relationship between conductivity, transmittance and plasma frequency. Looking back to the previous chapter of the literature data for transparent conducting oxides, which follow the material behavior displaying a distinct plasma frequency, the materials conductivity is drastically decreased compared to typical metals with plasma frequency in the X-Ray regions of the spectrum.

One explanation to describe the phenomena of a "see-through" metal can be traced back to  $\alpha$  and  $\delta_s$  from the previous chapter skin depth  $\delta_{s(\kappa)}$  as a function of the optics quantities  $\kappa$  and  $\lambda$  as the

$$\delta_{s(\kappa)} = \frac{1}{\alpha_\kappa} = \frac{\lambda}{4\pi\kappa}, \quad (3.56)$$

Using (3.54) (neglecting  $R'$ ), it is easily shown that when  $L = 1/\alpha$ , the transmitted field drops by  $\exp\{-1\}$ , or  $\approx \frac{1}{3}$ . As stated throughout the chapter, for optical transmittance to occur the material must have a small attenuation constant and/or a small thickness to avoid the  $\alpha t$  losses. Specifically, the material thickness must be much less than the optical skin depth thereby reducing the absorption.

For conductors at RF however, the skin depth which utilizes the good conductor approximation ( $\frac{\sigma_e}{\omega\epsilon'} \gg 1$ ) and to be given as

$$\delta_s = \frac{1}{\alpha} = \sqrt{\frac{1}{\pi f \mu_0 \sigma}}, \quad (3.57)$$

where (3.56) and (3.57) are similar quantities, but not identical since the attenuation constants in optics and RF electromagnetics are different. The skin depth in RF typically is in the context of a guided transmission line (waveguide, microstrip, coplanar waveguide, etc.). The RF skin depth characterizes the conductive losses that will occur in a guided wave environment, but this skin depth is derived from the absorption properties shown in normal incidence behaviors of conductors. To avoid the absorption the conductor must be at least as thick as the skin depth. *This gives an important result for transparent conductors where it is desired that the thickness is much less than the optical penetration depth  $\delta_{s,\kappa}$  but greater than the RF skin depth  $\delta_s$ .*

Since conductors are typically known as highly reflective materials due to the attenuation constant and skin depth of conductor by the Hagen-Rubens relation which approximates the reflectance for good conductors [115]. The Hagen-Rubens relation uses the fact that for metals  $\sigma \gg \omega\epsilon'$ , which allows the approximation that  $n^2 \approx \kappa^2$  which allows reflectance from (3.48) to become

$$R = 1 - \frac{4n}{2n^2 + 2n + 1}. \quad (3.58)$$

Since for conductive materials  $n$  is large,  $2n + 1 \ll 2n^2$  at frequencies much less than the plasma frequency (or wavelengths much longer than the plasma wavelength) where *metals* refractive index  $n \gg 1$ , the expression for reflectance in metals becomes

$$R = 1 - \frac{2}{n} = 1 - 2\sqrt{\frac{\omega\epsilon_0}{\sigma}}. \quad (3.59)$$

When  $\sigma \gg \omega\epsilon$ , reflectance  $R$  given by (3.59) approaches one where all incident energy is reflected. When  $R$  is not equal to one, the rest of the power is either transmitted through or absorbed in the material. Equation (3.59) does not hold for dielectric materials, which will have reflection based on index of refraction and Snell's law.

Hecht said, "For a material to be transparent, the penetration depth must be large in comparison to its thickness." [107]. Fig. 3.7 shows that statement is valid, and a reason why many of the transparent conducting oxides do not perform well at RF/micro-/millimeter wave frequencies. Since the materials thickness is less than its skin depth, the wave penetrates through the material, with absorption. A further expansion of the general expression for the skin depth, bringing the constitutive parameters is required to gain an intuition of how the skin depth can be greater than the conductor thickness.

### 3.2 Comparing Transparent Conductors Based on Electromagnetic Properties

Optically transparent conductors are often compared in terms of optical performance and electrical performance. Though the conductors are governed by very complex material physics, the comparison process can be rather simplified. Achieving high transmittance through a conducting material typically requires the material to be made very thin to minimize absorption. Alternatively, to achieve low loss for propagating electromagnetic waves in the TCO, the material must be sufficiently thick to create a low sheet resistance. The challenge of creating a low sheet resistance is even more difficult at micro-/millimeter-wave frequencies  $f$  as the skin depth  $\delta_s$  reduces how far the wave penetrates the conductor. Figure 3.7 shows the skin depth versus varying conductivity at a few common operating frequencies. The light pink shaded region represents a common conductivity range for ITO and other transparent conducting oxides. Typical skin depths for TCOs in this range are 22-500  $\mu\text{m}$  for frequencies between 1 GHz and 77 GHz. These skin depths are much greater than the typical film thickness of 2  $\mu\text{m}$ . As a result of the thinness of the film, the ohmic losses at these frequencies are increased. Making the film thicker, however,

decreases the optical transmission. The dark gray shaded area, in contrast, shows a range of conductivities for a silver or copper mesh. For this case, all frequencies are below the  $2\text{ }\mu\text{m}$  reference line, which corresponds to their skin depths being equal to or less than the conductor thickness; no additional ohmic losses occur.

Similarly to the D.C. sheet resistance, that is dependent on conductivity and thickness, the RF sheet resistance  $R_s^{RF}$  is defined by the conductivity and the skin depth as

$$R_s^{RF} = \frac{1}{\sigma\delta_s}. \quad (3.60)$$

The RF sheet resistance is used to gather an effective resistance at a given frequency. When skin depth is not met; however, this quantity refers back to the D.C. sheet resistance using the thickness  $t$  to calculate the resistance. When RF skin depth is not met, the incident wave is effectively being transmitted through the material causing major RF losses. Typically, in electromagnetic interference (EMI) shielding applications where transparent conductors are currently used, the materials are characterized by their shielding effectiveness which a metric that describes a materials effectiveness at reflecting and/or absorbing incident fields. The result is a direct relationship to the skin depth and RF surface resistance. If the skin depth is met the RF surface resistance will be low meaning much of the wave will be reflected and shielding effectiveness is high.

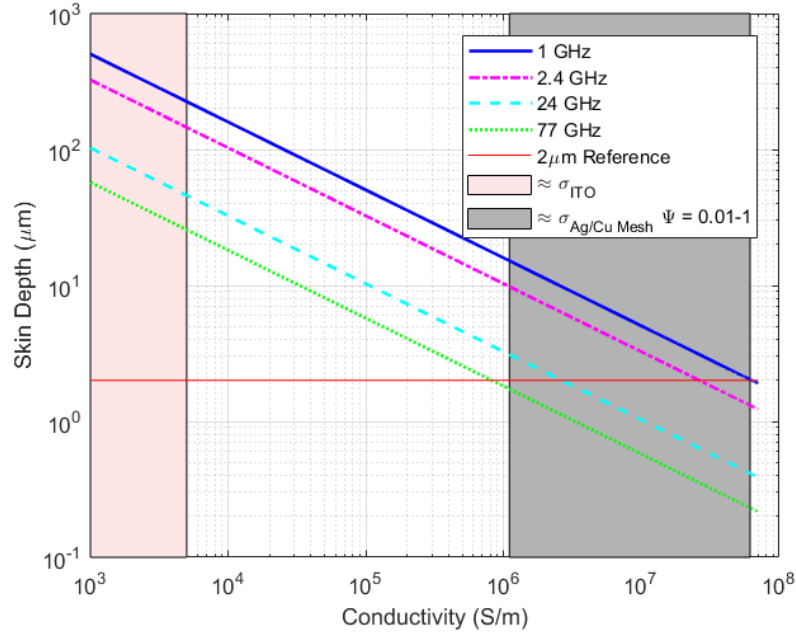


Figure 3.7: Log-log comparison of skin depth ( $\mu\text{m}$ ) versus conductivity for various RF frequencies compared to Indium Tin Oxide (ITO) and mesh conductors.

### 3.3 Comparison of Transparent Conductors

Optically transparent conductors at RF are desired to be conductive at RF and transparent in optical regions which, by the Drude model, means at RF the conductor is below the plasma frequency and in the optical region the conductor is above the plasma frequency, where the material is no longer a conductor. A summary of the behavior above and below the plasma frequency is shown in Table 3.2. A general figure of the behavior of the plasma frequency, Combining the derivations from the previous section allows the TCO materials to be analyzed for performance of conductivity and penetration depth at a desired wavelength. To avoid constraining the simulation to a certain thickness penetration depth is used. At one penetration depth the wave will have decreased by 37 % given by (3.56). Typically, the thickness of the film is chosen as a result of the optical penetration depth, since it is clear the thickness must be much less than the penetration depth to be transparent. It must be noted, using the interference effects shown above, could make it possible to engineer the transmittance of the TCO by adjusting the thickness based on quarter-wave transformer

Table 3.2: Material behavior based on the effects on parameters and constants above and below the plasma frequency where the material acts as a good insulator and good conductor, respectively.

	$\omega < \omega_P$	$\omega > \omega_P$
Effective Conductivity $\sigma_e$	$\approx \sigma$	$\approx 0$
Complex Permittivity $\tilde{\epsilon}$	$\approx j\frac{\sigma}{\omega}$	$\approx \epsilon'$
Complex Refractive Index $\tilde{n}$	$\approx j\kappa \approx j\sqrt{\left(\frac{\sigma}{\omega\epsilon_0}\right)}$	$\approx n \approx \sqrt{\frac{\epsilon'}{\epsilon_0}}$
Attenuation Constant $\alpha$	$\approx \sqrt{\frac{\omega\mu_0\sigma}{2}}$	$\approx 0$
Reflectance $R$	$\approx 1 - 2\sqrt{\frac{\omega\epsilon_0}{\sigma}}$	$\approx \frac{(\sqrt{\epsilon'/\epsilon_0}-1)^2}{(\sqrt{\epsilon'/\epsilon_0}+1)^2}$
Transmittance $T$	$\approx \frac{(1-R)^2}{1+R^2} \approx 0$	$\approx 1 - \frac{(\sqrt{\epsilon'/\epsilon_0}-1)^2}{(\sqrt{\epsilon'/\epsilon_0}+1)^2}$
EM Behavior	Good Conductor	Transparent

and the  $\lambda/4$  behavior in electromagnetic waves which could be a trade-off between the thickness and absorption to increase transmittance.

Examining the effects of plasma frequency at a fixed optical frequency (or wavelength) is shown in Fig. 3.8. It is very important to notice the x-axis in Fig. 3.8, is plasma wavelength, not wavelength. The figure uses the Drude model for permittivity (3.30), conductivity from (3.25) to analyze the behavior of a material's optical penetration depth and DC conductivity (shown in log scale in Fig. 3.8) when shifting the plasma frequency. As *plasma wavelength is increased above the optical operating wavelength the penetration depth increases; thus transmittance increases but the DC conductivity rapidly decreases.*

### 3.3.1 Limitations of Transparent Conducting Oxides

For the analysis in this paper, the behavior of materials at the plasma frequency is not as important as to where the frequency occurs. Background knowledge of the plasma frequency is important for clear explanation of how an optically transparent conductor can be physically possible. At frequencies below the plasma frequency, the imaginary part of the permittivity dominates the complex permittivity; thus the material is conductive, or in more physical terms, an incident wave is reflected. In contrast, when the frequency of the incident electromagnetic field is above the plasma frequency, the permittivity will have a

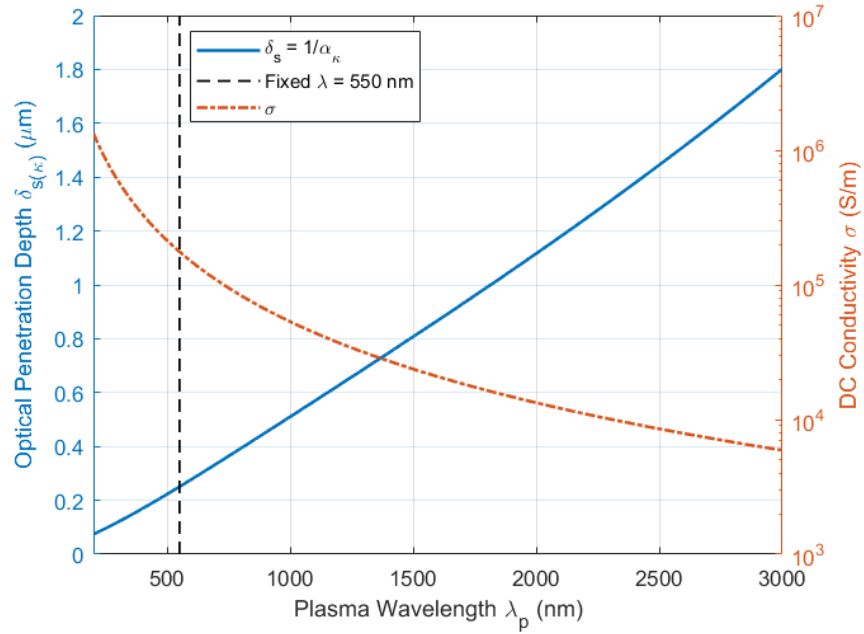


Figure 3.8: Optical penetration depth and conductivity versus plasma frequency given an operating wavelength in the visible region of 550 nm and DC conductivity versus plasma frequency. The graph is fixing the operating frequency and varying the plasma frequency to display the effects of operating above and below the plasma frequency.

positive real part and the conductivity in the imaginary part of permittivity loses its strength allowing the incident waves to be transmitted and/or absorbed in the material. As a result, the plasma frequency for optically transparent conductors must be above the visible range frequencies to see through with the human eye. In conclusion, the plasma frequency allows materials to be conductive and reflect incident electromagnetic fields in a lower frequency, but at a higher frequency above the plasma frequency, the incident wave will be absorbed and/or transmitted through the material. Furthermore, by the Drude model, as the plasma frequency decreases, so does the DC and RF conductivity (see Table 3.1) which brings the fundamental limitation of transparent conductors for RF applications which require high conductivity in order to reach skin depth requirement to minimize resistive losses. As a result, the mesh conductor is commonly used in RF applications, as seen in the previous chapter. The mesh conductor, LikeTCOs, has its own pros, cons, and trade-offs but has a large advantage over TCOs.



### 3.3.2 Advantages of Optically Transparent Mesh Conductor

Knowledge of the limitations of the transparent conducting oxides allows the exploitation of a different class of transparent material. As mentioned in the previous chapter, mesh conductors have been used as an alternative transparent conductor for different applications, typically in EMI shielding where it has shown effective shielding up to 60 dB at 2 GHz [116]. The mesh is ultimately an inductive high-pass filter which blocks RF and passes optical frequencies shown in Fig. 3.9. The mesh uses the openings in the conductor to reject or pass signals based on the pitch of the mesh allows tuning of the frequency response. At higher frequencies/smaller wavelengths, more electromagnetic leakage will occur. Unlike with TCO's, the geometry can be altered to combat the electromagnetic leakage by creating a better conducting surface at each frequency. As mentioned before, with advancements in micro-manufacturing, the mesh screens can be made invisible to the naked eye.

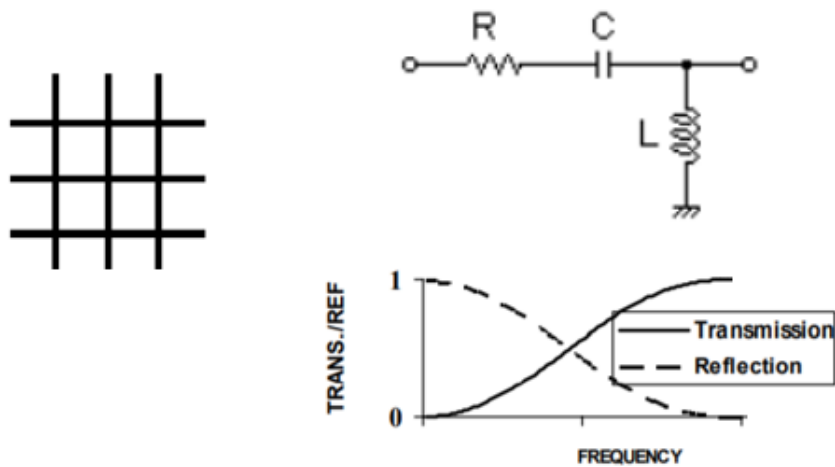


Figure 3.9: Mesh topology described by an RLC high pass filter [117].

To provide parallels to the TCOs and plasma frequency, the mesh has its own filter cutoff frequency, very Like the plasma frequency at a high level. At the physical level, the

behavior is very different. The difference is that the mesh is still conductive at the optical frequencies, but due to the geometry where the spacing determines when an incident wave can pass. The mesh is conductive at RF with its effective conductivity being the ratio of material that is present, whereas the transmittance is directly the opposite. Using the fill factor  $\Psi$  introduced in the previous chapter allows the mesh to be treated with simple geometric expressions, whereas the TCOs require complex material physics to describe the operation. The transmittance  $T_{mesh}$  and conductivity  $\sigma_{mesh}$  can be simply shown as

$$T_{mesh} = (1 - \Psi)^2, \quad (3.61)$$

and the conductivity as

$$\sigma_{mesh} = \sigma(2\Psi - \Psi^2), \quad (3.62)$$

where the ratio of  $\sigma_{mesh}$  to  $\sigma$  comes from the fact that

$$1 - (1 - \Psi)^2 = 2\Psi - \Psi^2. \quad (3.63)$$

In addition to the higher performance available when using a metal mesh, the geometry of the mesh makes analysis much simpler than the TCO materials. Using the geometry of the mesh, the conductivity and transmittance can be easily predicted based on the fill factor as shown in Fig. 3.10.

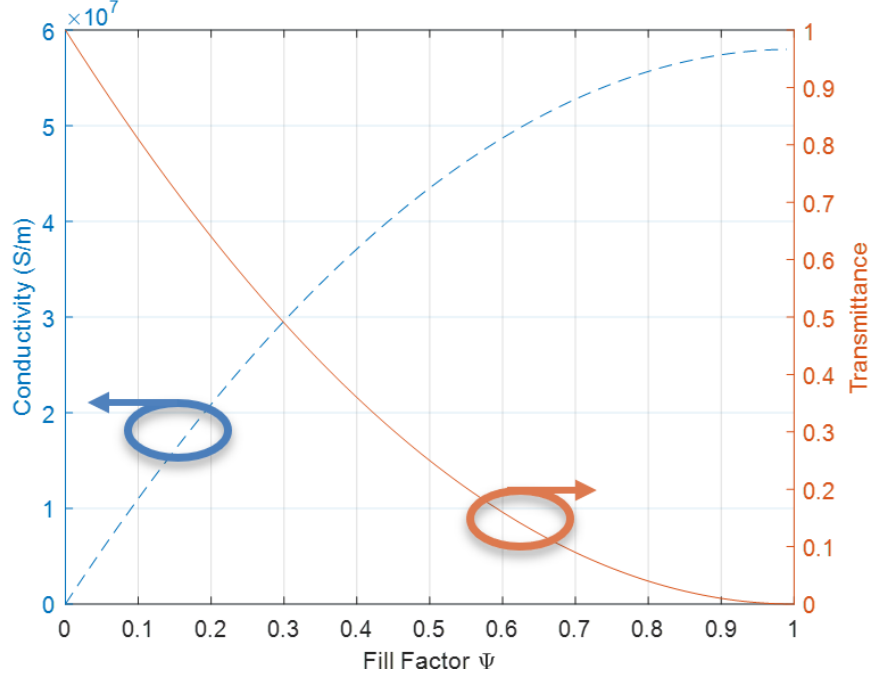


Figure 3.10: Optical transmittance and conductivity versus fill factor.

### 3.4 Proposed Figure of Merit for RF/EO Transparent Conductors

With an understanding of how both TCO and mesh type conductors over the electromagnetic spectrum, a figure of merit based on optical transmittance and RF sheet resistance can be introduced to allow the co-design for maximum RF and EO/IR performance. As it was shown, there are pros and cons to both types of conductors, and some are better suited for certain applications. For an optically transparent conductor to be operable RF, the figure of merit will be helpful in providing a relationship to the behavior of a material at a specified optical wavelength and RF frequency to a single quantity. The following presents figure of merit as a function of transmittance and RF sheet resistance if the RF skin depth is less than the thickness of the conductor shown as

$$\phi_{new}(\lambda_{EO}, f_{RF}) = \frac{T_{\lambda}^{10}}{R_s^{RF}} = T_{\lambda}^{10} \sigma t_{eff}; \quad (3.64)$$

where  $t_{eff}$  is the effective thickness given by

$$t_{eff} = \min(\delta_s, t), \quad (3.65)$$

where  $f_{RF}$  is the RF operating frequency to calculate  $R_s^{RF}$ , and  $T_\lambda$  is the transmittance at the desired optical wavelength  $\lambda_{EO}$ . The effective thickness is necessary since many transparent conducting oxides do not reach skin depth as shown before. The effective thickness allows the RF sheet resistance to be weighted by the thickness or skin depth, whichever is smaller. Since at RF, the skin depth the thickness that the RF electromagnetic wave interacts with, and anything greater is not accounted for in the materials RF sheet resistance. This thickness allows the correct weighting of the figure of merit materials greater than the skin depth and also those with a thickness that does not reach skin depth, which Haacke's figure of merit for transparent conductors did not account for.

For TCOs, the figure of merit can be expanded into the material parameters derived earlier in the chapter using the Drude model analysis. Using the Drude model approximations where at  $\lambda_{EO}$  the material will be operating above the plasma frequency, and at  $f_{RF}$  the material will have behavior below the plasma frequency which will greatly simplify the expression. The new figure of merit will consider both RF/EO operating frequencies since as we now know the material parameters change over both regions. Doing so will allow the figure of merit to be optimized in terms of the fundamental material parameters. In addition, the figure of merit requires the RF skin depth to be calculated, doing so will allow a verification that the conductor thickness is reaching the requirements to avoid conductive losses

#### 3.4.1 Figure of Merit Specific to Transparent Conducting Oxides

Using the Drude approximations going back to Table 3.2, the figure of merit for TCO's  $\phi_{new}^{TCO}$  can now be given in various forms based on the model of transmittance that is used.

The most general case will assume single bounce reflection on both boundaries with absorption given as,

$$\phi_{new}^{TCO} = \frac{T_{\lambda}^{10}}{R_s^{RF}} = \left( \frac{(1 - R_{\lambda})^2 \exp(-\alpha_{\kappa} t)}{1 + R_{\lambda}^2 \exp(-2\alpha_{\kappa} t)} \right)^{10} \sigma t_{eff}, \quad (3.66)$$

where  $t$  is the TCO thickness. For simplicity and illustrative purposes, the figure of merit will be shown assuming a reflectionless TCO, where the only transmissive losses come from the absorption. Using the approximation that  $R_{\lambda} = 0$ , the equation becomes

$$\phi_{new}^{TCO} = \frac{T_{\lambda}^{10}}{R_s^{RF}} = (\exp(-\alpha_{\kappa} t))^{10} \sigma t_{eff}, \quad (3.67)$$

which gives the conclusion that to maximize the figure of merit, it is desired that  $\alpha_{\kappa} t$  is minimized while  $\sigma t_{eff}$  is maximized. In physical terms this means to minimize the optical attenuation or the thickness while maximizing the conductivity and effective thickness (minimum between thickness and skin depth). From the analysis shown, the skin depth at RF is unlikely to be met for a TCO, thus the thickness of the conductor will be used rather than the skin depth. This results in a situation where the figure of merit is not being maximized.

Assuming the conductor thickness at RF can reach skin depth the figure of merit can be given its full form is represented as

$$\phi_{new}^{TCO} = \left( \exp \left[ -\frac{4\pi}{\lambda} \left\{ \frac{1}{2} \left( \sqrt{\left( \frac{\epsilon'_D}{\epsilon_0} \right)^2 + \left( \frac{\epsilon''_D}{\omega \epsilon_0} \right)^2} - \frac{\epsilon'_D}{\epsilon_0} \right) \right\}^{1/2} t \right] \right)^{10} \sigma \sqrt{\frac{1}{\pi f \tilde{\mu}_0 \sigma}}, \quad (3.68)$$

which relating the material parameters back to the Drude model conductivity and complex

permittivity are both a function of the plasma frequency where

$$\epsilon'_D = \epsilon' \left( 1 + \frac{\omega_p^2 \tau^2}{1 + \omega^2 \tau^2} \right), \quad (3.69)$$

$$\epsilon''_D = \epsilon' \left( \frac{\omega_p^2 \tau / \omega}{1 + \omega^2 \tau^2} \right), \quad (3.70)$$

and

$$\sigma = \omega_p^2 \epsilon' \tau, \quad (3.71)$$

The new figure of merit for TCO's with fixed operating wavelength  $\lambda = 550$  nm for a changing plasma wavelength is shown in Fig. 3.11. Since the conductor thickness for TCOs must remain small to maintain high transmittance, the results are a low figure of merit since the skin depth likely isn't met, which was shown is due to a simultaneously decreased conductivity from decreasing the plasma frequency which ultimately allows optical transmittance. Since skin depth is not met to maintain high transmittance, the figure of merit varies less with frequency.

Additionally, using literature data that provided thickness, transmittance, sheet resistance (or conductivity) the figure of merit can be compared for validity in realistic materials shown in Fig. 3.12. Since the TCO materials are process dependent and vary widely, the Drude model cannot predict the values of transmittance and sheet resistance precisely, but the figure shows the Drude model is in the correct range of simultaneous conductivity and transmittance for the TCO type materials. The figure uses Drude model plasma wavelengths of  $\lambda = 1000nm$  and  $\lambda = 1500nm$  since these values are typical of ITO and AZO films.

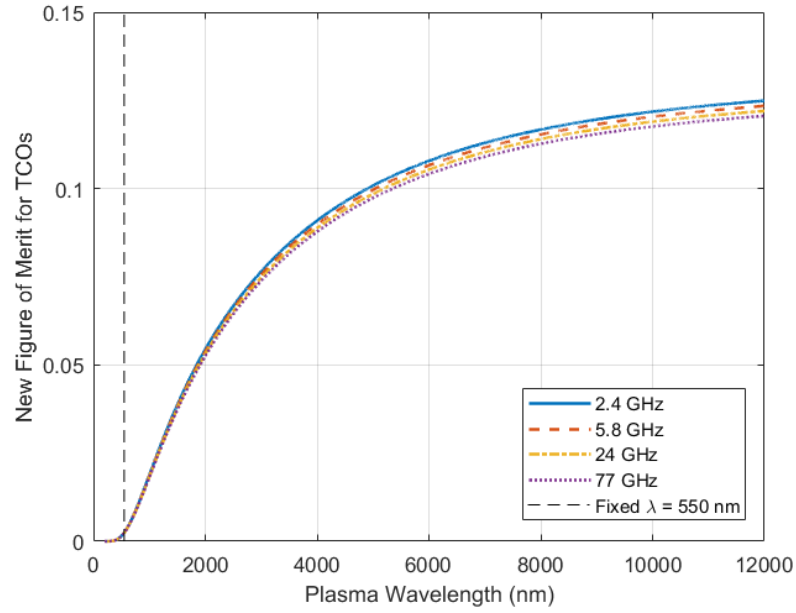


Figure 3.11: Figure of merit for a TCO versus plasma wavelength for optical operating wavelength of 550 nm (visible) for different ISM Band frequencies with a material thickness of 100 nm to achieve transmittance and the RF surface resistance when skin depth is not met.

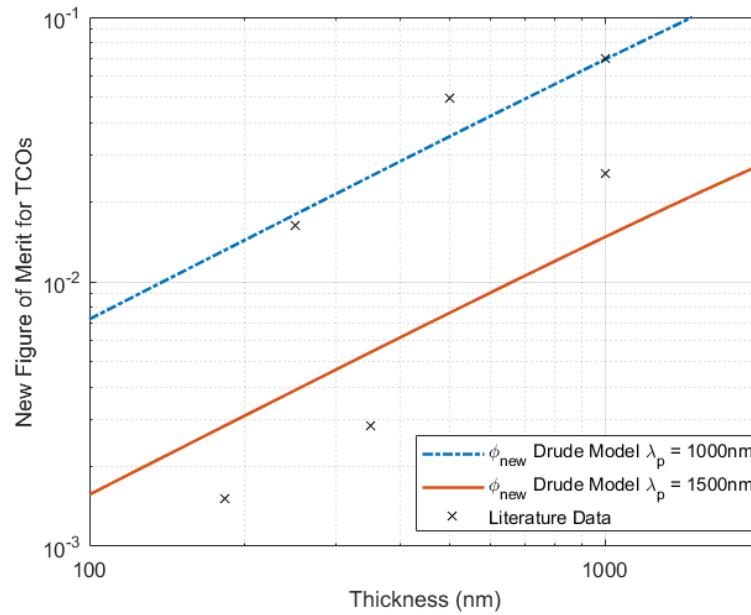


Figure 3.12: Figure of merit for a TCO versus changing thickness at operating wavelength  $\lambda = 550\text{nm}$  and Drude model plasma wavelengths of  $\lambda = 1000\text{nm}$  and  $\lambda = 1500\text{nm}$  with literature data plotted for comparison.

### 3.4.2 Figure of Merit Specific to Mesh Conductors

For the mesh, as alluded to before, the figure of merit is much simpler and can be discussed by pure geometry, rather than complex material parameters that change over the spectrum. The mesh is much simpler since it is only a function of the fill factor  $\Psi$ , the conductivity  $\sigma$ , and RF frequency  $f_{RF}$ . The mesh figure of merit for RF conductors becomes

$$\phi_{new}^{mesh} = (1 - \Psi)^{20} \sigma (2\Psi - \Psi^2) \delta_s, \quad (3.72)$$

which can be visualized in Fig. 3.13. Figure 3.13 shows that for low fill factor, the figure of merit is orders of magnitudes greater than the mesh figure of merit. This is largely due to the fact that the skin depth can be reached for the mesh conductor, whereas for the TCO they do not. If a TCO could reach skin depth with a thicker film thickness while achieving similar transmittance, the figure of merit would be greater, but for now with the real theoretical limitations of TCOs, *the mesh is the better option as an RF transparent conductor*.

Analyzing Fig. 3.13 further will give insights on how to design the mesh for RF circuits. In Fig. 3.13, there is a peak between  $\Psi = 0.05$  and  $0.1$ . This peak corresponds fill factor of the maximum figure of merit of a 1 micron thick copper conductor. This peak occurs given the trade-offs between the fill factor, frequency, and material thickness which is much simpler to characterize than the TCO since the mesh response is purely based on geometry. Since the mesh transmittance is based purely on geometry, the normally incident transmittance does not depend on conductor thickness, so the conductor thickness deposited is greater to reach the skin depth requirement.



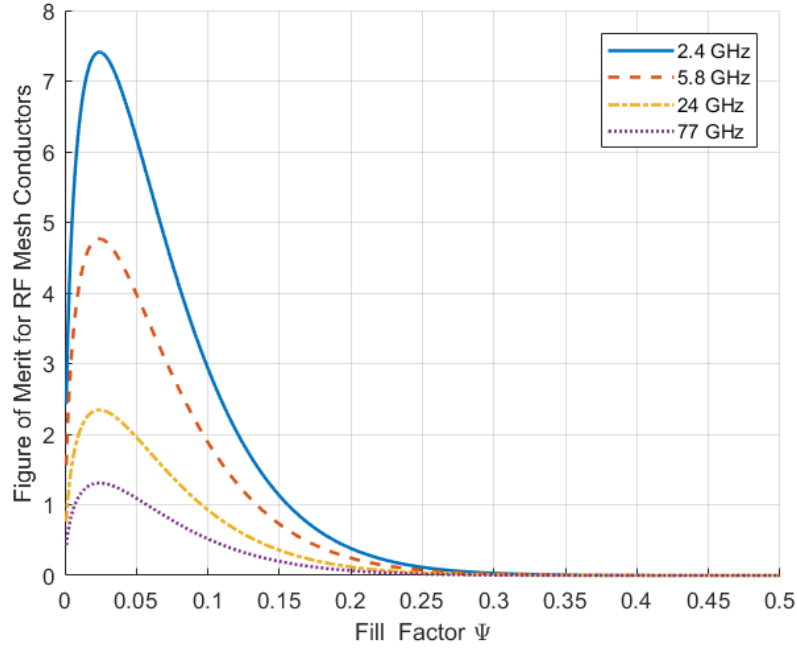


Figure 3.13: Modified new figure of merit for a  $1 \mu\text{m}$  thick copper mesh conductor ( $\sigma = 5.8e7 \text{ S/m}$ ) versus fill factor for the ISM band frequencies using the figure of merit in (3.72).

### 3.4.3 Literature Data Comparison Based on New Figure of Merit

Using the literature data with conductor thicknesses in Table 3.3, only a subset of the sources that gave values of conductor thickness, optical transmittance, sheet resistance. The data from these sources were analyzed further and compared at different operating frequencies in Figs. 3.14, 3.15, 3.16, and 3.17. The figures are all plotted with a maximum limit for both the mesh and TCO at each frequency from the maximum values shown in Figs. 3.11 and 3.13 based on the previous analysis of the TCO and mesh conductors. Using the skin depth/thickness conditional allows the conductors to be accurately compared for performance at different RF/millimeter-wave frequencies which was not possible using the previous figure of merit. The new figure of merit will vary depending on RF operating frequency  $f_{RF}$  since the skin depth changes versus frequency (refer to Fig. 3.7). At low frequencies, the figure of merit shows clearly that the mesh has higher performance. As frequency increases, the skin depth decreases, causing the effective thickness to decrease.

This can be seen where the figure of merit continues to decrease for the mesh conductors as frequency increases. The TCO conductors' figure of merit looks to remain the same at all frequencies since, due to the low conductivity and very small thicknesses, the skin depth requirement is not met.

*As a result of the analysis presented in this chapter, the best performing and most practical transparent conductor for RF and millimeter-wave applications is the mesh conductor which outperforms a transparent conducting oxide in all cases. Overall, the mesh shows higher conductivity in the RF region while displaying high transmittance in the optical or infrared regions based on the geometry. As a result, the next two chapters will discuss the design implications of introducing a mesh conductor into an RF circuit and the imaging performance over an optical aperture. A summary of the important equations and derivations from the chapter is shown in Table 3.4.*

Table 3.3: Published data from Table 2.1 that provided thickness, transmittance, and sheet resistance to be used for analysis on the new figure of merit for transparent RF conductors

Conductor	Thickness	$T_{max}$	$R_s$ ( $\Omega/sq$ )	$\phi_{TC} = T^{10}/R_s$	$\Psi$ (mesh only)	Source
AZO	500 nm	0.9	7.1	0.04911	-NA-	[20]
AZO	1000 nm	0.9	5	0.06974	-NA-	[21]
AZO	220 nm	0.965	6.2	0.11295	-NA-	[22]
ITO	250 nm	0.85	12	0.01641	-NA-	[33]
ITO	350 nm	0.731	15	0.00290	-NA-	[33]
ITO/AlSiO <sub>2</sub>	650 nm	0.85	6	0.03281	-NA-	[35]
ITO/Cu/ITO	183 nm	0.61	4.7	0.00152	-NA-	[34]
Copper Mesh	2500 nm	0.87	0.36	0.69007	0.0625	[10]
Copper Mesh	2500 nm	0.81	0.22	0.37890	0.091	[10]
Copper Mesh	2500 nm	0.78	0.22	0.38790	0.090	[10]
Copper Mesh	2500 nm	0.8	0.18	0.59652	0.048	[10]
Copper Mesh	2500 nm	0.86	0.15	1.47534	0.048	[10]
Copper Mesh	2500 nm	0.83	0.115	1.34922	0.0625	[10]
Copper Mesh	2500 nm	0.82	0.11	1.24953	0.063	[10]
Copper Mesh	2500 nm	0.78	0.14	0.59541	0.595	[10]
Copper Mesh	2500 nm	0.77	0.09	0.81408	0.091	[10]
Copper Mesh	2500 nm	0.71	0.09	0.36169	0.091	[10]

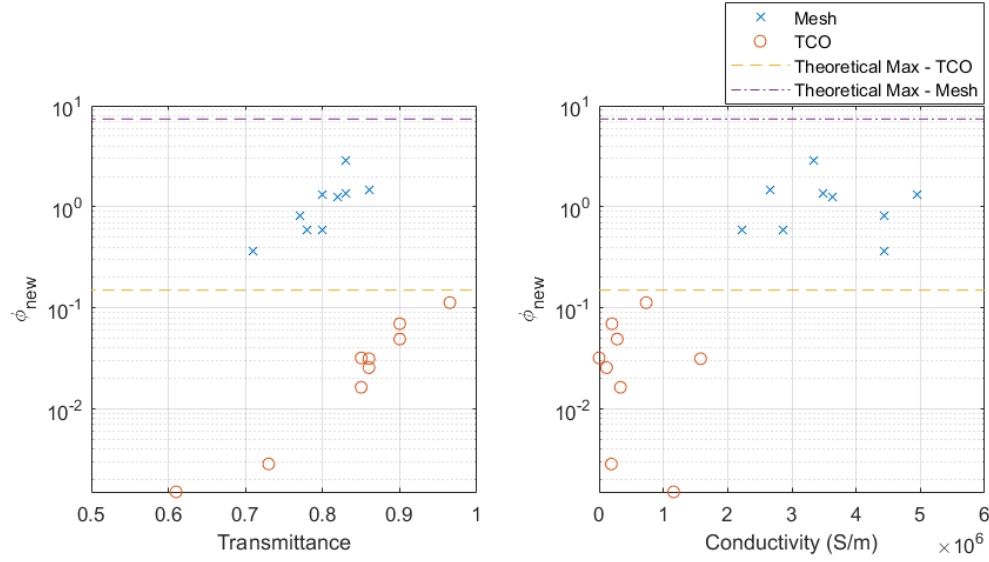


Figure 3.14: Modified figure of merit for transparent conductors using skin depth calculated at frequency  $f_{RF}=2.45$  GHz. (Left) Figure of merit versus reported visible transmittance (Right) Figure of merit versus reported conductivity.

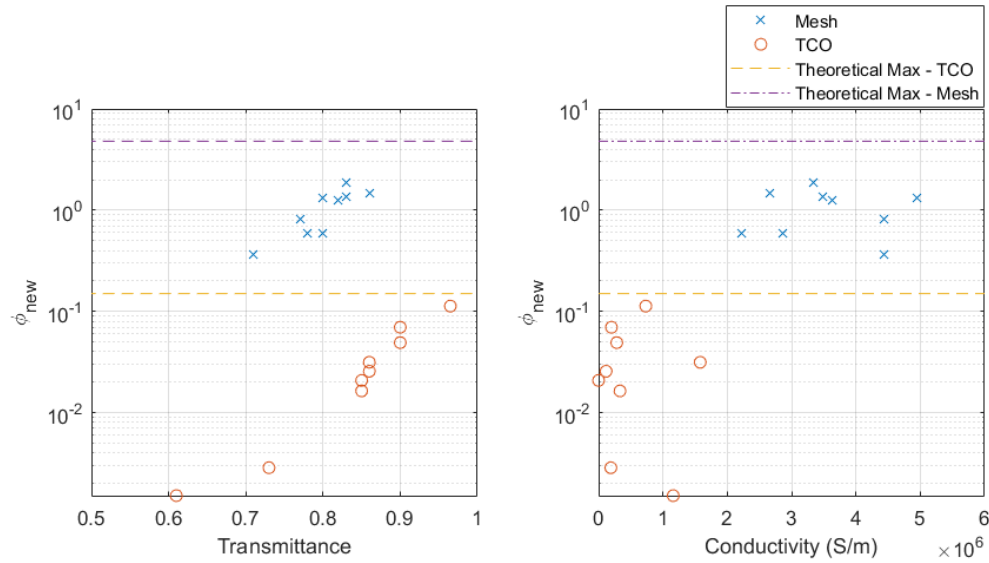


Figure 3.15: Modified figure of merit for transparent conductors using skin depth calculated at frequency  $f_{RF}=5.8$  GHz. (Left) Figure of merit versus reported visible transmittance (Right) Figure of merit versus reported conductivity.

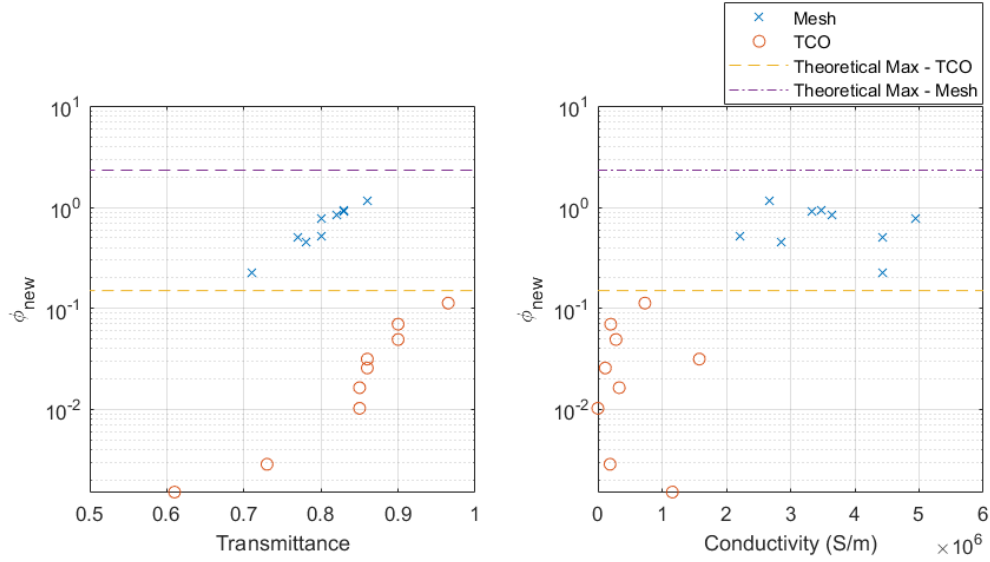


Figure 3.16: Modified figure of merit for transparent conductors using skin depth calculated at frequency  $f_{RF}=24$  GHz. (Left) Figure of merit versus reported visible transmittance (Right) Figure of merit versus reported conductivity.

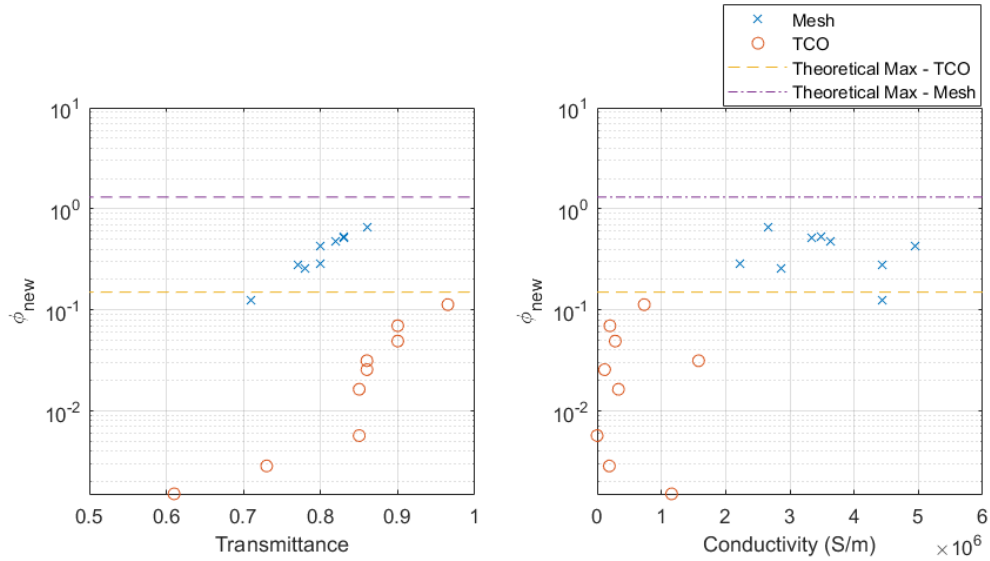


Figure 3.17: Modified figure of merit for transparent conductors using skin depth calculated at frequency  $f_{RF}=77$  GHz. (Left) Figure of merit versus reported visible transmittance (Right) Figure of merit versus reported conductivity.

Table 3.4: Summarized list of the important equations from the chapter

Description	Equation	#
Effective conductivity	$\sigma_e = \omega\epsilon'' + \sigma$	(3.10)
Complex Permittivity	$\tilde{\epsilon} = \epsilon' - j\frac{\sigma_e}{\omega}$	(3.12)
Plasma Frequency	$\omega_p = \sqrt{\frac{q^2 N}{\epsilon' m \tau}} = \sqrt{\frac{\sigma}{\epsilon' \tau}}$	(3.25)
Drude Complex Permittivity	$\tilde{\epsilon}_D = \epsilon' \left(1 - \frac{\omega_p^2}{\omega^2 + j\omega\tau^{-1}}\right)$	(3.30)
Drude DC Condcutivity	$\sigma = \omega_p^2 \tau \epsilon'$	(3.32)
Drude Effective Conductivity	$\sigma_e \approx \frac{\omega_p^2 \tau}{\omega^2 \tau^2 + 1} \epsilon'$	(3.31)
Complex Refractive Index	$\tilde{n} = n - j\kappa = \sqrt{\frac{\tilde{\epsilon} \tilde{\mu}}{\epsilon_0 \mu_0}}$	(3.37)
Refractive Index	$n = \left[ \frac{1}{2} \left( \sqrt{\left(\frac{\epsilon'}{\epsilon_0}\right)^2 + \left(\frac{\sigma_e}{\omega\epsilon_0}\right)^2} + \frac{\epsilon'}{\epsilon_0} \right) \right]^{1/2}$	(3.42)
Extinction Coefficient	$\kappa = \left[ \frac{1}{2} \left( \sqrt{\left(\frac{\epsilon'}{\epsilon_0}\right)^2 + \left(\frac{\sigma_e}{\omega\epsilon_0}\right)^2} - \frac{\epsilon'}{\epsilon_0} \right) \right]^{1/2}$	(3.43)
Reflectance	$R' = \frac{\sqrt{\left(\frac{\epsilon'}{\epsilon_0}\right)^2 + \left(\frac{\sigma_e}{\omega\epsilon_0}\right)^2} + 1 - \sqrt{2 \left( \sqrt{\left(\frac{\epsilon'}{\epsilon_0}\right)^2 + \left(\frac{\sigma_e}{\omega\epsilon_0}\right)^2} + \left(\frac{\epsilon'}{\epsilon_0}\right) \right)}}{\sqrt{\left(\frac{\epsilon'}{\epsilon_0}\right)^2 + \left(\frac{\sigma_e}{\omega\epsilon_0}\right)^2} + 1 + \sqrt{2 \left( \sqrt{\left(\frac{\epsilon'}{\epsilon_0}\right)^2 + \left(\frac{\sigma_e}{\omega\epsilon_0}\right)^2} + \left(\frac{\epsilon'}{\epsilon_0}\right) \right)}}$	(3.49)
Transmittance	$T = \frac{I_t}{I_0} = \frac{(1-R')^2 \exp(-\alpha_\kappa L)}{1+R'^2 \exp(-2\alpha_\kappa L)}$	(3.54)
Attenuation Constant	$\alpha = \text{Re}\{\gamma\} = \omega \sqrt{\tilde{\mu} \epsilon'} \left( \frac{1}{2} \left( \sqrt{1 + \left(\frac{\sigma_e}{\omega\epsilon'}\right)^2} - 1 \right) \right)^{1/2}$	(3.17)
Absorption Coefficient	$\alpha_\kappa = \frac{4\pi\kappa}{\lambda} = \frac{4\pi}{\lambda} \left( \frac{1}{2} \left( \sqrt{\left(\frac{\epsilon'}{\epsilon_0}\right)^2 + \left(\frac{\sigma_e}{\omega\epsilon_0}\right)^2} - \frac{\epsilon'}{\epsilon_0} \right) \right)^{1/2} \equiv 2\alpha$	(3.45)

## CHAPTER 4

### OPTICAL CHARACTERIZATION OF TRANSPARENT CONDUCTORS

---

**Chapter Overview:** This chapter provides the following:

- Measured transmittance comparison of ITO and mesh
  - Imaging experiment to investigate the degradation of an imaging systems modulation transfer function with the introduction of a TCO or mesh conductor over the optical aperture.
- 

The transparent conducting oxide and mesh will be further compared with laboratory measurements, including transmittance versus optical wavelength and imaging tests. For single aperture sensing, the effects on transmittance over range of wavelengths and effects on imaging when introducing a transparent conductor over the optical aperture needs to be further investigated for a complete characterization. The following section provides novel imaging experiments investigating the optics of optically transparent conductors which has not been considered for applications in literature.

The mesh conductor measured was made in a collaboration with Binghamton University Center for Advanced Microelectronics Manufacturing (CAMM) shown in Fig. 4.1. The mesh was fabricated 1  $\mu\text{m}$  thick copper mesh pitch  $g' = 95 \mu\text{m}$  and line width  $w' = 5 \mu\text{m}$  for a fill factor  $\Psi = 0.05$  which corresponds to a theoretical transmittance of 90% using the equation for fill factor and mesh transmittance from the previous chapter (2.4) and (2.6), respectively.

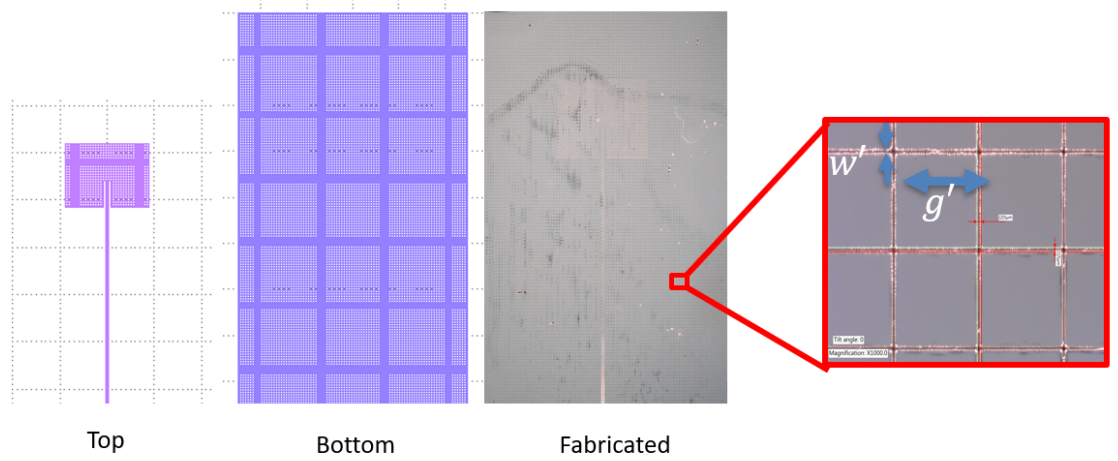


Figure 4.1: Transparent mesh antenna (left) K-layout model and (right) fabricated photos from Binghamton University CAMM. Mesh parameters are  $1\text{ }\mu\text{m}$  thick copper mesh, pitch  $g' = 95\text{ }\mu\text{m}$ , and line width  $w' = 5\text{ }\mu\text{m}$  for a calculated fill factor  $\Psi = 0.05$ .

#### 4.1 Measured Transmittance Comparison of Transparent Conductors

The transmittance versus wavelength of transparent conductors is of interest for many broadband optical applications. Thus far, many of the transparent conductors used on antennas have focused on purely visible wavelengths. For multi-modal sensing, studying wavelengths beyond the visible range is of interest to characterize the mesh and ITO materials and compare them. Transmittance measurements comparing the mesh and ITO over a wide range of optical wavelengths will be performed. Many imaging systems perform beyond the visible range, for example automotive night vision operates in the short wave infrared (SWIR) wavelengths. Studies in literature comparing the mesh to ITO for antenna purposes typically compare the transmittance at visible wavelengths since, thus far, many applications only require visible transparency.

Using the Cary 5000 Spectrometer, samples of ITO on PET and a mesh on Willow glass are measured to directly compare the two separate conductors optical performance. The measurement range was from 200 nm to 3200 nm (UV to SWIR). The measurement set-up is shown in Fig. 4.2.

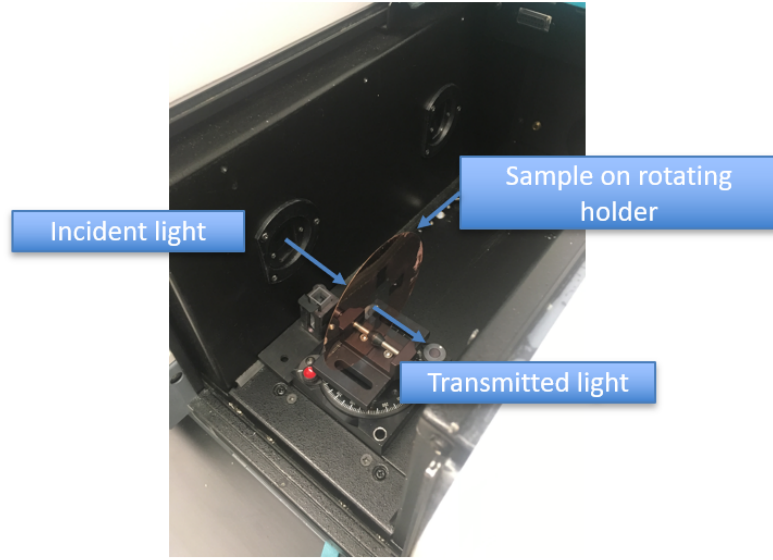


Figure 4.2: Sample optical transmittance measurement set-up in the Cary 5000 Spectrometer annotated for optical characterization from 200 nm to 3200 nm.

The samples measured are a mesh on Corning Willow glass sample shown in Fig. 4.1, where the PET ITO is a commercially available ITO film sample from Optical Filters USA used for EMI shielding applications [116]. The baseline measurements of a blank Willow glass and blank PET film for the mesh and ITO respectively will be taken to analyze the behavior of only the effects of the transparent conductor, and not the substrate. The measured data is shown in Fig. 4.3. Comparing the mesh versus a commercially available ITO sample over the broad optical bandwidth the differences are evident. The data shows the mesh is constant at the predicted 90% based on the fill factor  $\Psi = 0.05$  whereas the ITO had very high transmittance over the visible region but dropped off in the infrared going to 50% at 1700 nm which shows agreement to the analysis shown in the previous chapter and what is presented in the literature [8].

Using a baseline for each measurement allows the extraction to examine the effects of the conductor only without the substrate, which can be extracted by simple division as

$$T_{cond}(\%) = \frac{T_{cond+sub}}{T_{sub}} \times 100\% \quad (4.1)$$



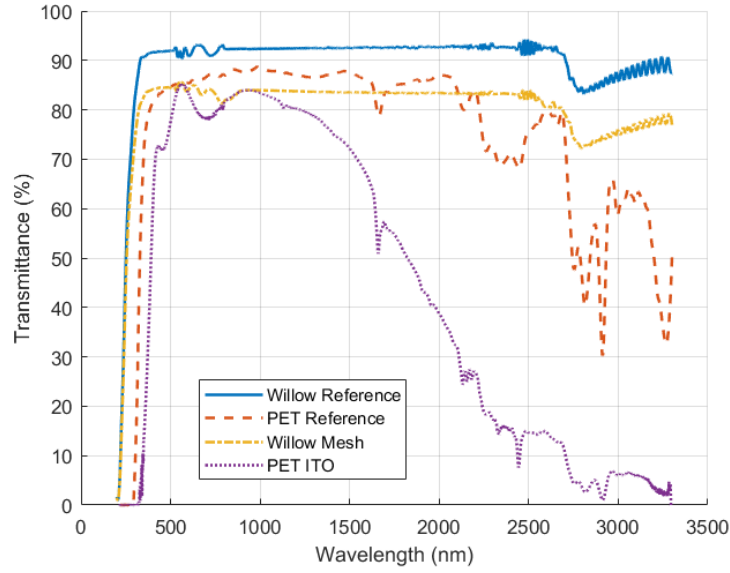


Figure 4.3: Normal transmittance of ITO, mesh and the baselines (PET, Willow glass)

where  $T_{cond+sub}$  is the conductor and substrate and  $T_{sub}$  is the baseline blank substrate which, for ITO is PET, and the mesh is the Corning Willow glass.

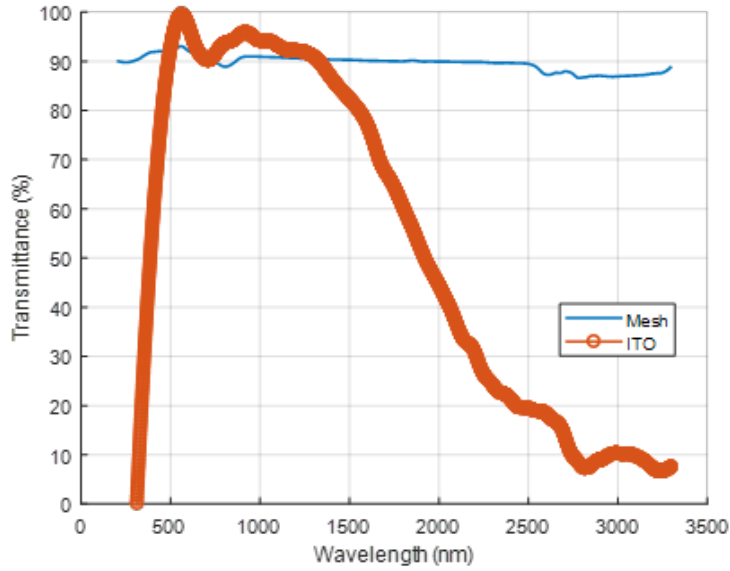


Figure 4.4: Normalized transmittance comparison of ITO and mesh conductors.

Using (4.1) on the data in Fig. 4.3, the effects of only the conductors on the respective material can be seen in Fig. 4.4. As predicted, the mesh with fill factor  $\Psi = 0.05$  has a

transmittance of approximately 90%, nearly constant over the entire measured spectrum. Also, the ITO film has transmittance in the visible region but a strong drop in transmittance around 1500 nm, and evidence of the plasma effects allowing the high frequencies to pass while the lower frequencies absorb/reflect the incident electromagnetic waves. Further analysis was carried out by measuring the materials at angles of incidence from 0 to 40 degrees to see the effects angle has on transmittance and shown in Fig. 4.8. For optical imaging systems, characterizing materials at angles of incidence will allow a limit on their maximum acceptance cone angle (field of view). Since the measured mesh has two sides of metallization, the transmittance is limited by the geometrical size, thickness, and alignment of these mesh lines. When the angle is normal to the mesh, the effects of thickness is negligible. The only properties affecting transmittance are the geometry of the mesh and the alignment. Shown by Fig. 4.5 as the angle is increased, the effective fill factor that allows light to pass through the mesh is decreased. This result is shown in Fig. 4.8 where the mesh transmittance decreases as the angle increases. Including conductor thickness and

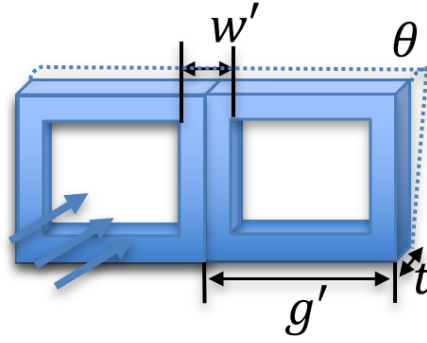


Figure 4.5: Mesh parameters with added angle of incidence

angle, fill factor becomes

$$\Psi = \frac{w'}{g' + w'} \Rightarrow \frac{t \sin \theta + w' \cos \theta}{g' \cos \theta + w' \cos \theta}. \quad (4.2)$$

In addition, this will occur at two layers, separated by the glass thickness. The second layer will block the light with a relationship between the conductor thickness, the angle of

incidence, and the thickness of the substrate ( $100 \mu\text{m}$  thick glass). Fig. 4.8 shows the mesh decrease from 90% at normal incidence to 80% at  $40^\circ$ . Mathematically, the two-layer mesh can be expressed as

$$\Psi = \frac{w'}{g' + w'} \Rightarrow \frac{t \sin \theta + w' \cos \theta + t_e}{g' \cos \theta + w' \cos \theta}. \quad (4.3)$$

where  $t_e$  is the effective thickness of the line width given by

$$t_e = \min(w', t_{sub} \tan(\theta)) \quad (4.4)$$

where the added  $(t_e \tan \theta)$  part in the numerator is expressed the minimum between the  $t_{sub}$  and line width since as the angle increases the line width from the second layer will be in the field of view to the incident light shown in Fig. 4.6. The linear behavior from  $0^\circ$  to  $5^\circ$  is from the  $(t_e \tan \theta)$  part of the equation, where  $t_{sub} \tan \theta$  is less than  $w'$ . When  $w'$  is less the behavior decreases slowly up until  $\approx 70^\circ$ .

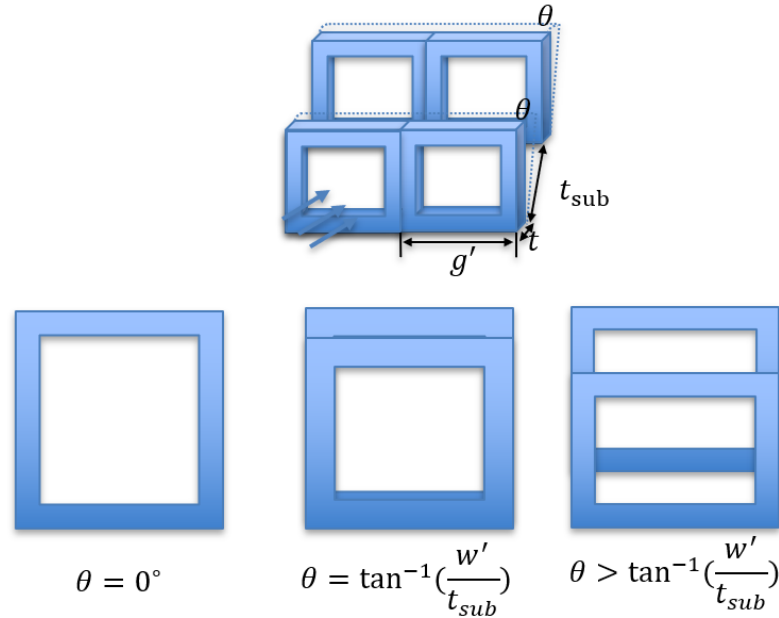


Figure 4.6: two-layer mesh with substrate separating and illustration of the effective fill factor due to the second layer mesh. The simple geometric approximation to the fill factor versus angle of incidence allows the transmittance to be predicted.

To simulate this effect using the values that were fabricated  $w' = 5 \mu\text{m}$ ,  $g' = 95 \mu\text{m}$ ,

$t = 1\mu\text{m}$ , and  $t_{sub} = 100\mu\text{m}$ . Substituting the values into (4.3) and varying the angle  $\theta$  gives the response in Fig. 4.7.

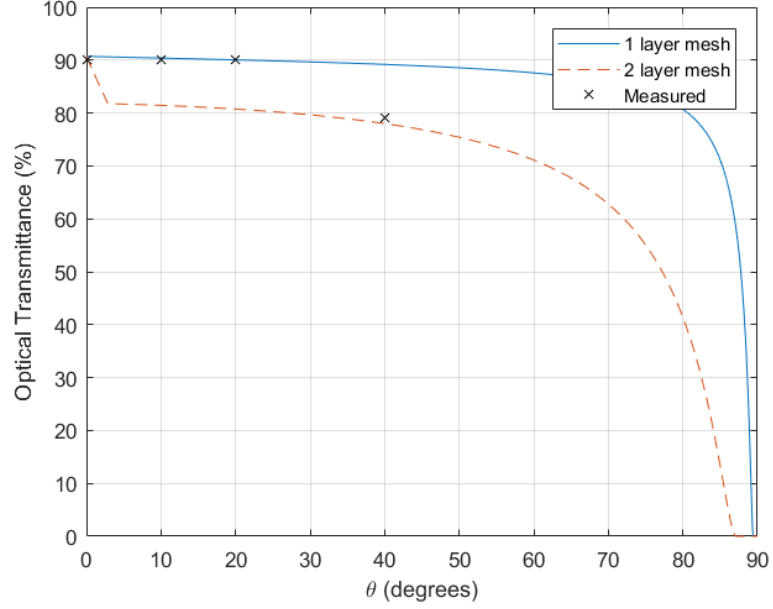


Figure 4.7: Simulation of transmittance versus angle for a two-layer mesh with substrate separating and illustration of the effective fill factor due to the second layer mesh. Mesh parameters same as fabricated values as  $w' = 5\mu\text{m}$ ,  $g' = 95\mu\text{m}$ ,  $t = 1\mu\text{m}$ , and  $t_{sub} = 100\mu\text{m}$ .

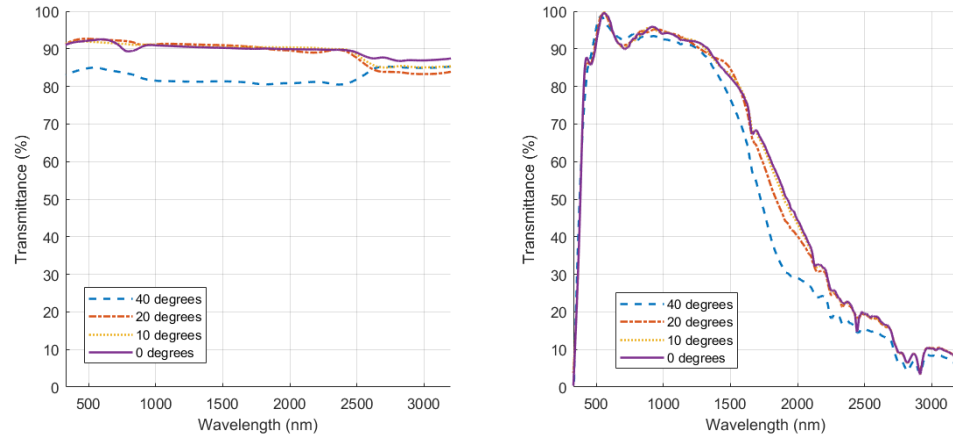


Figure 4.8: Transmittance vs wavelength of ITO (right), mesh (left) with baseline PET and Willow glass divided out and captured incident angles of 0, 10, 20, 40 degrees.

Comparing the expected values with the measured values shows discontinuity. In the measured sample the front side included patch antenna with microstrip feed and the back

was the uniform ground plane. The measurement data for  $10^\circ$  and  $20^\circ$  was likely aligned in a spot where the front side mesh was not being accounted for. For  $40^\circ$ , more surface area of the antenna was being covered by the incident beam, allowing front side mesh to interact with the incident light beam, creating the large decrease in transmittance at the  $40^\circ$  angle.

For ITO at an angle, the effective thickness that the light propagates through the material increases geometrically causing the  $\alpha_\kappa t$  losses to increase as angle increases.

## 4.2 Imaging through Transparent Conductors

Aside from transmission and sheet resistance, optical imaging applications require an additional step of analysis. Depending on whether the imaging system is coherent or incoherent will determine the level of analysis.

### 4.2.1 Imaging Background

Imaging applications, typically characterize systems in terms of a point spread function ( $PSF$ ) or more commonly the optical transfer function ( $OTF$ ) where the spatial Fourier transform of the  $PSF$ , gives the  $OTF$  given as,

$$PSF \xrightarrow{\mathcal{F}} OTF, \quad (4.5)$$

which can be split into the magnitude and phase as

$$MTF = |OTF|, \quad (4.6)$$

and the angle ( $\angle$ ) is

$$POTF = \angle(OTF), \quad (4.7)$$

where  $MTF$  is the modulation transfer function and the  $POTF$  is the phase optical transfer function. The  $PSF$  and  $MTF$  are used when discussing an optical systems sharpness and

resolution. Both the mesh and the TCO will impact the imaging system in different ways. For a TCO, the film can be viewed as like any transparent material with index of refraction  $n$ , thickness  $t$ , surface roughness, and transmission  $T$ . As the TCO is typically deposited on another substrate like glass or plastic, the TCO can potentially be neglected if the TCO is thin enough. Otherwise, simple geometric optical analysis can be utilized to consider the refractive effects. In contrast to TCOs, the mesh will be impacted less by refraction but may potentially have diffractive effects. Diffraction plays a large role in limiting the resolving power of any optical instrument (e.g. cameras, telescopes, microscopes, etc). The diffraction limit describes the optical instrument's ability to distinguish two point sources in close proximity to one another at a given distance. Depending on the mesh geometry and the wavelength(s) of interest, diffraction may occur at the mesh surface, and the point spread function of the imaging system may be affected [118]. Ultimately, the mesh has the potential to reduce the imaging quality or sharpness of an optical system.

Additionally, for a coherent imaging system that depends on the phase content of the return, the entire  $OTF$  must be accounted for. Since the digital camera does not account for phase information of a return signal, the  $OTF$  was not required. For coherent optical systems, the  $OTF$  will need to be accounted for both ITO and mesh samples of the optical aperture. The mesh will have non-uniform phase over the aperture due to the geometry. The transparent conducting oxide, however, will undergo a uniform phase shift based on its index of refraction, but the phase change will be static, the phase different can be calibrated out reducing the effects.

In the imaging community, there are many different methods to determine the resolving power over a diffraction limited imaging system. The classical method is using the USAF 1951 Target, Fig. 4.9. The resolution test target consists of a pattern of three bar targets periodically decreasing in size. The target typically covers a large range of 0.25 to 228 line pairs-per-millimeter (lp/mm). The element observed without distinct image contrast indicates the approximate resolution limit. The digits on the chart indicate the row and

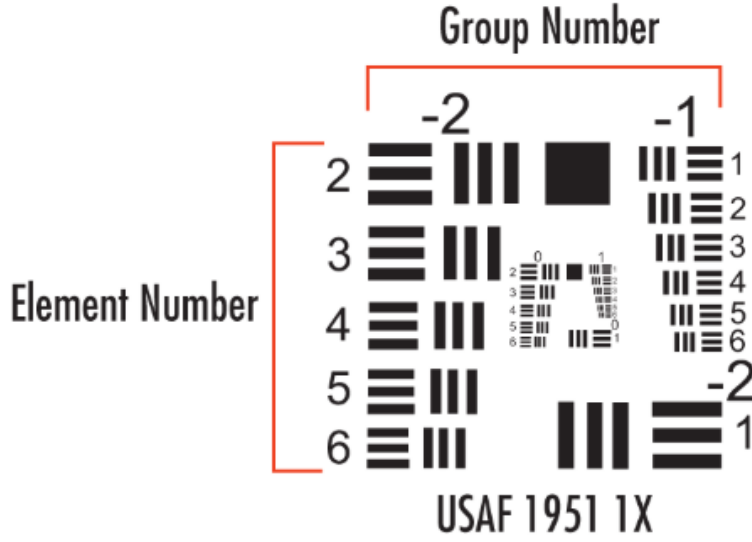


Figure 4.9: USAF 1951 Resolution Target

column location in the series table, which in turn defines the spatial frequency of each element, and thus the available resolution of the system and is calculated by

$$Resolution = 2^{group + \frac{element-1}{6}}, \quad (4.8)$$

where the group number represents the different sections and the element number is the line pairs within the groups. The resolution equation gives the resolving power of an optical imaging system, where the first element that cannot be resolved is the resolution limit of the system. For single aperture sensing, the degradation of resolution from the introduction of a transparent conductor in the aperture must be discussed. As alluded to earlier, the mesh will likely degrade the imaging system more than that of a transparent conducting oxide film, which will instead have refractive effects. The USAF method, which uses the periodic lines for resolution extraction, is robust, but very outdated in the age of digital signal processing using MATLAB.

A more recent method is to use the slant-edge method [119]. Using a similar process outlined in [119], the PSF can be simply extracted by first obtaining the edge spread func-

tion  $E(x)$  (ESF). Taking the derivative of the ESF, gives the line spread function  $L(x)$  (LSF) shown as

$$L(x) = \frac{dE(x)}{dx}, \quad (4.9)$$

where  $x$  is either pixel or distance (typically in milli-meters). Taking multiple slant angles allows the LSF to be interpolated into a PSF. The modulation transfer function is a measure of the ability of an optical system to transfer various levels of detail in the image. The *MTF* incorporates resolution and contrast into a single metric. The *MTF* gives an optical systems spatial frequency response (SFR). For a typical finite lens, its *MTF*, and hence ability to resolve high spatial frequencies, is limited by its finite aperture. Many different standards to measure the slant edge target have been developed as the technology evolves. ISO12233:2000 offers a more updated test chart which allows multiple slant edge samples to be easily captured with the standard line-pairs readily available for immediate resolution characterization.

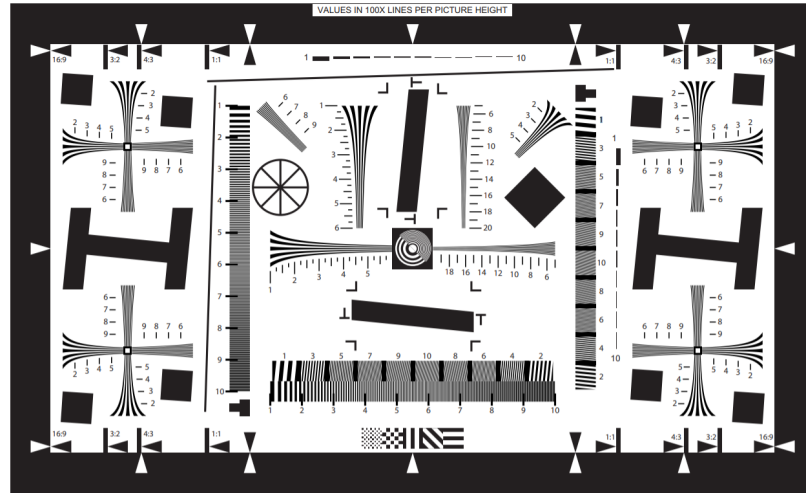


Figure 4.10: ISO12233:2000 Slant Edge Resolution Target with slant targets and resolution line pairs shown.

#### 4.2.2 Imaging Set-up

The slant edge method follows simple process outlined by the ISO 12233 spatial frequency response evaluation method in Fig. 4.11.



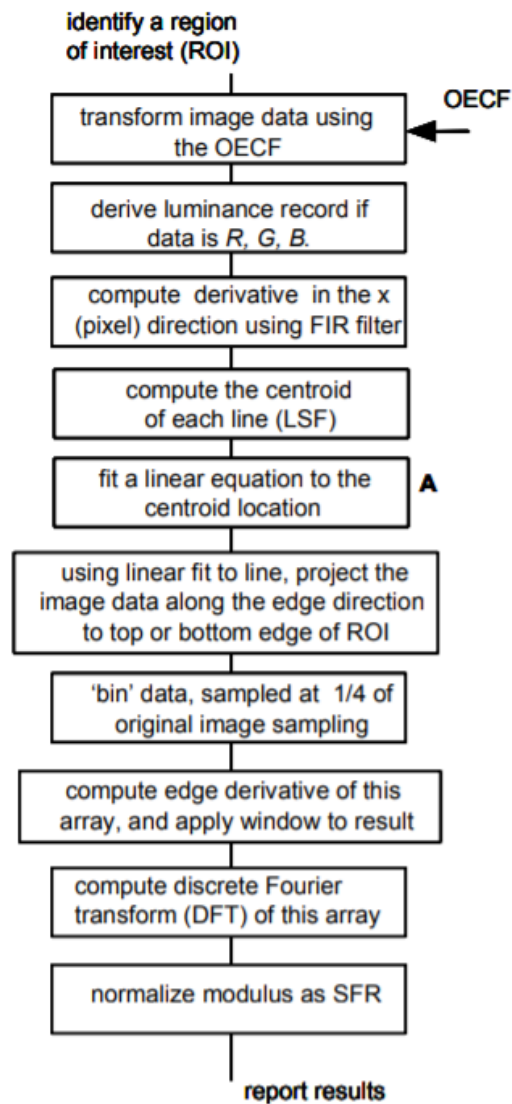


Figure 4.11: ISO12233 spatial frequency response extraction method [120]

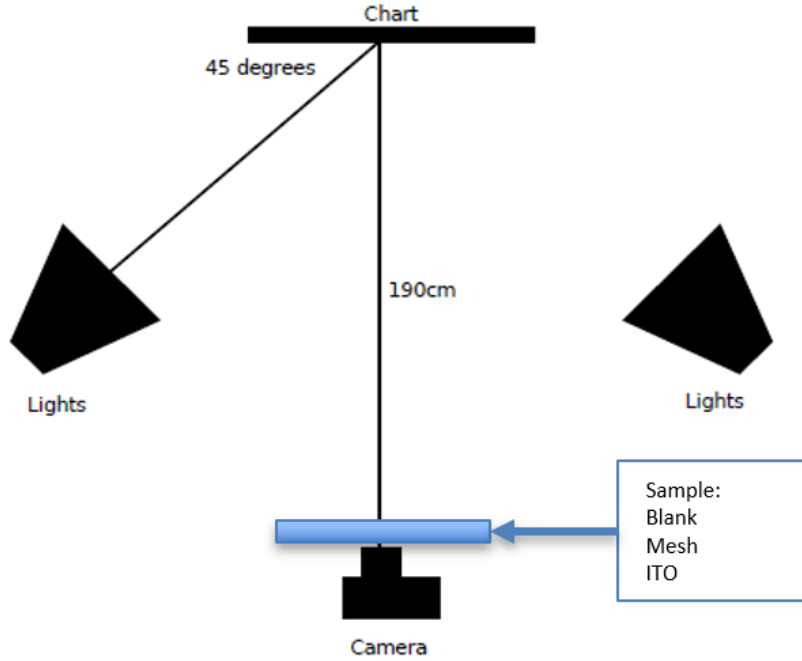


Figure 4.12: Modified set-up of the slant-edge method as described in the slant-edge repeatability study with mesh and ITO samples in front of the lens [119].

Using a Nikon D7500 DSLR camera and the process outlined above, an extraction can be performed to get more information on the materials effect on the imaging quality using the setup shown in Fig. 4.12, which is modified from [119]. The first step is to obtain the *ESF*, which displays how the imaging system responds to a sharp edge. Using the slanted-edge technique, a mapping can be performed as shown in Fig. 4.13. This mapping is used to determine the effective edge spread function for the given slant angle, typically between 5-15 degrees [119].

Table 4.1: Summary of set-up and Nikon DSLR camera settings for *MTF* imaging experiment.

Distance	190 cm
F-Stop	f/6.3
Focal Length	135 mm
Max Aperture	4.5
ISO speed	ISO-1000
Pixel Pitch	4.2 $\mu\text{m}$

The next step is to take the slant edge image of the three scenarios, (raw image or

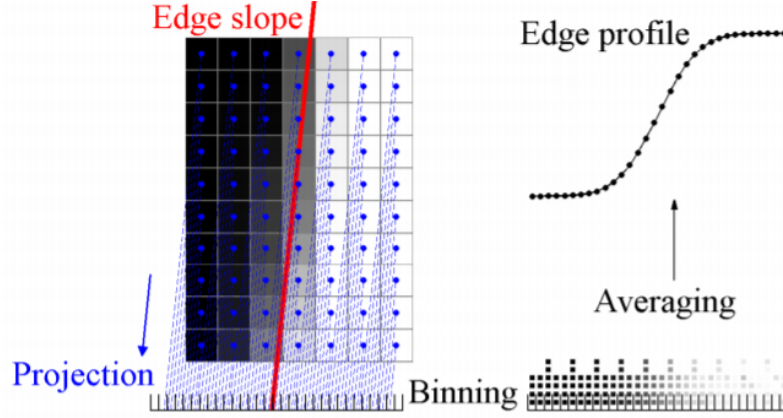


Figure 4.13: Diagram showing how the slant edge is projected, binned, and averaged to create a one-dimensional profile from the two-dimensional dataset [121].

blank, mesh, and ITO) The raw files are shown in Fig. 4.17. The slant image is input into the `sfrmat3.m` function to output the  $MTF$  of the three scenes, shown in Fig. 4.18 with the regions of interest shown in Figs. 4.14, 4.15, and 4.16. The  $MTF$  is shown over spatial frequency in terms of cycles/pixel which makes it easy to point out the Nyquist frequency of 0.5 cycle/pixel. Using the process outlined above the  $MTF$  of the individual transparent conductors can be extracted. Like any transfer function, the  $MTF$  of optical systems can be cascaded giving the total system  $MTF$ . Using the linearity of the  $MTF$ , the individual  $N$   $MTF$ 's can be multiplied to give the  $MTF$  of the entire system  $MTF_{system}$  as

$$MTF_{system} = MTF_1 MTF_2 \dots MTF_N. \quad (4.10)$$

In the experiment of the transparent conductors over the camera lens we will have the  $MTF$  of the system  $MTF_{system}$ , the camera plus lens  $MTF_{camera}$ , and the transparent conductor over the aperture  $MTF_{TC}$ . (Note: for both cases (mesh and ITO), the conductors are on a substrate, Willow glass for the mesh and PET for the ITO. This setup is realistic unless the conductor is deposited directly on the glass of the lens.)

Exploiting the linearity of the  $MTF_{system}$ ,  $MTF_{TC}$  can be given as

$$MTF_{TC} = \frac{MTF_{system}}{MTF_{camera}}. \quad (4.11)$$

#### 4.2.3 Imaging Measurements and Analysis

The results from the  $MTF$  extraction are shown in Fig. 4.19. The  $MTF$  data shows that as the spatial frequencies increase, the resolution and contrast decrease for both an ITO sample and mesh sample over the aperture. The mesh has a stronger effect, decreasing the  $MTF$  by almost 0.1 up to Nyquist of 0.5 cycles/pixel. The degradation is due to the fact that in the visible region, ITO showed a higher level of transmittance, as a result has higher contrast. The diffractive effects of the mesh are present, but minimal since the mesh pitch is much greater than the  $4.2\mu\text{m}$  pixel pitch of the camera.

At Nyquist frequency (0.5 cycles/pixel) the ITO  $MTF$  is 18% higher than that of the mesh due to the contrast and geometry of the mesh. This means the ITO can handle higher spatial frequency content than the mesh can. The 3 dB points for the mesh occurs at 0.5 cycles/pixel, where ITO is above Nyquist at 0.6 cycles/pixel. Further analysis will need to be performed in future work.

Areas of exploration include experiments with different aperture sizes (i.e. smart-phone camera, DSLR, telescope.), varying the mesh pitch be much greater and on the same order as the pixel pitch, non-uniform mesh, misaligned mesh, full antenna array etc. From the initial analysis presented, the mesh and ITO performance is comparable and the degradation of contrast and resolution of the mesh is similar to of ITO making the mesh available for use in imaging applications. A concern was the diffractive effects introduced by the mesh would degrade the performance, but only slight degradation was shown in the initial measurements presented.

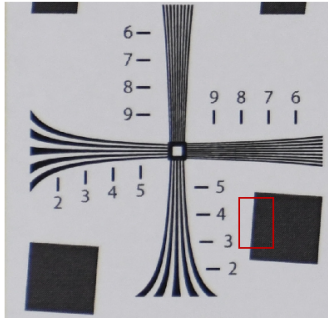


Figure 4.14: Baseline image of slant target with area of interest in red.

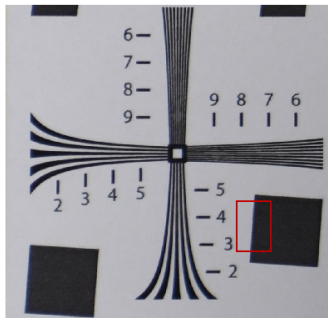


Figure 4.15: Image of slant target with mesh conductor over aperture with area of interest in red

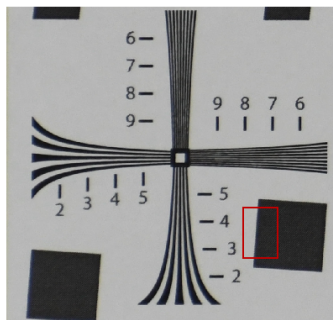


Figure 4.16: Image of slant target with ITO conductor over aperture with area of interest in red

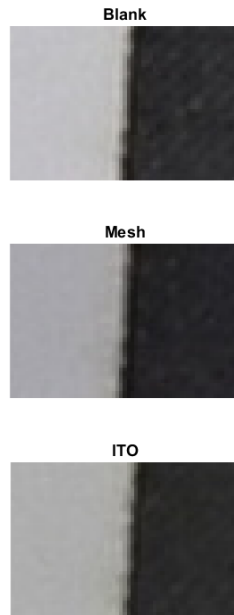


Figure 4.17: Sample of slant-edge data for a raw (uncovered) aperture, a metal mesh covered aperture, and an ITO covered aperture.

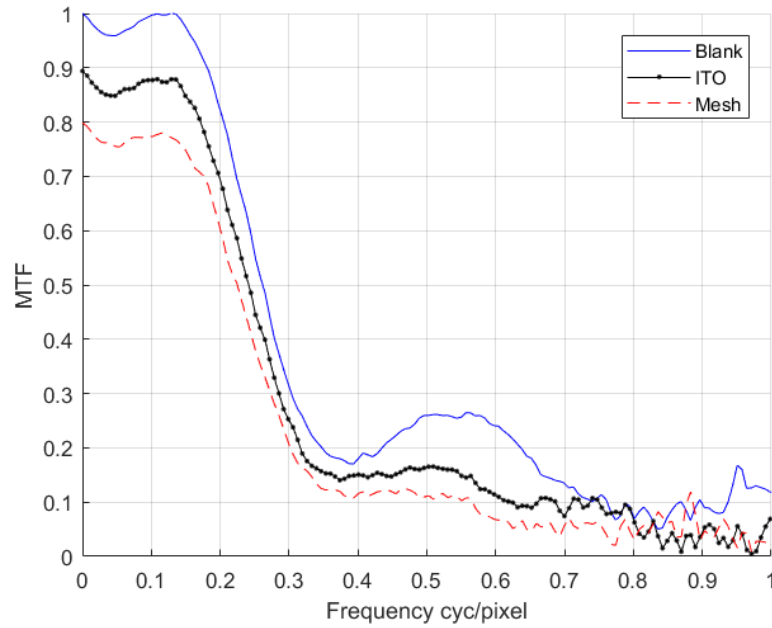


Figure 4.18: Processed  $MTF$  of the slant-edge data for a raw (uncovered) aperture, a metal mesh covered aperture, and an ITO covered aperture using sfrmat3.m.

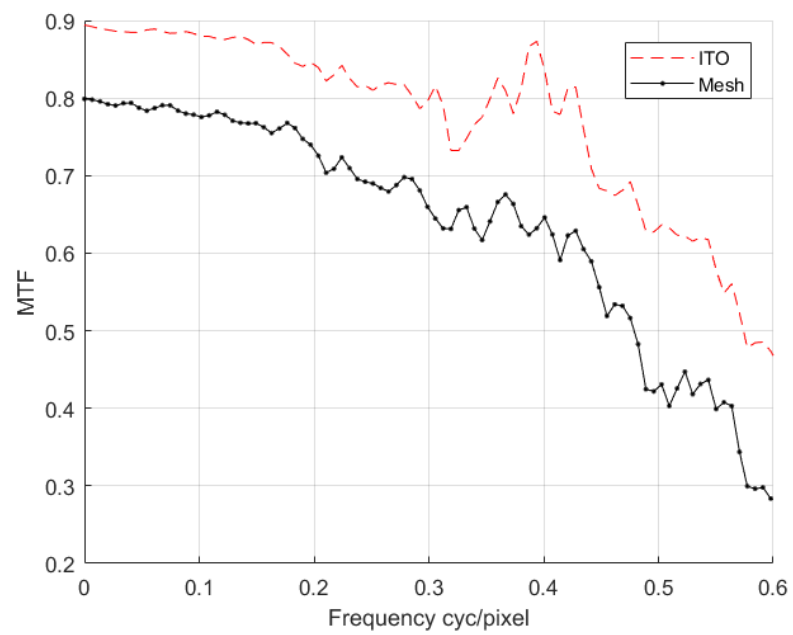


Figure 4.19: Extracted  $MTF$  displaying individual spatial frequency response of mesh and ITO.

## CHAPTER 5

### CHARACTERIZATION OF MESH CONDUCTOR FOR MICROSTRIP TRANSMISSION LINES AND ANTENNAS

---

**Chapter Overview:** This chapter provides the following:

- Full characterization of meshed transmission lines with analysis of loss and shift in impedance due to changes in RLGC circuits parameters.
  - Design simulation and measurement of meshed patch antennas with analysis of antenna performance and other changes when adding the mesh.
- 

Using the conclusions from the previous chapter on the optimal transparent conductor for RF, the mesh will be analyzed in the following section. The following analysis for transmission lines will be largely important in developing a methodology to design a patch antenna array which depends on the full understanding of transmission lines and antennas to ensure maximum performance. The chapter will characterize the mesh conductors by its S-parameters, specifically insertion loss ( $|S_{21}|$ ) and return loss ( $|S_{11}|$ ) compared to last chapter where the materials were characterized optically in terms of transmittance, reflectance, and absorbance.

The following work has been accepted for publication to the 2019 MTT-S International Microwave Symposium [93], and an extension will be presented in Transactions MTT-S IMS Special Issue. The antenna work in this section has been accepted to the 2019 IEEE International Symposium on Antennas and Propagation and USNC-URSI Radio Science Meeting [94].



## 5.1 Microstrip Transmission Line

Microstrip transmission lines are widely used in RF and microwave engineering and are used for transferring high frequency energy in quasi-TEM form. transmission lines at high frequencies are known to have the form of an RLGC circuit, where  $R_{pul}$  is resistance per unit length,  $L_{pul}$  is inductance per unit length,  $G_{pul}$  is conductance per unit length, and  $C_{pul}$  is capacitance per unit length [106]. The capacitance is due to the proximity of the conductors, and the inductance represents the self-inductance of the signal trace and the ground plane. In practical designs, the loss of the transmission line is negligible allowing R and G to be neglected. As a result, they won't be discussed in the analysis in this paper. Important microstrip line parameters such as phase velocity, propagation constant, characteristic impedance and the RLGC parameters can be extracted from the S-parameters using S-parameters to Z- and Y-parameter identities. The RLGC parameters give the approximate propagation constant; characteristic impedance  $Z_c$  shown in (5.1); operating frequency shown in (5.2) where the  $\Delta x$  balances the units inductance and capacitance; and phase velocity of the transmission line.

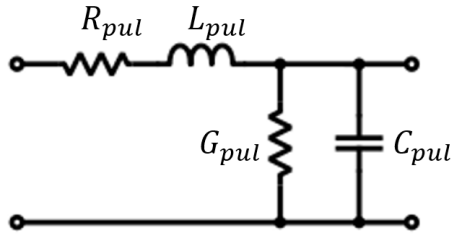


Figure 5.1: Lumped element RLGC circuit model for transmission lines

In addition to the RLGC parameters, effective permittivity is an important quantity which governs much of the propagation behavior and determine impedance and phase length to design an RF microstrip circuit [122]. The effective permittivity  $\epsilon_e$  can be computed using (5.3), where  $\epsilon_r$  is the relative permittivity,  $W$  is the width of the transmission line, and  $d$  is the height of the substrate [122]. In addition, the phase  $\phi$  of the transmission

line can be found using (5.4), where  $k_0 = \beta = 2\pi/\lambda$  is the propagation constant in air, and  $l$  is the length of the transmission line.

$$Z_c = \sqrt{\frac{L_{pul}}{C_{pul}}} \quad (5.1)$$

$$f = \frac{1}{2\pi\sqrt{L_{pul}C_{pul}\Delta x}} \quad (5.2)$$

$$\frac{\epsilon'_e}{\epsilon_o} = \frac{\epsilon_r + 1}{2} + \frac{\epsilon_r - 1}{2} \frac{1}{\sqrt{1 + \frac{12d}{W}}} \quad (5.3)$$

$$\phi = \sqrt{\frac{\epsilon'_e}{\epsilon_o}} k_0 l \quad (5.4)$$

## 5.2 S-parameters to RLGC

In RF measurements, the data gathered is a scattering matrix called S-parameters. The scattering matrix provides complete information of any N-port network, and for a microstrip transmission line structure this is a two-port network. The S-matrix is defined as the ratio of the reflected and incident voltage waves  $V_i^-$  and  $V_j^+$ , respectively, as

$$S_{ij} = \frac{V_i^-}{V_j^+}, \quad (5.5)$$

where  $S_{ij}$  is a complex quantity holding magnitude and phase information.

For the transmission lines measured,  $S_{11}$  and  $S_{22}$  are known as the reflection coefficients whereas  $S_{21}$  and  $S_{12}$  are the transmission coefficients. To convert the S-matrix into an impedance matrix (Z-matrix), the conversions

$$Z_{11} = Z_0 \frac{(1 + S_{11})(1 - S_{22}) + S_{21}S_{12}}{(1 + S_{11})(1 - S_{22}) - S_{21}S_{12}}, \quad (5.6)$$

$$Z_{12} = Z_0 \frac{2S_{12}}{(1 + S_{11})(1 - S_{22}) - S_{21}S_{12}}, \quad (5.7)$$

$$Z_{12} = Z_0 \frac{2S_{21}}{(1 + S_{11})(1 - S_{22}) - S_{21}S_{12}}, \quad (5.8)$$

and

$$Z_{22} = Z_0 \frac{(1 + S_{11})(1 - S_{22}) + S_{21}S_{12}}{(1 + S_{11})(1 - S_{22}) - S_{21}S_{12}}, \quad (5.9)$$

are used where  $Z_0$  is the reference impedance of the VNA, typically  $50 \Omega$ . Now instead of an S-matrix, the network is described in terms of voltage and current, otherwise known as a Z-matrix. Using the propagation constant  $\gamma$

$$\gamma = \alpha + j\beta = \sqrt{(R_{pul} + j\omega L_{pul})(G_{pul} + j\omega C_{pul})} \quad (5.10)$$

from the measured complex s-parameters, along with the new Z-matrix, the RLGC parameters can be extracted as [123]

$$R_{pul} = \text{Re}(\gamma Z_0), \quad (5.11)$$

$$L_{pul} = \frac{\text{Im}(\gamma Z_0)}{2\pi f}, \quad (5.12)$$

$$G_{pul} = \text{Re}\left(\frac{\gamma}{Z_0}\right), \quad (5.13)$$

and

$$C_{pul} = \frac{\text{Im}(\gamma/Z_0)}{2\pi f}, \quad (5.14)$$

where  $f$  is the desired frequency. As these parameters change versus frequency, it will be important to extract the RLGC parameters at a single frequency for direct comparison of the mesh transmission lines.

### 5.3 Meshed Transmission Line with Solid Ground Plane

Introducing a mesh to a transmission line will likely cause changes to the properties of the transmission line, even when obeying the Rayleigh criterion. The mesh alters the inherent capacitance and inductance of the solid transmission line. Basic electromagnetic theory suggests a meshed transmission line will decrease the capacitance and increase inductance based on the geometrical aspects of the mesh. From the geometry of the microstrip transmission line, one would expect the capacitance to decrease and the inductance to increase as the fill factor decreases (as more metal is removed). If inductance increases and capacitance decreases, from (5.1)  $Z_c$  increases.

#### 5.3.1 Proposed Modification to Effective Permittivity

Introducing a mesh to a microstrip transmission line signal trace will affect the effective permittivity as a function of the fill factor. Equation (5.15) for the effective permittivity of a mesh region of a transmission line  $\epsilon_e^{mesh}$ , includes the fill factor and will be verified in the Section 5.3.3. The modification allows the open area of the mesh to be taken into account in the effective permittivity for BB' of Fig. 5.2a. The cross section is used to describe an effective permittivity, which is also a weighted average of the permittivity. For the mesh, the effective permittivity will increase. The  $\sqrt{\Psi}$  in (5.15) can be described by the physical phenomena where the mesh added an electrical width to the transmission line due to the fringing fields of the transmission line which increase in the mesh due to the added inductance within the trace, and the decreased capacitance between the trace and the ground plane.

$$\epsilon_e^{mesh} = \frac{\epsilon'}{\epsilon_o} = \frac{\epsilon_r + 1}{2} + \frac{\epsilon_r - 1}{2} \frac{1}{\sqrt{1 + \frac{12d\sqrt{\Psi}}{W}}} \quad (5.15)$$

### 5.3.2 Simulation vs Measurement

Two microstrip transmission line models were simulated, fabricated, and measured. The board was made using copper conductor, FR4 substrate ( $\epsilon_r = 4.6$ ) with thickness 1.6 mm as shown in Fig. 5.3. Table 5.1 shows the design parameters for both transmission line structures. The solid transmission line, trace 1, was designed to be  $50 \Omega$  and the meshed transmission line kept the trace width constant to later analyze the effect of the mesh on a transmission line of the same dimensions. The simulations were carried out in CST Microwave Design Suite and fabricated board was made by Oshpark. Simulation and measurement of the mesh and solid transmission line are shown in Fig. 5.5. The solid transmission line was designed to have  $|S_{11}|$  below -10 dB from 2 to 4 GHz. The measured data shows agreement with the simulation which allows for a parametric study to be carried out using the mesh transmission line. In simulation and measurement of the meshed transmis-

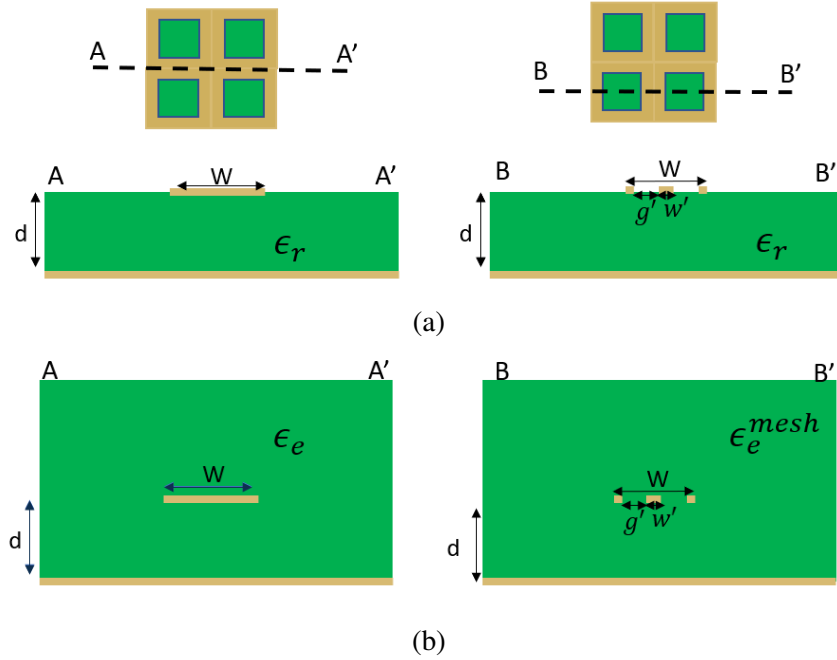


Figure 5.2: (a) Unit cell with cross section of dielectric and air interface. AA' is the portion with solid transmission line. BB' is the portion with an open gap in the transmission line. (b) Cross section showing the effective permittivity covering the full region of the transmission line.

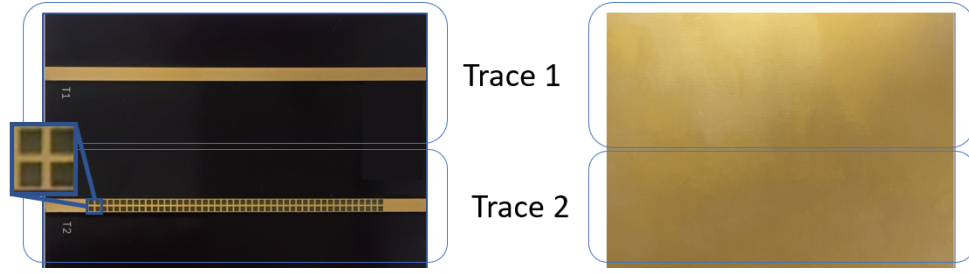


Figure 5.3: Fabricated board with the solid transmission line (Trace 1) and the meshed transmission line (Trace 2).

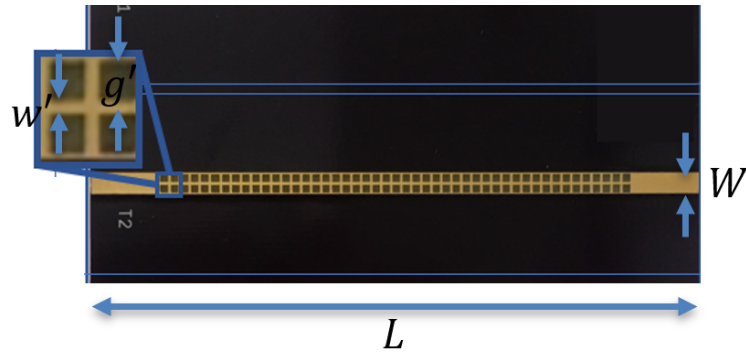


Figure 5.4: Parameterized mesh transmission line board parameters

sion line, a shift in the return loss is evident from 3 GHz in the solid transmission line to 2.7 GHz in the meshed transmission line. The insertion loss in Fig. 5.5 shows a larger loss in the meshed transmission line in both the simulation and measurement at 2.4 GHz, but only by about 0.1 dB between the solid and meshed transmission line measurements and 0.2 dB in simulation. The initial S-parameters show there is likely a shift in the impedance and electrical length due to adding a mesh, but a further S-parameter extraction will be carried out in Section 5.3.3 to verify the results. Fig. 5.6a and 5.6b show the quasi-TEM field distribution in the solid meshed transmission line to display the propagation in simulation at 2.4 GHz which shows a small change within the meshed transmission line likely due to the added inductance due to the meshed lines.

Table 5.1: Solid transmission line and meshed transmission line design parameters.

Parameter	Dimension	
Thickness, $d$	1.6 mm	1.6 mm
$\epsilon_r$	4.6	4.6
Trace Width, $W$	2.92 mm	2.92 mm
Length	88.95 mm	88.95 mm
Fill Factor, $\Psi$	1	0.21
Mesh Spacing, $g'$	—	1.15 mm
Mesh Line Width, $w'$	—	0.31 mm

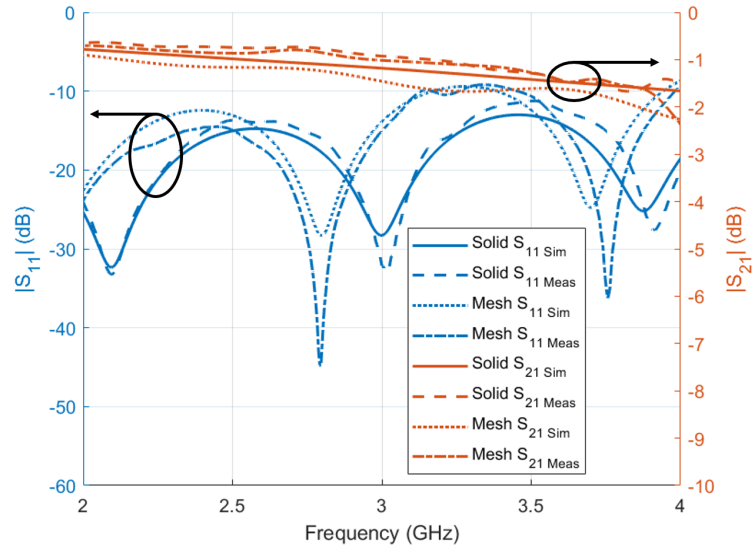


Figure 5.5: Simulated and measured transmission line  $|S_{11}|$  reference left axis and  $|S_{21}|$  reference right y-axis. Measured data for the solid and mesh transmission lines shown in Fig. 5.3.

### 5.3.3 Meshed vs Solid Comparison

A parametric sweep was carried out which varied the fill factor but kept the unit cell size  $g' + w'$  constant. Keeping the unit cell size constant allows the fill factor to be the only variable allowing the changes in geometry to be easily tracked in the parametric study. fill factor will be varied between 0.05 and 1.

Performing a fill factor parameter sweep, the RLCG parameters can be extracted at 2.4 GHz from the S-parameters. Of the RLGC parameters the L and C are most important to verify the intuition that the inductance would increase, and the capacitance would de-

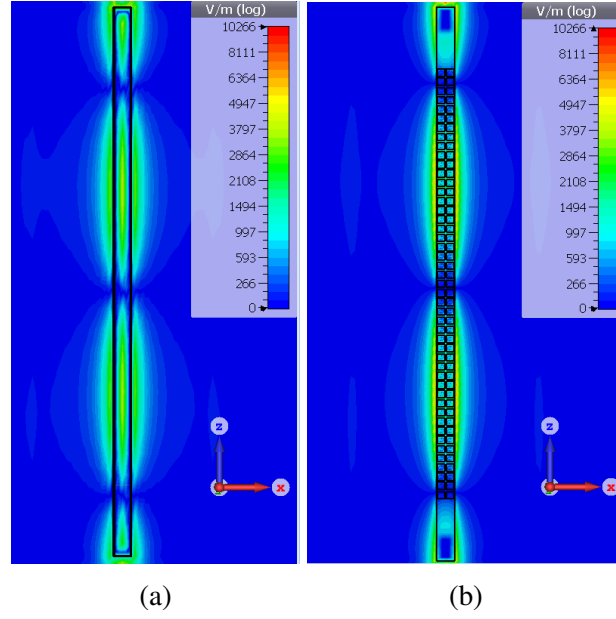


Figure 5.6: Simulated electric field at 2.4 GHz of (a) solid transmission line (b) mesh transmission line with a solid ground plane

crease as fill factor decreases. Table 5.2 shows the results in the  $L$  and  $C$  columns. As fill factor decreases, the  $L$  increases by  $L_{pul} \approx 46(pH/m)/\Psi$  and a decrease of  $C_{pul} \approx 13.7(fF/m)/\Psi$ . The changes in  $L$  and  $C$  will create a frequency shift that can be seen in Fig. 5.5 since resonant frequency is given by (5.2).

Table 5.2: Simulated transmission line with solid ground plane parameters versus fill factor.

$\Psi$	$S_{21}$ Phase, $\phi(^{\circ})$	$\epsilon_e$	$L_{pul}$ (nH/m)	$C_{pul}$ (pF/m)	$Z_o$ ( $\Omega$ )
0.05	-538.74	3.828	0.144	0.0298	69.6011
0.09	-536.75	3.758	0.143	0.0305	67.8986
0.21	-531.64	3.642	0.142	0.0317	64.9887
0.30	-528.16	3.596	0.137	0.0332	64.4353
0.42	-525.44	3.558	0.116	0.0355	57.0512
0.55	-523.97	3.534	0.114	0.0359	56.2787
0.66	-521.64	3.519	0.109	0.0370	54.3593
0.78	-521.63	3.510	0.108	0.0381	54.1933
1.00	-521.33	3.504	0.099	0.0397	50



#### 5.4 Mesh Transmission Line and Mesh Ground Plane

Similar analysis has been shown for a mesh transmission line with meshed ground plane and the results are expected to be very similar. The analysis is being prepared for submission to IEEE Transactions on MTT Special Issue on the 2019 IEEE MTT-S International Microwave Symposium. Using a similar transmission line structure, an extended analysis is presented showing the results of the electric length, RLGC, and loss per meter versus the change in fill factor and unit cell size. An example fabricated model is shown in Fig. 5.7.

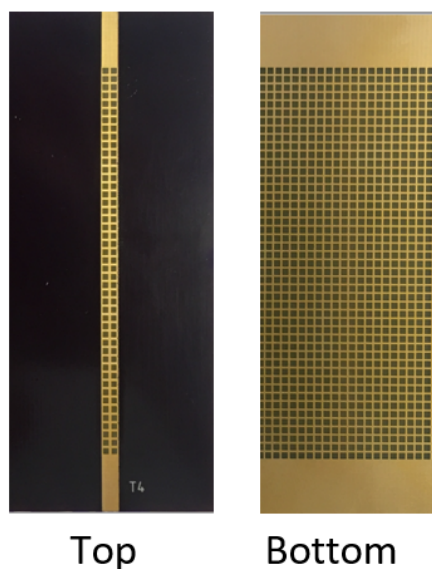


Figure 5.7: Top and bottom example of microstrip transmission line with meshed trace and ground plane.

Using the same design parameters shown in Fig. 5.4, a shorter length ( $L = 31.00$  mm) TL design was used to speed up the simulation time rather than using the 88.95 mm length as before. Using a different length will also expand the study rather than constraining the results to a single length TL. This design was simulated using Rogers 4003C substrate parameters. The design parameters are shown in Table 5.3.

The study on the meshed transmission line with meshed ground plane will observe effects of loss (dielectric and conductive) as well as the changes in RLGC. Using Rogers

Table 5.3: Solid transmission line and meshed transmission line design parameters.

	Parameters
Thickness, $d$	0.503 mm
$\epsilon'/\epsilon_o$	3.38
Trace Width, $W$	1.23 mm
Length	31.00 mm

4003 which has thickness 0.503 mm, relative permittivity  $\epsilon_r = 3.38$ , with 1 oz copper the mesh transmission line traces can be milled using a laser milling machine with high precision and manufacturing speed.

The inductance and capacitance relationship to fill factor follows a relationship closely related to

$$C_{theory} = C_{solid} (2\Psi - \Psi^2)^{0.1} \quad (5.16)$$

$$L_{theory} = L_{solid} (2\Psi - \Psi^2)^{-0.1} \quad (5.17)$$

where  $L_{solid}$  is the solid transmission line or  $\Psi = 1$ . The  $(2\Psi - \Psi^2)$  in (5.16) and (5.17) is the area of the material that is present and is weighted by the fractional exponent is from an interpolation of the data and accounts for the fringing capacitances and inductances. The main trend to note is that as fill factor decreases (more material is taken away)  $L_{pul}$  increases and  $C_{pul}$  decreases, as shown in Fig. 5.8 and Fig. 5.9 respectively. The results are as expected from the analysis using a meshed transmission line and solid ground plane. The meshed ground plane increases the effects of changes in  $L_{pul}$  and  $C_{pul}$ . Understanding the relationships between,  $L_{pul}$  and  $C_{pul}$  it is easy to see that the characteristic impedance of the meshed transmission line will increase, shown in Fig. 5.10. A relationship between the impedance and fill factor is shown, with a similar trend to that of the inductance per unit length. Along with impedance, another interesting behavior is the total power loss from the transmission line. Many transmission line models use lossless assumptions, neglecting both dielectric and conductor loss. As the fill factor increases, it is expected that the conductor loss will also increase, since the skin depth is also increasing. Figs. 5.11 and 5.12 shows

the expected behavior over frequency, validating the hypothesis on conductor loss as the conductor is taken away. The lost power is likely due to power leakage in addition to the skin depth losses that occur.

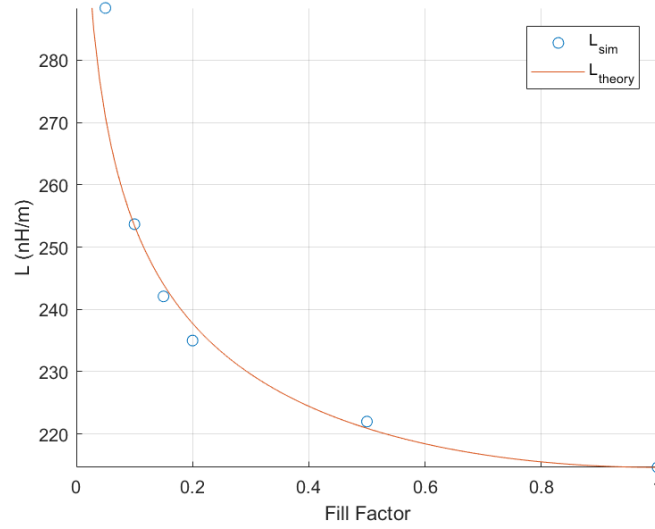


Figure 5.8: Inductance versus fill factor with simulated values extracted from s-parameters and a theoretical model based on (5.17)

Table 5.4: Simulated meshed transmission line parameters with meshed ground plane versus fill factor.

$\Psi$	$S_{21}$ Phase, $\phi(^{\circ})$	$L_{pul}$ (nH/m)	$C_{pul}$ (pF/m)	$Z_o$ ( $\Omega$ )
0.05	-162.292	288	117	62.2
0.10	-161.764	254	132	56.3
0.15	-160.604	242	137	54.5
0.2	-159.466	227	141	52.5
0.5	-157.286	226	145	52.2
1.00	-157.158	214	153	50

#### 5.4.1 Compensating for the Propagation Effects Introduced by the Mesh Conductor

Based on the changes in capacitance and inductance, matching the meshed transmission line impedance to  $50 \Omega$  can be executed by increasing the width  $W$  of transmission line which will increase the capacitance while decreasing the inductance of the signal trace. Increasing the width from 2.92 mm to 4.3 mm (keeping other parameters the same from Table 5.1) for a solid transmission line will increase the capacitance and decrease the inductance to lower the impedance from  $50 \Omega$  to  $38 \Omega$ , but applying mesh with parameters  $\Psi = 0.16$ ,  $g' = 1.8mm$  and  $w' = 0.35$  will bring the impedance back up to  $50 \Omega$  to minimize reflections (return loss below 25 dB) and insertion loss around 0.9 dB at 2.4 GHz as displayed

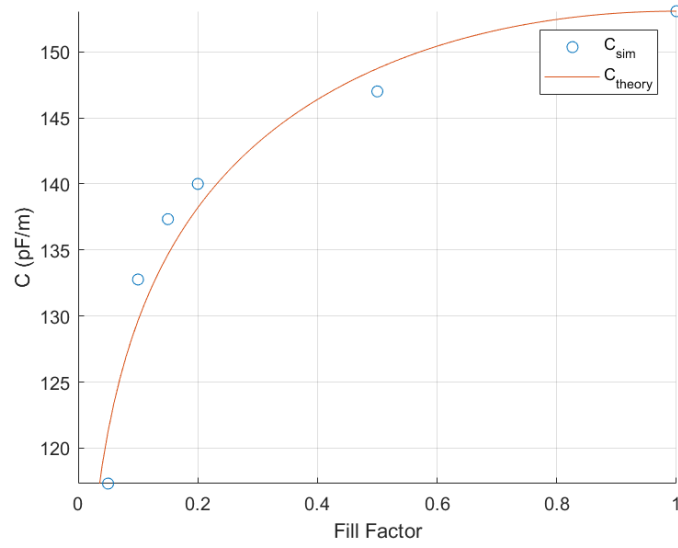


Figure 5.9: Capacitance versus fill factor with simulated values extracted from s-parameters and a theoretical model based on (5.16)

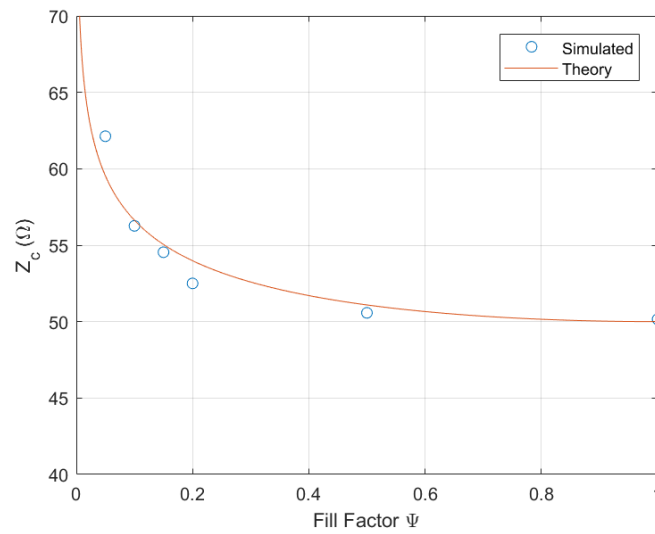


Figure 5.10: Impedance versus fill factor extracted from the s-parameters.

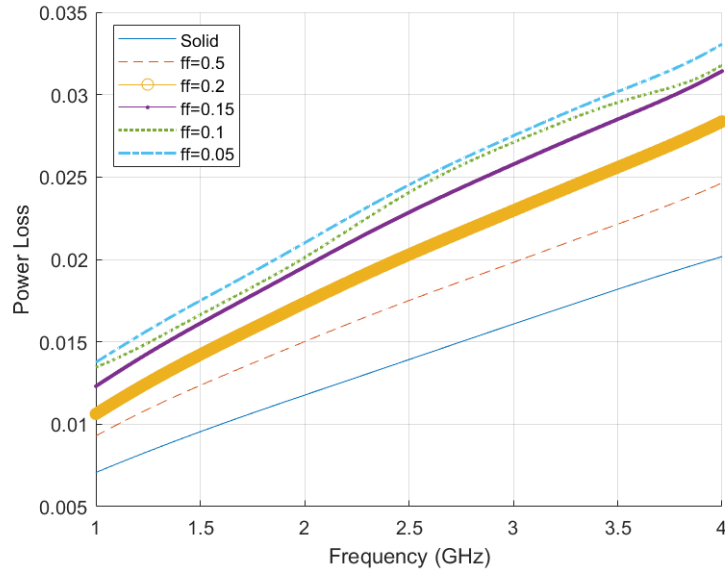


Figure 5.11: Power loss at different fill factors over the simulated frequency range. Note loss increase as the frequency increases; this includes dielectric and conductor loss in the simulations. As fill factor decreases, the loss increases as expected.

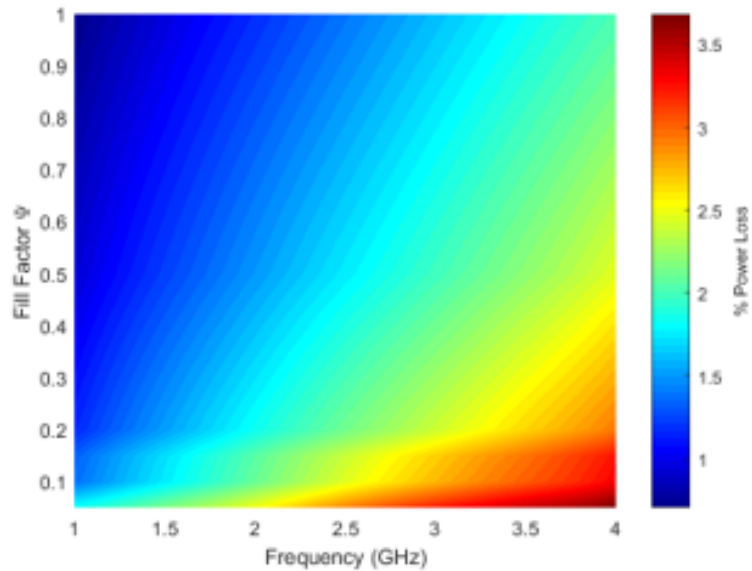


Figure 5.12: Interpolated power loss versus fill factor versus the simulated frequency range. Note loss increase as the frequency increases, this includes dielectric and conductor loss in the simulations. As fill factor decreases, the loss increases as expected.

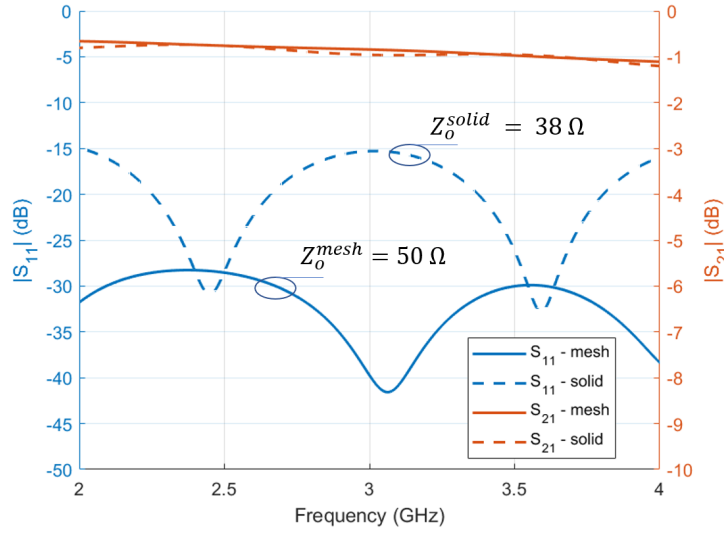


Figure 5.13: Simulated S-parameters to match the meshed transmission line using a lower impedance solid transmission line as the reference.  $W = 4.2\text{mm}$   $\Psi = 0.16$  for  $S_{11}$ -mesh and  $S_{21}$ -mesh (simulated without connectors).

in Fig. 5.13. The phase length of the  $50\ \Omega$  meshed transmission line goes up to  $378^\circ$  from  $364.6^\circ$  for a  $50\ \Omega$  solid transmission line when the total length is  $68.95\text{ mm}$ . Using the trends in Table 5.4 will allow for design equations to match a  $50\ \Omega$  meshed transmission line of any fill factor.

It can be concluded that adding a mesh does affect the transmission line performance as expected. The behavior is predictable based on fill factor and dimensions of the transmission line structure. It was predicted that the mesh would alter the inductance and capacitance per unit length in the transmission line structure and thus alter the impedance. The findings agreed with simulation and measurements using a S-parameter to RLGC conversion. The results were used to compensate for the effects of the mesh to allow the meshed structure to operate at  $50\ \Omega$  by increasing the width of the transmission line.

## 5.5 Meshed Patch Antennas

As seen with the microstrip transmission line, a frequency shift is expected to occur for a meshed patch antenna. For this analysis, to remain constant with parameters, the width of the microstrip feed will not be varied. It has been shown that decreasing the patch length will re-tune the antenna to the correct operating frequency [94].

### 5.5.1 Antenna Design

The dimensioned patch antennas are found in Fig. 5.14. The solid patch antenna and the meshed patch antenna are to be made with the same dimensions ( $W = 29$  mm,  $l = 28.6$  mm,  $a = 4.17$  mm,  $C = 10$  mm,  $D = 8$  mm). The meshed design includes a meshed radiating element and a meshed feed. The ground plane of the antenna on the right is also meshed. In the meshed design, there is a section of solid transmission line and ground plane to allow the SMA connector to be soldered on. The line width  $w' = 0.2$  mm and the pitch  $g' = 2.5$  mm, can be defined by the fill factor,  $\Psi = 0.07$ . The antenna pitch, which equates to  $\lambda_c/20$  (2.89 mm at 2.5 GHz), satisfies the Rayleigh criterion. The antennas are both made on FR-4 with thickness 1.5 mm and  $\epsilon_r = 4.3$ . Though the meshed antenna is not visibly transparent in this paper, the analysis could easily be translated to a meshed antenna on glass.

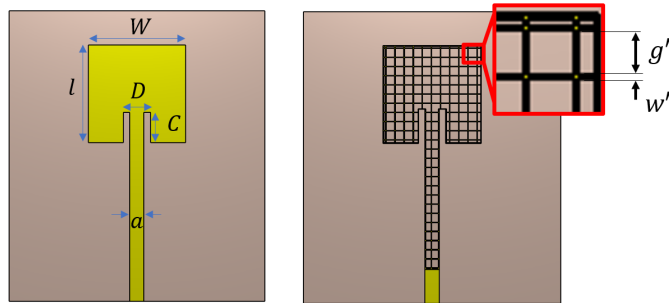


Figure 5.14: (Left) Solid patch antenna with solid ground plane (Right) Mesh patch antenna with same dimensions of  $W, l, a, C, D$  and meshed ground plane (Ground planes not shown).



### 5.5.2 Results

#### *Return Loss*

The return loss for the patch antennas in Fig. 5.14 are shown in Fig. 5.15. The solid antenna shows simulated and measured results resonating at 2.52 GHz with bandwidth, BW, of 69 MHz or 2.66%. The meshed antenna of the same dimensions operates 40 MHz lower at 2.48 GHz with BW at 71 MHz, 2.86%. The shift occurs due to the added inductance and reduced capacitance when introducing a mesh, which has also been observed with a meshed transmission line [93]. The meshed patch antenna geometry must be altered to compensate for the mesh and to resonate at the same frequency as the solid. One method to increase the resonant frequency is decreasing the length  $l$  of the radiating patch, shown in Fig. 5.16. The total decreased length is 1.1 mm or approximately 4% which was determined by relating the frequency shift to the change in electrical length due to the mesh. The decrease in physical length increases the resonant frequency to match the solid design at 2.52 GHz with 80 MHz, 3.2 % BW. The bandwidth of the mesh design has 0.5%, 11 MHz, larger bandwidth than the solid design which is small increase. The return loss of the meshed antenna is almost identical to that of the solid since the mesh was properly tuned and the mesh meets the skin depth requirement at 2.5 GHz minimizing additional losses.

#### *Pattern and Performance*

The patterns will be compared in Fig. 5.17 for the solid patch antenna and the adjusted mesh patch antenna from Fig. 5.16 at 2.52 GHz. The elevation pattern is seen as off-boresight for both the solid and the mesh antenna due to the proximity of the radiating patch to the top edge of the substrate. The peak realized gain for the mesh is 2.95 dBi and the solid antenna is 3.1 dBi, a 0.15 dBi change. One important difference between the two antennas is the front-to-back ratio (FBR) seen in Fig. 5.17. The FBR for the solid is around 23 dB and the FBR for the mesh antenna is 16 dB which equates to a 7 dB decrease for a

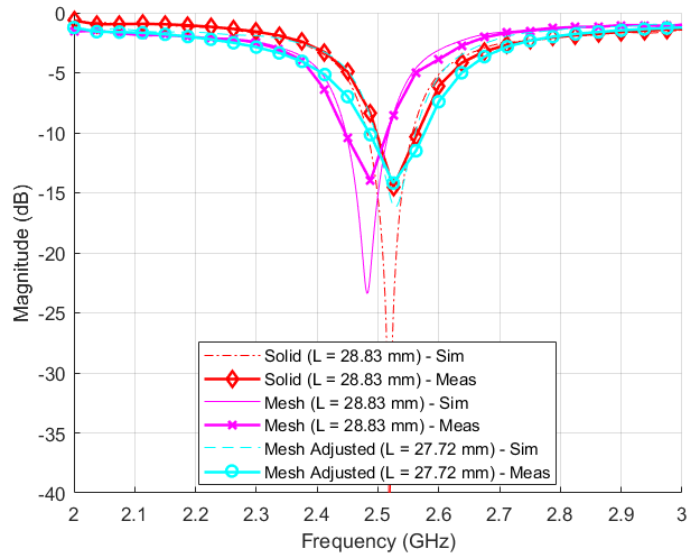


Figure 5.15: Simulated and measured return loss of the antennas from Fig. 5.14 and 5.16.

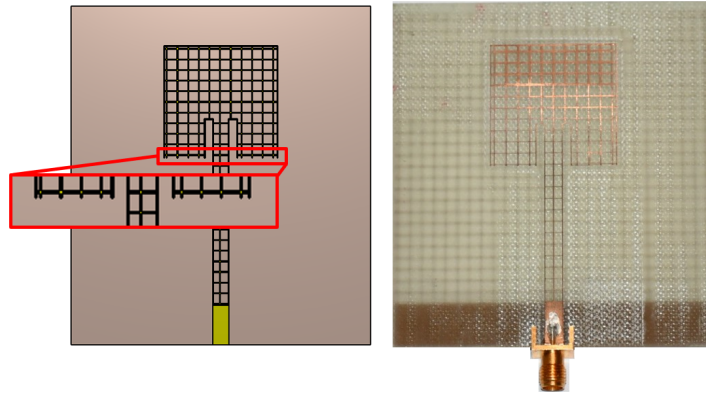


Figure 5.16: Adjusted patch antenna decreasing the length  $l$  by 1.1 mm to be 27.72 mm.  $\Psi, W, a, C, D$  all remain constant. (Left) CST model (Right) Fabricated with SMA connector.

mesh of  $\Psi = 0.07$  with  $\lambda/20$  pitch. This change in FBR is due to the meshed ground plane where the mesh allows some of the propagating waves to leak through the mesh.

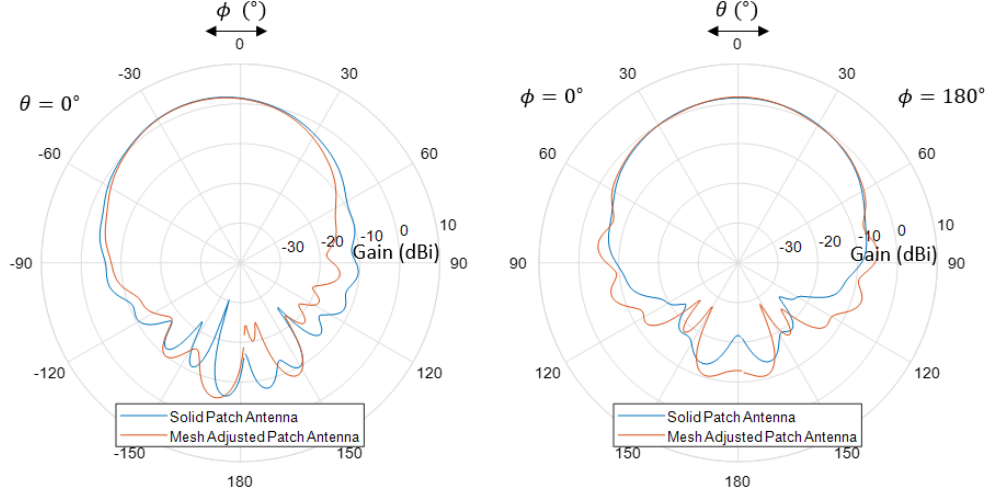


Figure 5.17: Measured antenna patterns at 2.52 GHz for both the solid and adjusted mesh patch antennas with realized gain shown. (Left) Elevation Pattern (Right) Azimuth Pattern.

Since the front-to-back ratio decreased when introducing a mesh, a full sweep is carried out to show how it degrades as more metal is taken away. This analysis is showing how effective the mesh acts as a ground plane to protect from back radiation. The FBR versus fill factor can be approximated as

$$FBR = |FBR(\Psi = 1)|(2\Psi - \Psi^2), \quad (5.18)$$

where all quantities are calculated in linear scale, then converted to dB in Fig. 5.18. The decrease FBR versus fill factor for a fixed unit cell can be characterized by the amount of conductor that remains. This effect is an interesting but predictable relationship, since as more material is taken away, the more the RF wave will leak causing the FBR to decrease as  $\Psi$  increases.

From Fig. 5.17, the antenna patterns showed a change in the azimuthal 3dB beamwidth and a miniscule change in realized gain. The relationship between the fill factor and the beamwidth and gain is shown in Figs. 5.19 and 5.20. The figures show a solid patch

Table 5.5: Antenna parameters versus fill factor.

$\Psi$	Peak Gain (dBi)	3dB Beamwidth ( $^{\circ}$ )	FBR (dB)
$\Psi = 1$	2.28	68.4	29
$\Psi = 0.5$	2.28	67.5	28
$\Psi = 0.25$	2.26	66.1	25
$\Psi = 0.18$	2.23	65.5	22
$\Psi = 0.07$	2.20	64.8	17

antenna reference to easily display the decrease in beamwidth and even smaller change in gain. In future work, a further analysis will need to be taken into account to verify if the decrease can be accounted for by better impedance matching to the antenna. The relationship between the beamwidth and fill factor could be attributed to the fact the gain remains somewhat constant, but the front to back ratio varies more with fill factor. As fill factor decreases, FBR also decreases, but the gain remains the same. This in turn causes the beamwidth to decrease as fill factor is decreased. The decrease in gain can be attributed to the increase in transmission line losses shown in the previous section.

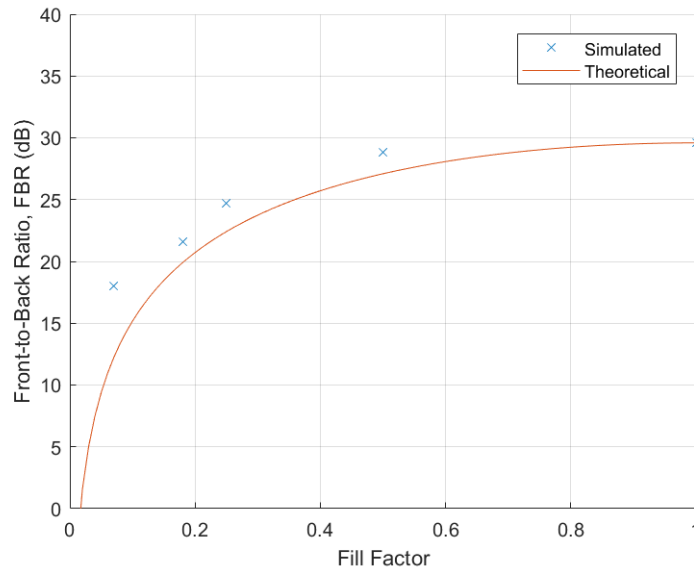


Figure 5.18: Simulated front to back ratio versus fill factor for 2.52 GHz mesh patch antenna.

From the initial analysis, the mesh has little effect on the radiation characteristics of the

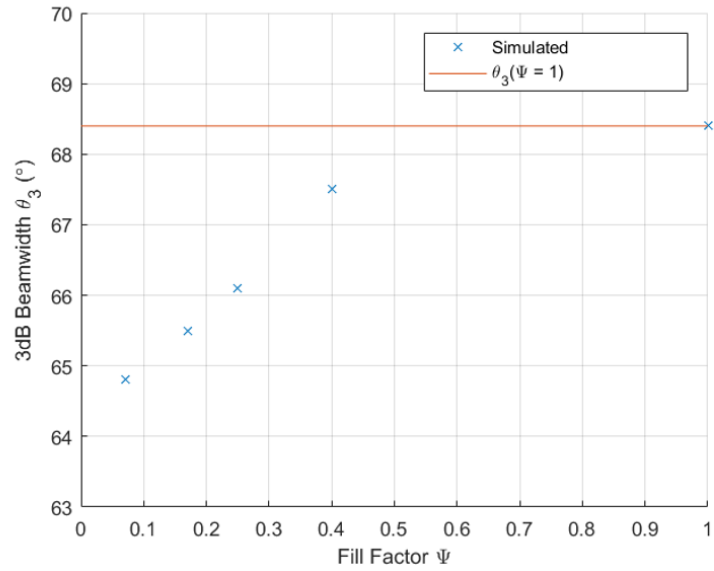


Figure 5.19: Simulated 3dB beamwidth  $\theta_3$  versus fill factor for 2.52 GHz mesh patch antenna.

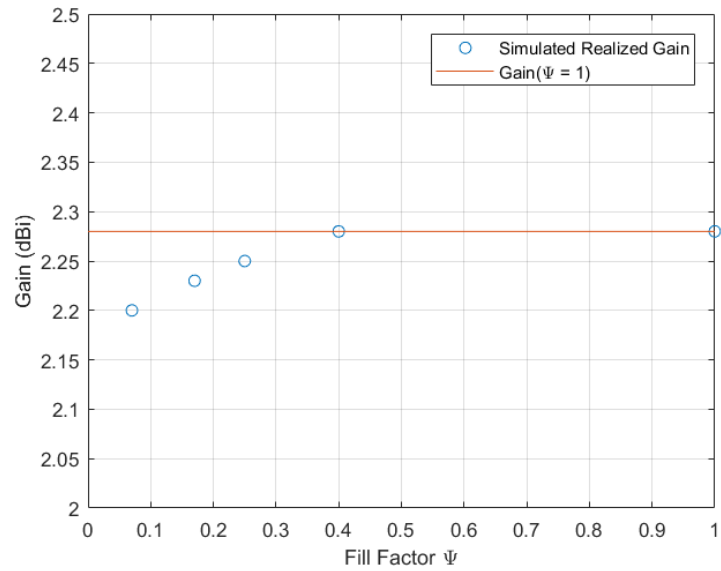


Figure 5.20: Simulated realized gain (dB) versus fill factor for 2.52 GHz mesh patch antenna.

patch antenna. Since the antenna was made with  $35\text{ }\mu\text{m}$  copper, fully reaching skin depth, the conductive losses were not evident except for the less than 0.1 dB decrease of gain and a  $3^\circ$  decrease in 3dB beamwidth due to the fact the FBR is decreasing, while the peak gain stays relatively constant. For the 0.05 fill factor antenna which would equate to a 90% transmissive mesh antenna at normal incidence the antenna performance is only decreased by 3.5% which is a marginal decrease which showed agreement with measurement and simulation. In conclusion, the fully meshed patch antenna performed on the same level as the solid patch when using a mesh which validates the antenna performance aspects of the analysis.

## 5.6 Meshed, Linear, Series Fed Patch Array

Using the analysis from the previous sections an antenna array can be simulated. A linear series fed patch array encompasses both aspects of the meshed transmission lines and the meshed patch antenna. Creating a meshed array must consider the adjusted transmission line phase length and increased impedance's inherent with the introduction of a mesh. Literature has shown that when the mesh pitch is much much less than a wavelength, the mesh structure can be considered solid [99]. The analysis in this section will set up the designs for higher frequency antennas where the behavior scales with frequency. Further studies are examining the FBR with a constant fill factor, but decreased mesh pitch, which will enhance the ground plane and radiating patch effectiveness. The linear series fed patch antenna array is commonly used in beamforming applications.

Figure 5.21 shows the initial CST model for the series fed array. Using the transmission line analysis and the results from the patch antenna make the design of this antenna simpler and more predictable. Understanding the effects, the mesh has on the transmission line phase length, impedance/RLGC parameters, and the radiation properties the antenna can be designed with ease. The series fed linear patch array is a relatively sensitive antenna due to its relationships of the phase length and stepped impedance and adding a mesh

to this design could affect the operating frequency when compared to the solid. Initial simulations show the down shift in resonance follows the behavior of both the transmission line and the patch antenna due to the increase in inductance and decrease in capacitance from the introduction of the mesh. In order to simulate the fully meshed arrays accurately, high computation is necessary especially when the mesh pitch is not sufficiently small compared to a wavelength ( $\approx \lambda/50$ ). The S-parameters and antenna pattern measurements in Figs. 5.22 and 5.23 show a meshed linear series fed array is feasible, further work will be needed to tune the antenna to account for the effects presented in this chapter including the impedance changes as well as the resonant frequency of the antenna which will be needed for a functioning RF sensing mechanism in a single aperture RF-EO/IR sensing system. The pattern and performance is similar in terms of realized gain, beamwidth. A measurement will need to be performed to validate the simulation presented. In addition, using the analysis previously introduced, tuning the array will be performed by changing the feed and patch antennas lengths, as well as adjusting the feed and patch widths. This design was shown as an introduction to future work in developing an optically transparent phased array antenna.

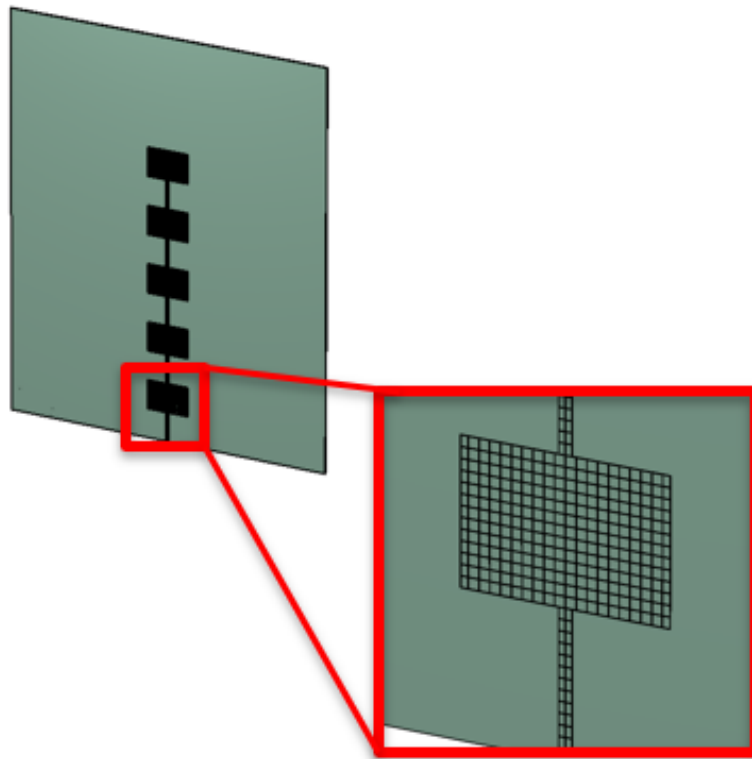


Figure 5.21: 5.8 GHz meshed linear, series fed patch array.

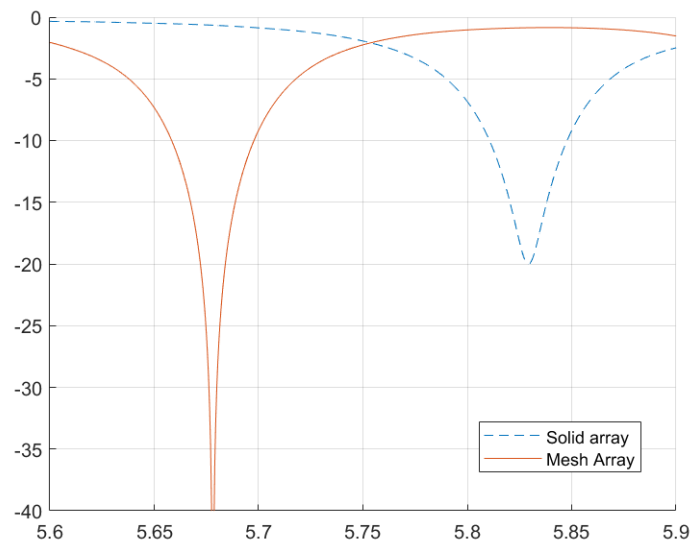


Figure 5.22: S-parameters for 5.8 GHz meshed linear, series fed patch array.



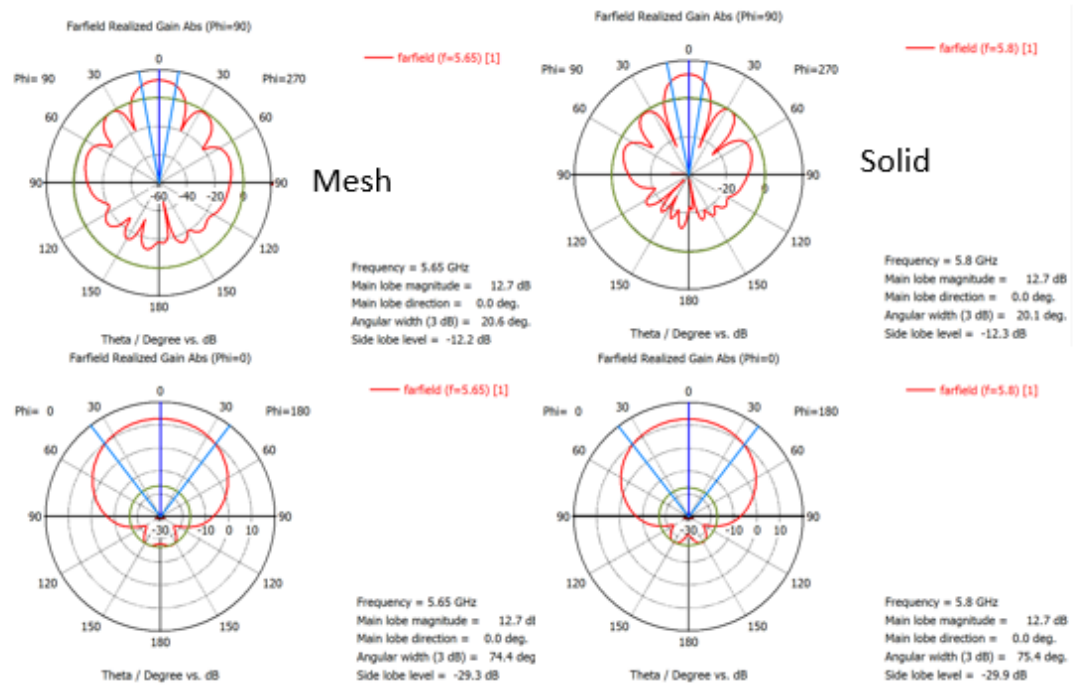


Figure 5.23: Simulated Pattern for 5.8 GHz meshed linear, series fed patch array.

## CHAPTER 6

### CONCLUSION AND FUTURE WORK

---

**Chapter Overview:** This chapter provides the following:

- Concluding remarks on the work presented in the thesis
  - Proposed future work
  - Summary of novel contributions Presented in this Work
  - List of publications resulting from the work presented in the thesis
- 

The work in this thesis presents the initial steps in achieving single aperture multi-modal sensing. The essential aspect in achieving the proposed sensing is the transparent antenna. The transparent conductor explored is a conductive mesh, as the limitations of transparent conducting oxides present challenges with high performance at RF/micro-/millimeter-waves.

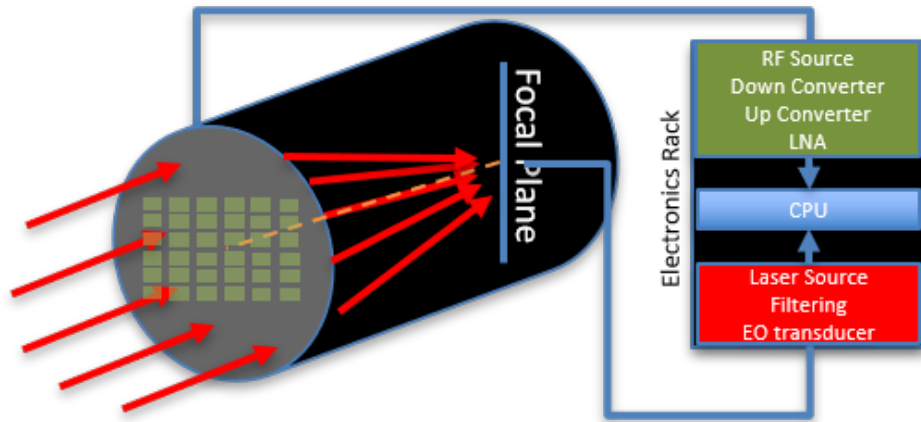


Figure 6.1: Single aperture multi-modal sensing or communications.

As RF communications and EO imaging are well developed technologies, the most pivotal technology will assist in realizing single aperture multi-modal sensing is the optically transparent antenna characterization. The end goal will be looking to place an RF antenna array over an optical aperture where the phase center of the antenna array is aligned with the optical axis of the EO system as shown in Fig. 6.1. Adding an RF sensing modality to an EO system will have trade-offs including precision of sensing versus the decrease in SWaP. For many of the applications, adding a sensing modality will drastically increase the situational awareness for the given application and provides useful sensing information.

## **6.1 Future Work**

The research allows the exploration of new areas in antenna design, remote sensing and system level design. The work lays the ground work for future problems to be solved on a system level.

### 6.1.1 Exploring Infrared Transparent Antennas

Another class of transparent antennas, that has not been documented at all in literature is IR transparent antennas. Using the mesh on a SWIR transparent substrate, an antenna can be easily realized. IR transparent substrates are less common, but there are flexible options like polymers that are available with transmittance covering SWIR from  $8\mu\text{m}$  to  $12\mu\text{m}$

### 6.1.2 Signal launch and feeding mechanisms

In microwave and millimeter wave circuits, the signal launch is often the largest source of signal losses and reflections. For a transparent antenna, methods to launch a signal and feed the antenna must be discussed. Though this is not the current focus of the research, it will need to be discussed and analyzed in future work. Millimeter wave circuits also require higher precision connectors typically 3.5 mm or 2.92 mm connectors and cable assemblies. In addition, GPPO (mini-SMP) connectors are reported to achieve high performance up to

30 GHz [124]. Other standard options like the Southwest Microwave screw-on edge mount connectors are being explored but have not yet been documented for use on glass.

#### 6.1.3 Purposely Misaligning the Top and Bottom Layer of Mesh Patch Antenna

An investigation to purposely misalign the mesh to analyze the radiation properties of a the mesh. Though, the misaligned mesh will slightly degrade the transmittance the RF performance could potentially be enhance due to the current density and how wave propagate though the meshed antenna. The misalignment could positively affect the front to back ratio by altering the ground plane that the resonant wave interacts with.

#### 6.1.4 Optically Transparent Array Layout

Many of today's active electronic scanned array (AESA) antennas have each antenna element fed separately to allow active beam steering capabilities. As a result, many of the antennas are fed directly with the electronics on the backside of the aperture. This topology minimizes losses and allows space to be conserved in many of the state-of-the-art AESA's and adaptive beamformers. For an optically transparent aperture, the standard probe or aperture feeding mechanisms will not suffice as the optical transmittance will be sacrificed. As a result, a study to feed the antenna elements from the edge of the aperture will be performed. This is part of future work, and results will not be presented in this thesis.

#### 6.1.5 Array Front-to-Back Ratio Measurement

For a realized RF/EO multimodal system, further analysis of the front-to-back ratio of a transparent antenna will be necessary. For many EO systems there is a limitation on the power that can be incident on the focal plane array. Since backlobes are inherent on every antenna element and are further exaggerated for a transparent antenna, this specification will create a limit on the input power to the RF antenna aperture. Based on the initial analysis presented in the previous chapter, the *FBR* can be somewhat predicted based on

the solid design and the fill factor, but will need to be verified on the full system to calculate the maximum power limitations of the system.

#### 6.1.6 Array Fabrication and Test

Once the initial single element antenna characterization is carried out, the 24 GHz antenna array will be fabricated and measured. The optical tests will be testing imaging quality through the lens with a range of optical wavelength. The antenna array will undergo standard antenna tests to verify operation and power handling capabilities.

#### 6.1.7 Multi-modal Sensing System Construction

The transparent antenna array has potential for a variety of novel applications. Combining the antenna array on the aperture of an EO/IR system has the potential for new science to emerge by combining the data collected from both the RF aperture and the EO/IR aperture. Using a variety of techniques used currently combining visible and infrared waves for classification, specifically vegetative classification using normalized difference vegetation index (NDVI). Extending the classification to RF and EO/IR platform will have challenges with the large difference in frequency, but could have great impact for the future of sensing in self-driving cars. Providing a low SWaP/cost (SWaP-C) system with the ability to target and classify objects based on their RF/IR returns would be crucial in the development for level five autonomy (full vehicle automation where the driverless car can operate on any road and in any condition).

#### 6.1.8 RF-EO/IR Single Aperture Sensor Fusion

Single aperture sensor fusion has many applications within automotive, satellite, and defense industries. RF-EO/IR sensor fusion can be performed by taking the reflectivity of a material or structure at RF and at EO/IR wavelengths for precise object classification based on the materials transmissive, reflective, and absorptive properties, as explained in Chapter

3 of this thesis, are directly related to the material properties at the separate wavelengths.

## 6.2 Contributions

The thesis has presented novel contributions that have added to the discussion of optically transparent conductors and optically transparent antennas in literature. The following is a summary of the novel contributions presented in the thesis.

- Survey of transparent conductors and transparent antennas - A literature survey was conducted to investigate transparent conductors that can and have been used for transparent antennas. Using the data of transparent conductors and transparent antennas, trends displaying the relationship between conductivity and transmittance. The data analysis allows one to find the material that will work best for the desired application maximizing both conductivity and transmittance.
- Proposed figure of merit for optically transparent RF conductors - A figure of merit is proposed to include a frequency dependence with skin depth on the previous figure of merit for transparent conductors. This figure of merit is its skin depth at the desired operating frequency.
- Electromagnetic properties of transparent conductors - An explanation of optically transparent conductors carried out based on classical electromagnetics analysis using the variation of the electric susceptibility over wavelength as the fundamental basis for transparent conductors which can be modelling using the Drude free-electron model which describes metals with a plasma frequency where it transitions from reflected to transmitting electromagnetic waves.
- Optical Comparison of Mesh and Transparent Conducting Oxide - Transmittance measurements from UV (200 nm) to Near Infrared (3200 nm) were taken of both a transparent conducting oxide (Indium Tin Oxide) and a 90% transmissive mesh showing

the differences in performance. These measurements were related back to the performance on imaging, evaluated by the degradation of the point-spread-function when covering an optical aperture.

- RF characterization of meshed transmission lines - Evaluation of the effect of a mesh conductor for microstrip transmission lines was conducted. The analysis gave a full understanding of the effects of using a meshed transmission line, including the impedance, phase, loss. Using the classical evaluation of the RLGC lumped element model the study presented a relationship between the mesh geometry and the inductance/capacitance per unit length.
- Characterization of meshed patch antennas - Patch antennas were analyzed observing the mesh effect on resonant frequency, gain, and front-to-back ratio. The work was presented at 2.4 GHz, with future implementations at 24 GHz.

### **6.3 Publications and Presentations**

The research in this thesis has been submitted to or is in preparation to be submitted to peer-reviewed conference proceedings, journals, and poster presentations. The following publications are subsets and focused articles of the work presented in this thesis.

#### 6.3.1 Peer Reviewed Journal Articles

- Z. J. Silva, C. R. Valenta, and G. D. Durgin, “Optically transparent antennas: Transparent RF conductors,” IEEE Antennas and Propagation Magazine, 2019 (Under Review).
- Z. J. Silva, C. R. Valenta, and G. D. Durgin, “Meshed Microstrip Transmission Lines,” Transactions on Microwave Theory and Techniques IMS Special Edition 2019 (In Preparation).

- Z. J. Silva, C. R. Valenta, and G. D. Durgin, “Meshed Patch Antennas,” Transactions on Antennas and Propagation 2019 (In Preparation).
- Z. J. Silva, G. P. Badura, C. R. Valenta, and G. D. Durgin, “Imaging Through Optically Transparent Conductors,” OSA Optics Express (In Preparation).

### 6.3.2 Refereed Conference Proceedings and Presentations

- Z. J. Silva, C. R. Valenta, and G. D. Durgin, “Design and characterization of meshed microstrip transmission lines,” IEEE International Microwave Symposium, 2019 (Accepted).
- Z. J. Silva, C. P. Hunter, C. R. Valenta, and G. D. Durgin, “2.5 GHz meshed inset-fed patch antenna,” IEEE International Symposium on Antennas and Propagation, 2019 (Accepted).

### 6.3.3 Poster Presentations

- *Meshed Transmission Lines: Towards Optically Transparent Antennas*
  - IEEE RFID Conference (Poster) - Orlando, FL  
(April 10-12, 2018)
- *Transparent Antennas for Multi-Modal Remote Sensing*
  - Symposium on Space Innovations (Poster) - Atlanta, GA  
(November 13-14, 2018)



## REFERENCES

- [1] A. W. Wright, “Art. vii.—on the production of transparent metallic films by the electrical discharge in exhausted tubes,” *American Journal of Science and Arts (1820-1879)*, vol. 13, no. 73, p. 49, 1877.
- [2] K. Baedeker, “Electrical conductivity and thermo-electromotive force of some metallic compounds,” *Annalen der Physik*, vol. 327, no. 4, pp. 749–766, 1907.
- [3] J. Preston, “Constitution and mechanism of the selenium rectifier photocell,” *Proc. R. Soc. Lond. A*, vol. 202, no. 1071, pp. 449–466, 1950.
- [4] H. A. McMaster, *Conductive coating for glass and method of application*, US Patent 2,429,420, 1947.
- [5] C. M. Lampert, “Heat mirror coatings for energy conserving windows,” *Solar Energy Materials*, vol. 6, no. 1, pp. 1–41, 1981.
- [6] Y. Kim, C. Lee, S. Hong, C. W. Jung, and Y. Kim, “Design of transparent multilayer film antenna for wireless communication,” *Electronics Letters*, vol. 51, no. 1, pp. 12–14, 2014.
- [7] S. Hong, Y. Kim, and C. W. Jung, “Transparent microstrip patch antennas with multilayer and metal-mesh films,” *IEEE Antennas and Wireless Propagation Letters*, vol. 16, pp. 772–775, 2017.
- [8] D. S. Ginley, H. Hosono, and D. C. Paine, in *Handbook of transparent conductors*, Springer, 2010.
- [9] S. Ye, A. R. Rathmell, Z. Chen, I. E. Stewart, and B. J. Wiley, “Metal nanowire networks: The next generation of transparent conductors,” *Advanced Materials*, vol. 26, no. 39, pp. 6670–6687, 2014.
- [10] J. Lombardi, R. Malay, J. Schaffner, H. J. Song, M.-H. Huang, S. Pollard, M. Poliks, and T. Talty, “Copper transparent antennas on flexible glass by subtractive and semi-additive fabrication for automotive applications,” in *2018 IEEE 68th Electronic Components and Technology Conference (ECTC)*, IEEE, 2018, pp. 2107–2115.
- [11] F. Castanedo, “A review of data fusion techniques,” *The Scientific World Journal*, vol. 2013, 2013.

- [12] Z. J. Silva, C. R. Valenta, and G. D. Durgin, "Optically transparent antennas: Transparent rf conductors," *IEEE Antennas and Propagation Magazine*, 2019, (Under Review).
- [13] G Haacke, "New figure of merit for transparent conductors," *Journal of Applied Physics*, vol. 47, no. 9, pp. 4086–4089, 1976.
- [14] P.-C. Yu, C.-C. Hong, and T.-M. Liou, "Bendable transparent conductive meshes based on multi-layer inkjet-printed silver patterns," *Journal of Micromechanics and Microengineering*, vol. 26, no. 3, p. 035 012, 2016.
- [15] M. Malek, S Hakimi, S. A. Rahim, and A. Evizal, "Dual-band cpw-fed transparent antenna for active rfid tags," *IEEE Antennas and Wireless Propagation Letters*, vol. 14, pp. 919–922, 2015.
- [16] J. Han, S. Yuan, L. Liu, X. Qiu, H. Gong, X. Yang, C. Li, Y. Hao, and B. Cao, "Fully indium-free flexible ag nanowires/zno: F composite transparent conductive electrodes with high haze," *Journal of Materials Chemistry A*, vol. 3, no. 10, pp. 5375–5384, 2015.
- [17] J. Zhang, "Multi-source remote sensing data fusion: Status and trends," *International Journal of Image and Data Fusion*, vol. 1, no. 1, pp. 5–24, 2010.
- [18] S. Bae, H. Kim, Y. Lee, X. Xu, J.-S. Park, Y. Zheng, J. Balakrishnan, T. Lei, H. R. Kim, Y. I. Song, *et al.*, "Roll-to-roll production of 30-inch graphene films for transparent electrodes," *Nature nanotechnology*, vol. 5, no. 8, p. 574, 2010.
- [19] R. G. Gordon, "Criteria for choosing transparent conductors," *MRS bulletin*, vol. 25, no. 8, pp. 52–57, 2000.
- [20] S. Ghosh, A. Mallick, A. Koley, P. Chaudhury, S. Garner, and D. Basak, "Study on azo coated flexible glass as tco substrate," in *Photovoltaic Specialist Conference (PVSC), 2017 IEEE 44th*, IEEE, 2017, pp. 1–5.
- [21] N.-F. Shih, J.-Z. Chen, and Y.-L. Jiang, "Properties and analysis of transparency conducting azo films by using dc power and rf power simultaneous magnetron sputtering," *Advances in Materials Science and Engineering*, vol. 2013, 2013.
- [22] C. Tong, J. Yun, Y.-J. Chen, D. Ji, Q. Gan, and W. A. Anderson, "Thermally diffused al: ZnO thin films for broadband transparent conductor," *ACS applied materials & interfaces*, vol. 8, no. 6, pp. 3985–3991, 2016.
- [23] H. Hagendorfer, K. Lienau, S. Nishiwaki, C. M. Fella, L. Kranz, A. R. Uhl, D. Jaeger, L. Luo, C. Gretener, S. Buecheler, *et al.*, "Highly transparent and conduc-

tive znO: Al thin films from a low temperature aqueous solution approach,” *Advanced Materials*, vol. 26, no. 4, pp. 632–636, 2014.

- [24] J. W. Jo, J. W. Jung, J. U. Lee, and W. H. Jo, “Fabrication of highly conductive and transparent thin films from single-walled carbon nanotubes using a new non-ionic surfactant via spin coating,” *Acs Nano*, vol. 4, no. 9, pp. 5382–5388, 2010.
- [25] J. Zhang, L. Gao, J. Sun, Y. Liu, Y. Wang, J. Wang, H. Kajiura, Y. Li, and K. Noda, “Dispersion of single-walled carbon nanotubes by nafion in water/ethanol for preparing transparent conducting films,” *The Journal of Physical Chemistry C*, vol. 112, no. 42, pp. 16 370–16 376, 2008.
- [26] N. Ferrer-Anglada, J. Pérez-Puigdemont, J. Figueras, M. Z. Iqbal, and S. Roth, “Flexible, transparent electrodes using carbon nanotubes,” *Nanoscale research letters*, vol. 7, no. 1, p. 571, 2012.
- [27] M. W. Rowell, M. A. Topinka, M. D. McGehee, H.-J. Prall, G. Dennler, N. S. Sariciftci, L. Hu, and G. Gruner, “Organic solar cells with carbon nanotube network electrodes,” *Applied Physics Letters*, vol. 88, no. 23, p. 233 506, 2006.
- [28] W. Aloui, A. Ltaief, and A. Bouazizi, “Transparent and conductive multi walled carbon nanotubes flexible electrodes for optoelectronic applications,” *Superlattices and Microstructures*, vol. 64, pp. 581–589, 2013.
- [29] K. Ellmer, “Past achievements and future challenges in the development of optically transparent electrodes,” *Nature Photonics*, vol. 6, no. 12, p. 809, 2012.
- [30] B. N. Chandrashekar, B. Deng, A. S. Smitha, Y. Chen, C. Tan, H. Zhang, H. Peng, and Z. Liu, “Roll-to-roll green transfer of cvd graphene onto plastic for a transparent and flexible triboelectric nanogenerator,” *Advanced Materials*, vol. 27, no. 35, pp. 5210–5216, 2015.
- [31] C. Cai, F. Jia, A. Li, F. Huang, Z. Xu, L. Qiu, Y. Chen, G. Fei, and M. Wang, “Crackless transfer of large-area graphene films for superior-performance transparent electrodes,” *Carbon*, vol. 98, pp. 457–462, 2016.
- [32] C.-M. Gee, C.-C. Tseng, F.-Y. Wu, H.-P. Chang, L.-J. Li, Y.-P. Hsieh, C.-T. Lin, and J.-C. Chen, “Flexible transparent electrodes made of electrochemically exfoliated graphene sheets from low-cost graphite pieces,” *Displays*, vol. 34, no. 4, pp. 315–319, 2013.
- [33] J. Burst, W. Rance, D. Meysing, C. Wolden, W. Metzger, S. Garner, P Cimo, T. Barnes, T. Gessert, and M. Reese, “Performance of transparent conductors on flexible glass and plastic substrates for thin film photovoltaics,” in *Photovoltaic Specialist Conference (PVSC), 2014 IEEE 40th*, IEEE, 2014, pp. 1589–1592.

- [34] F. Colombel, X. Castel, M. Himdi, G. Legeay, S. Vigneron, and E. M. Cruz, "Ultrathin metal layer, ito film and ito/cu/ito multilayer towards transparent antenna," *IET science, measurement & technology*, vol. 3, no. 3, pp. 229–234, 2009.
- [35] M. D. Poliks, Y.-L. Sung, J. Lombardi, R. Malay, J. Dederick, C. Westgate, M.-H. Huang, S. Garner, S. Pollard, and C. Daly, "Transparent antennas for wireless systems based on patterned indium tin oxide and flexible glass," in *Electronic Components and Technology Conference (ECTC), 2017 IEEE 67th*, IEEE, 2017, pp. 1443–1448.
- [36] S. H. Kang and C. W. Jung, "Transparent patch antenna using metal mesh," *IEEE Transactions on Antennas and Propagation*, vol. 66, no. 4, pp. 2095–2100, 2018.
- [37] J. Hautcoeur, F. Colombel, X. Castel, M. Himdi, and E. M. Cruz, "Radiofrequency performances of transparent ultra-wideband antennas," *Progress In Electromagnetics Research C*, vol. 22, pp. 259–271, 2011.
- [38] J. Hautcoeur, F. Colombel, X. Castel, M. Himdi, and E. M. Cruz, "Optically transparent monopole antenna with high radiation efficiency manufactured with silver grid layer (aggl)," *Electronics Letters*, vol. 45, no. 20, pp. 1014–1016, 2009.
- [39] A. Martin, X. Castel, M. Himdi, and O. Lafond, "Mesh parameters influence on transparent and active antennas performance at microwaves," *AIP Advances*, vol. 7, no. 8, p. 085 120, 2017.
- [40] Y. G. Moon, J. B. Koo, N.-M. Park, J.-Y. Oh, B. S. Na, S. S. Lee, S.-D. Ahn, and C. W. Park, "Freely deformable liquid metal grids as stretchable and transparent electrodes," *IEEE Transactions on Electron Devices*, vol. 64, no. 12, pp. 5157–5162, 2017.
- [41] J. Hautcoeur, L. Talbi, K. Hettak, and M. Nedil, "60 ghz optically transparent microstrip antenna made of meshed augl material," *IET Microwaves, Antennas & Propagation*, vol. 8, no. 13, pp. 1091–1096, 2014.
- [42] H. Sharifi, H. J. Song, M. Yajima, K. Kona, A. Bekaryan, K. Geary, and I. Bilik, "Semi-transparent and conformal antenna technology for millimeter-wave intelligent sensing," in *2018 IEEE MTT-S International Conference on Microwaves for Intelligent Mobility (ICMIM)*, IEEE, 2018, pp. 1–4.
- [43] H. Inaba, M. Shinnai, K. Nishikawa, T. Saitoh, and T. Tsukada, *Vehicle window glass antenna using transparent conductive film*, US Patent 4,849,766, 1989.
- [44] K Ito and M Wu, "See-through microstrip antennas constructed on a transparent substrate," in *Antennas and Propagation, 1991. ICAP 91., Seventh International Conference on (IEE)*, IET, 1991, pp. 133–136.

- [45] L. L. Nagy, F. T. Shum, and J. L. Funke, *Transparent film antenna for a vehicle window*, US Patent 5,083,135, 1992.
- [46] M. Mandell, P. Stannard, and I Katz, "Nascap programmer's reference manual," *NASA Rep. SSS-84-6638, S-Cubed*, 1993.
- [47] E. K. Walton, H. S. Koontz, and R. D. Moran, *Transparent window antenna*, US Patent 5,355,144, 1994.
- [48] R. N. Simons and R. Q. Lee, "Feasibility study of optically transparent microstrip patch antenna," 1997.
- [49] H. Lindenmeier, J. Hopf, and L. Reiter, *Windowpane antenna with transparent conductive layer*, US Patent 5,926,141, 1999.
- [50] R. Simons and R. Q. Lee, *Optically transparent microstrip patch and slot antennas*, US Patent 5,872,542, 1999.
- [51] M.-S. Wu and K. Ito, "Basic study on see-through microstrip antennas constructed on a window glass," in *Antennas and Propagation Society International Symposium, 1992. AP-S. 1992 Digest. Held in Conjunction with: URSI Radio Science Meeting and Nuclear EMP Meeting., IEEE*, IEEE, 1992, pp. 499–502.
- [52] N Outaleb, J Pinel, M Drissi, and O Bonnaud, "Microwave planar antenna with rf-sputtered indium tin oxide films," *Microwave and Optical Technology Letters*, vol. 24, no. 1, pp. 3–7, 2000.
- [53] M. J. Lynch, *Optically transparent phase array antenna*, US Patent 6,388,621, 2002.
- [54] M. Zamudio, T Busani, Y Tawk, J Costantine, and C Christodoulou, "Design of azo film for optically transparent antennas," in *Antennas and Propagation (APSURSI), 2016 IEEE International Symposium on*, IEEE, 2016, pp. 127–128.
- [55] A. Desai, T. Upadhyaya, and R. Patel, "Compact wideband transparent antenna for 5g communication systems," *Microwave and Optical Technology Letters*, 2017.
- [56] A Katsounaros, Y Hao, N Collings, and W. Crossland, "Optically transparent antenna for ultra wide-band applications," in *Antennas and Propagation, 2009. Eu-CAP 2009. 3rd European Conference on*, IEEE, 2009, pp. 1918–1921.
- [57] T Peter, T. Yuk, R Nilavalan, and S. Cheung, "A novel technique to improve gain in transparent uwb antennas," in *LAPC 2011-2011 Loughborough Antennas and Propagation Conference*, 2011.

- [58] M. Roo-Ons, S. Shynu, M. Ammann, S. McCormack, and B. Norton, "Transparent patch antenna on a-si thin-film glass solar module," *Electronics letters*, vol. 47, no. 2, pp. 85–86, 2011.
- [59] H. J. Song, "Challenges in glass integrated optically transparent antennas," in *International Symposium on Antennas and Propagation (ISAP)*, 2011.
- [60] A. Azini, M. Kamarudin, T. Rahman, S. Rahim, and M. Rani, "Transparent antenna design for wireless access point application," *Session 3A8*, p. 532, 2013.
- [61] M. Rani, S. K. A. Rahim, M. R. Kamarudin, T. Peter, S. Cheung, and B. Saad, "Electromagnetic behaviors of thin film cpw-fed csrr loaded on uwb transparent antenna," *IEEE Antennas and Wireless Propagation Letters*, vol. 13, pp. 1239–1242, 2014.
- [62] A. Desai and T. Upadhyaya, "Transparent dual band antenna with  $\mu$ -negative material loading for smart devices," *Microwave and Optical Technology Letters*, vol. 60, no. 11, pp. 2805–2811, 2018.
- [63] S. Hakimi, S. K. A. Rahim, M. Abedian, S. Noghabaei, and M. Khalily, "Cpw-fed transparent antenna for extended ultrawideband applications," *IEEE Antennas and Wireless Propagation Letters*, vol. 13, pp. 1251–1254, 2014.
- [64] Y. Yao, W. Chen, X. Chen, and J. Yu, "Design of optically transparent antenna with directional radiation patterns," *International Journal of Antennas and Propagation*, vol. 2017, 2017.
- [65] Y. Koga and M. Kai, "A transparent double folded loop antenna for iot applications," in *2018 IEEE-APS Topical Conference on Antennas and Propagation in Wireless Communications (APWC)*, IEEE, 2018, pp. 762–765.
- [66] G. Sun, B. Muneer, and Q. Zhu, "A study of microstrip antenna made of transparent ito films," in *Antennas and Propagation Society International Symposium (APSURSI), 2014 IEEE*, IEEE, 2014, pp. 1867–1868.
- [67] T. Yasin, R. Baktur, and C. Furse, "A study on the efficiency of transparent patch antennas designed from conductive oxide films," in *2011 IEEE International Symposium on Antennas and Propagation (APSURSI)*, 2011.
- [68] B. S. Kim, K.-Y. Shin, J. B. Pyo, J. Lee, J. G. Son, S.-S. Lee, and J. H. Park, "Reversibly stretchable, optically transparent radio-frequency antennas based on wavy ag nanowire networks," *ACS applied materials & interfaces*, vol. 8, no. 4, pp. 2582–2590, 2016.

- [69] T. Sannicolo, M. Lagrange, A. Cabos, C. Celle, J.-P. Simonato, and D. Bellet, "Metallic nanowire-based transparent electrodes for next generation flexible devices: A review," *Small*, vol. 12, no. 44, pp. 6052–6075, 2016.
- [70] M. A. Maged, F. Elhefnawi, H. M. Akah, and H. M. El-Hennawy, "C-band transparent antenna design for intersatellites communication," *International Journal of Scientific and Engineering Research*, vol. 12, no. 7, 2018.
- [71] S. Sheikh, M. Shokooh-Saremi, and M.-M. Bagheri-Mohagheghi, "Transparent microstrip antenna made of fluorine doped tin oxide: A comprehensive study," *Journal of Electromagnetic waves and Applications*, vol. 29, no. 12, pp. 1557–1569, 2015.
- [72] M. Grande, G. V. Bianco, D. Laneve, P. Capezzuto, V. Petruzzelli, M. Scalora, F. Prudeniano, G. Bruno, and A. D'Orazio, "Optically transparent wideband cvd graphene-based microwave antennas," *Applied Physics Letters*, vol. 112, no. 25, p. 251 103, 2018.
- [73] S. Kosuga, K. Suga, R. Suga, T. Watanabe, O. Hashimoto, and S. Koh, "Radiation properties of graphene-based optically transparent dipole antenna," *Microwave and Optical Technology Letters*, vol. 60, no. 12, pp. 2992–2998, 2018.
- [74] J. Wang, Y. Guan, H. Yu, N. Li, S. Wang, C. Shen, Z. Dai, D. Gan, R. Yang, S. He, *et al.*, "Transparent graphene microstrip filters for wireless communications," *Journal of Physics D: Applied Physics*, vol. 50, no. 34, 34LT01, 2017.
- [75] B.-D. Yang, J.-M. Oh, H.-J. Kang, S.-H. Park, C.-S. Hwang, M. K. Ryu, and J.-E. Pi, "A transparent logic circuit for rfid tag in a-igzo tft technology," *ETRI Journal*, vol. 35, no. 4, pp. 610–616, 2013.
- [76] H. R. Khaleel, H. M. Al-Rizzo, and A. I. Abbosh, "Design, fabrication, and testing of flexible antennas," in *Advancement in Microstrip Antennas With Recent Applications*, InTech, 2013.
- [77] N. J. Kirsch, N. A. Vacirca, E. E. Plowman, T. P. Kurzweg, A. K. Fontecchio, and K. R. Dandekar, "Optically transparent conductive polymer rfid meandering dipole antenna," in *RFID, 2009 IEEE International Conference on*, IEEE, 2009, pp. 278–282.
- [78] T. Yasin and R. Baktur, "Inkjet printed patch antennas on transparent substrates," in *Antennas and Propagation Society International Symposium (APSURSI), 2010 IEEE*, IEEE, 2010, pp. 1–4.
- [79] J. A. Arellano, "Inkjet-printed highly transparent solar cell antennas," Master's thesis, Utah State University, 2011.

- [80] R. Montaña, N. Neveu, S. Palacio, E. Martinez, D. R. Jackson, J. Chen, P. W. Fink, and R. S. Provence, "Development of low-profile antennas for cubesats," 2014.
- [81] X. Liu, D. R. Jackson, J. Chen, J. Liu, P. W. Fink, G. Y. Lin, and N. Neveu, "Transparent and nontransparent microstrip antennas on a cubesat: Novel low-profile antennas for cubesats improve mission reliability.," *IEEE Antennas and Propagation Magazine*, vol. 59, no. 2, pp. 59–68, 2017.
- [82] M. M. Rabie, H. El-Henawy, F. El-Hefnawy, and F. Ibrahim, "Meshed conductor and meshed substrate gps l1 band microstrip antenna for cubesat applications," in *2018 35th National Radio Science Conference (NRSC)*, IEEE, 2018, pp. 55–62.
- [83] S. Y. Lee, D. Choi, Y. Youn, and W. Hong, "Electrical characterization of highly efficient, optically transparent nanometers-thick unit cells for antenna-on-display applications," in *2018 IEEE/MTT-S International Microwave Symposium-IMS*, IEEE, 2018, pp. 1043–1045.
- [84] M. Kashanianfard and K. Sarabandi, "Metamaterial inspired optically transparent band-selective ground planes for antenna applications," *IEEE Transactions on Antennas and Propagation*, vol. 61, no. 9, pp. 4624–4631, 2013.
- [85] M. Lange, *High-efficiency transparent microwave antennas*, US Patent 6,933,891, 2005.
- [86] T. W. Turpin and R. Baktur, "Meshed patch antennas integrated on solar cells," *IEEE Antennas and Wireless Propagation Letters*, vol. 8, pp. 693–696, 2009.
- [87] J. R. Saberlin, C. Furse, T. Yasin, and R. Baktur, "Passive feed methods for meshed antennas," in *Antennas and Propagation Society International Symposium (AP-SURSI), 2010 IEEE*, IEEE, 2010, pp. 1–4.
- [88] J. R. Saberlin and C. Furse, "Challenges with optically transparent patch antennas," *IEEE Antennas and Propagation Magazine*, vol. 54, no. 3, pp. 10–16, 2012.
- [89] T. Yasin and R. Baktur, "Circularly polarized meshed patch antenna for small satellite application," *IEEE Antennas and Wireless Propagation Letters*, vol. 12, pp. 1057–1060, 2013.
- [90] C. G. Ryan and G. V. Eleftheriades, "Single-and dual-band transparent circularly polarized patch antennas with metamaterial loading," *IEEE Antennas and Wireless Propagation Letters*, vol. 14, pp. 470–473, 2015.
- [91] S. Sheikh, "Circularly polarized meshed patch antenna," *IEEE Antennas and Wireless Propagation Letters*, vol. 15, pp. 352–355, 2016.



- [92] O. Yurduseven, D. Smith, N. Pearsall, I. Forbes, and D. Johnston, "A meshed multi-band solar patch array antenna," in *Antennas and Propagation Conference (LAPC), 2012 Loughborough*, IEEE, 2012, pp. 1–5.
- [93] Z. J. Silva, C. R. Valenta, and G. D. Durgin, "Design and characterization of meshed microstrip transmission lines," in *IEEE International Microwave Symposium*, (Submitted for publication), 2019.
- [94] Z. J. Silva, C. P. Hunter, C. R. Valenta, and G. D. Durgin, "2.5 ghz meshed inset-fed patch antenna," in *IEEE International Symposium on Antennas and Propagation*, (Submitted for publication), 2019.
- [95] T. Yasin, R. Baktur, and C. Furse, "A comparative study on two types of transparent patch antennas," in *General Assembly and Scientific Symposium, 2011 URSI*, IEEE, 2011, pp. 1–4.
- [96] M. R. Haraty, M. Naser-Moghadasi, A. A. Lotfi-Neyestanak, and A. Nikfarjam, "Improving the efficiency of transparent antenna using gold nanolayer deposition," *IEEE Antennas and Wireless Propagation Letters*, vol. 15, pp. 4–7, 2016.
- [97] H. J. Song, T. Y. Hsu, D. F. Sievenpiper, T. J. Talty, and H.-p. Hsu, *Method for improving the efficiency of transparent thin film antennas and antennas made by such method*, US Patent 7,427,961, 2008.
- [98] H. J. Song, T. Y. Hsu, D. F. Sievenpiper, H. P. Hsu, J. Schaffner, and E. Yasan, "A method for improving the efficiency of transparent film antennas," *IEEE Antennas and Wireless Propagation Letters*, vol. 7, pp. 753–756, 2008.
- [99] J. Hautcoeur, L. Talbi, and K. Hettak, "Feasibility study of optically transparent cpw-fed monopole antenna at 60-ghz ism bands," *IEEE Transactions on Antennas and Propagation*, vol. 61, no. 4, pp. 1651–1657, 2013.
- [100] J. R. Saberlin and C. Furse, "Challenges with optically transparent patch antennas for small satellites," in *Antennas and Propagation Society International Symposium (APSURSI), 2010 IEEE*, IEEE, 2010, pp. 1–4.
- [101] F. Harrysson and J. Medbo, *Combined display and antenna arrangement*, US Patent 8,213,757, 2012.
- [102] H. K. Pan, A. Takagi, B. Horine, and H. G. Skinner, *Communication device and display incorporating antennas between display pixels*, US Patent 9,553,352, 2017.
- [103] T. Ishibashi, S. Okumura, Y. Matsui, Y. Yamaoka, T. Takagi, H. Muko, and R. Omote, *Transparent antenna for display, translucent member for display with an antenna and housing component with an antenna*, US Patent 7,847,753, 2010.

- [104] S. Hong, S. H. Kang, Y. Kim, and C. W. Jung, “Transparent and flexible antenna for wearable glasses applications,” *IEEE Transactions on Antennas and Propagation*, vol. 64, no. 7, pp. 2797–2804, 2016.
- [105] C. A. Balanis, *Advanced engineering electromagnetics*. John Wiley & Sons, 1999.
- [106] D. M. Pozar, *Microwave engineering*. John Wiley & Sons, 2009.
- [107] E. Hecht *et al.*, *Optics*. Reading, Mass.: Addison-Wesley, 2002.
- [108] M. Born and E. Wolf, *Principles of optics: electromagnetic theory of propagation, interference and diffraction of light*. Elsevier, 2013.
- [109] G. S. Smith, *An introduction to classical electromagnetic radiation*. Cambridge University Press, 1997.
- [110] J. Snoek, “Dispersion and absorption in magnetic ferrites at frequencies above one mc/s,” *Physica*, vol. 14, no. 4, pp. 207–217, 1948.
- [111] *Dielectric spectroscopy*, <https://web.archive.org/web/20060118002845/http://www.psrc.usm.edu/mauritz/dilect.html>, Accessed: 2019-04-1.
- [112] P. Drude, “Zur elektronentheorie der metalle; ii. teil. galvanomagnetische und thermomagnetische effecte,” *Annalen der Physik*, vol. 308, no. 11, pp. 369–402, 1900.
- [113] R. E. Hummel, in *Electronic Properties of Materials*, Springer, 2011, pp. 197–206.
- [114] H. Fan, “Infra-red absorption in semiconductors,” *Reports on Progress in Physics*, vol. 19, no. 1, p. 107, 1956.
- [115] E Hagen and H Rubens, “Über beziehungen des reflexions-und emissionsvermögens der metalle zu ihrem elektrischen leitvermögen,” *Annalen der Physik*, vol. 316, no. 8, pp. 873–901, 1903.
- [116] *Emiclar ito film*, <http://www.opticalfiltersusa.com/emiclar-ito-film.html>, Accessed: 2019-03-17.
- [117] P. A. Ade, G. Pisano, C. Tucker, and S. Weaver, “A review of metal mesh filters,” in *Millimeter and Submillimeter Detectors and Instrumentation for Astronomy III*, International Society for Optics and Photonics, vol. 6275, 2006, 62750U.
- [118] R. D. Fiete and B. D. Paul, “Modeling the optical transfer function in the imaging chain,” *Optical Engineering*, vol. 53, no. 8, p. 083 103, 2014.

- [119] J. K. Roland, “A study of slanted-edge mtf stability and repeatability,” in *Image Quality and System Performance XII*, International Society for Optics and Photonics, vol. 9396, 2015, p. 93960L.
- [120] P. D. Burns *et al.*, “Slanted-edge mtf for digital camera and scanner analysis.”
- [121] K. Masaoka, T. Yamashita, Y. Nishida, and M. Sugawara, “Modified slanted-edge method and multidirectional modulation transfer function estimation,” *Optics express*, vol. 22, no. 5, pp. 6040–6046, 2014.
- [122] I. J. Bahl, “A designer’s guide to microstrip line,” *Microwaves*, pp. 1–380, 1977.
- [123] M. Degerstrom, B. Gilbert, and E. Daniel, “Accurate resistance, inductance, capacitance, and conductance (rlcg) from uniform transmission line measurements,” in *2008 IEEE-EPEP Electrical Performance of Electronic Packaging*, IEEE, 2008, pp. 77–80.
- [124] *Corning microwave connectivity*, <https://www.corning.com/worldwide/en/products/communication-networks/applications/microwave-connectivity.html>, Accessed: 2019-03-06.